Subsonic Analysis of 0.04-Scale F-16XL Models Using an Unstructured Euler Code

Wendy B. Lessard
Langley Research Center • Hampton, Virginia

October 1996

Summary

The subsonic flow field about the basic F-16XL airplane model, with and without air dams, was analyzed by investigators using an inviscid unstructured grid technique. Computed surface pressure distributions at 13 fuselage stations and 10 butt-line stations were compared with a wind-tunnel investigation at Mach 0.148 for a range of angles of attack from 0° to 20°. To evaluate the effect of grid dependency on the solution, a grid study was performed in which fine, medium, and coarse grid meshes were generated for the F-16XL without air dams. The off-surface grid field, which was locally adapted to the vortical flow field and compared to the nonadapted flow field, showed improved correlation with the wind-tunnel data. The computed off-body flow quantities for the no-air-dam configuration are compared to five-hole pressure probe data at $\alpha = 10°$. The grid for the basic F-16XL with air dams also was adapted to the vortical flow field, and solutions were obtained at $\alpha = 10°$, 13°, and 15°. A comprehensive analysis of the off-body computed pressure contours and velocity vectors is presented for configurations with and without the air dam.

Introduction

This paper describes a flight–wind-tunnel–computational fluid dynamics (CFD) validation experiment for the F-16XL airplane (ref. 1 and work in progress at Langley Research Center by S. J. Rickard). This paper focuses on the application and calibration of an unstructured grid method to solve the Euler equations for 0.04-scale models tested in the Basic Aerodynamic Research Tunnel (BART) facility (ref. 2) at Langley Research Center (fig. 1). The use of unstructured grids to compute flows about complex geometries has increased in recent years because the unstructured tetrahedral mesh discretizes irregularly shaped domains more easily than a structured grid does. Given the drastically reduced time to generate a grid, this approach is especially suitable for use in the design stages of configurations. Two disadvantages of using unstructured grids encountered by the investigator were increased computer memory requirements and increased postprocessing time. Solving the Euler equations requires less central processing unit (CPU) time than do the more accurate Navier-Stokes equations, and depending on the flow characteristics, the Euler equations can offer reasonable results fairly quickly.

One obvious shortcoming to using an Euler solver is the exclusion of viscous flow effects. While the Navier-Stokes equations are necessary to accurately capture all the flow physics, researchers have found that many of the important features of the primary vortex and its interaction with the wing can be modeled by the Euler equa-

tions. Euler equations work well for vortex-dominated flows generated by slender delta wings, where the viscous effects do not dominate the off-surface flow field and the flow separates from a sharp leading edge (ref. 3). The sensitivity of the Euler codes to such numerical parameters as artificial viscosity of the numerical algorithm and discretization errors also affects the solution (ref. 4). Therefore, the applicability of the Euler equations to this type of problem will depend on these types of considerations. Recent unstructured grid studies performed with the unstructured grid Euler code USM3D on a wing-pylon-store configuration (ref. 5) and an isolated fuselage geometry (ref. 6) reveal favorable comparisons of surface pressure distributions as well as forces and moments. Because favorable results were obtained from previous studies and the F-16XL has a slender cranked-arrow wing, USM3D was used to analyze this configuration.

Symbols and Abbreviations

BL	butt-line stations
CFD	computational fluid dynamics
CFL	Courant-Friedrichs-Lewy number
CPU	central processing unit
C_L	lift coefficient
C_P	static pressure coefficient
$C_{P,t}$	total pressure coefficient
FS	fuselage station
M	free-stream Mach number
MW	megaword
RN	Reynolds number
b	wing span, 15.58 in.
c	local chord
$\bar{c}$	mean aerodynamic chord, 11.87 in.
nd	without air dam
wd	with air dam
x/c	fraction of local chord
y	spanwise distance, in.
$y/(b/2)_1$	fraction of local semispan; note local semispan does not include missile rail and missile
z	normal distance, in.
α	angle of attack, deg

Model and Test

A three-view schematic of the 0.04-scale basic F-16XL configuration appears in figure 2. The basic model features an "S-shaped" leading edge at the wing

apex as opposed to a straight leading edge (modified apex), which was also experimentally tested but not included in this investigation. The model is 25.41 in. long with a 15.55-in. wingspan. The wing has an inboard leading-edge sweep angle of 70° and an outboard leading-edge sweep angle of 50°. Other model features include a vertical tail and a drag chute housing. An air dam on each wing extends part way onto the upper surface of the aileron-actuator pod. A missile consisting of four front and four rear fins attaches to each wingtip via a missile rail. The model is constructed with a flow-through inlet and nozzle.

Investigators obtained the experimental data in the BART facility (fig. 1) by testing a 0.04-scale F-16XL over a range of test conditions: 0° to 20°, $0.07 \leq M \leq 0.165$, and $500{,}000 \leq RN \leq 1\,120\,000$, all at zero sideslip. Data types taken included surface static pressure (ports mapped in fig. 3) and oil flow, five-hole pressure probe in the flow field (for total pressure and velocity magnitude and direction), vapor screen, and pressure-sensitive paint on several test configurations. Most of the data are reported in reference 1 and in the work in progress by S. J. Rickard at Langley.

Selected data samples for the basic model with missiles and with and without air dams are used in this paper for comparison purposes. Geometrical consistency of model and CFD numerical surface description are assumed in this data comparison.

Computational Grids and Method

The surface and volume grids were constructed with the grid generator VGRID (ref. 7), which is a tetrahedral unstructured grid generator based on the advancing front method (refs. 8 and 9). The parameters for the initial front (initial surface grid) were defined in GRIDTOOL (ref. 10). The GRIDTOOL program allows the user to interactively divide the configuration into bilinear patches, as well as define the node (or point) and line source locations (fig. 4), magnitudes, and directions. The nodal and line sources control the spacing on the surface and the cell sizes in the grid field. No grid stretching was used; a cell aspect ratio of 1.0 was specified, although not always maintained by the code. An initial front was created and projected onto the original database surface with GRIDTOOL. The front was then advanced into the field by adding tetrahedral cells to complete the grid.

Unstructured grids were generated for the basic F-16XL model with and without air dams. In an attempt to minimize the total number of cells, thereby reducing memory and run time required, fine, medium, and coarse grids of the F-16XL configuration without air dams were generated first. This method permitted not only assessment of the effects of grid dependency on the solution but also determination of the most efficient grid in terms of solution accuracy and computer resources.

Grid Study

An unstructured fine grid was generated first for the basic F-16XL without air dams. To ease the grid construction process, a small modification was made to the four fins located at the rear of the missile; the thickness of the leading and trailing edges of the fins was increased. Also, unlike the database, which modeled the tips of the four rear fins as collapsed lines, the computationally defined fins were modified to have a finite thickness. It would have been advantageous to model the fin tips with a singular line, which would result in fewer total grid cells being required because of the absence of the small tip surface. However, the collapsed fin-tip geometry produced difficulties for the advancing-front method.

The surface of the missile, missile rail, and surrounding area required a dense distribution of points to resolve the small fin geometry and to capture the flow physics in this region. A dense point distribution also had to be maintained in this area to ensure a good (not skewed) local meshing of the cells. Figure 5(a) shows the surface and reflection plane of the F-16XL unstructured fine grid. The grid outer boundaries were located about $5\bar{c}$ from the surface in all directions. The complete fine grid is composed of 1 144 077 cells and 205 317 points, with 19 000 points on the surface. Figure 5(b) shows a close-up view of the surface grid on the missile and missile rail. As the figure shows, small cell spacing over a fairly large field area was necessary to ensure local and global meshing with a minimum amount of skewness. A coarser grid density was generated by increasing all the source strengths by 1.25. A total of 899 083 cells and 161 967 points comprised this grid, with 16 351 grid points on the surface. Likewise, the coarse grid was generated by applying a 1.50 increase in the source strengths for the fine grid. The resulting coarse grid consisted of 532 622 cells and 96 835 points, with 11 740 points on the surface.

The fine, medium, and coarse surface grids are shown and compared to one another in figure 6. While a gradual decrease in point density is seen from fine to coarse grid, higher grid point density is consistently maintained for all three grids on the leading edge, in the missile area (including the wingtip), on the actuator pod, and at the wing/fuselage interface. The off-surface grid densities for each grid appear in figures 7 and 8 at fuselage stations FS10.0 and FS18.0, respectively. The different grid densities are not as apparent at FS18.0 as they are at FS10.0 because of the very small spacing initially required to resolve the fins on the fine grid. Even after increasing all point and line source strengths by a factor

of 1.5, the spacing on and around the missile region remained quite small.

The medium surface grid definition was chosen and then locally adapted to the vortical flow regions at $M = 0.148$ and $\alpha = 10°$. The justification for choosing the medium grid was based on solution accuracy and computational efficiency and is discussed in detail in the "Results" section. The "Results" section also demonstrates the need for local grid adaption in the regions of vortical flow. In order to find the location of the vortical flow areas, the pressure coefficient C_P contours from the converged solution were plotted in several crossflow planes so that the vortical cores (identified by the lowest C_P value) could be located. Line sources placed through these points produced a higher density of grid cells in the localized area of the vortex paths. These off-surface line sources also affected the point distribution on the surface of the adapted medium grid, as shown in figure 9. The completed adapted grid consisted of a total of 826 420 cells and 149 299 points, with 16 132 grid points on the surface. The researcher found that by maintaining approximately the same number of surface points as the medium grid (16 351 medium grid surface points), the volume grid could be generated more efficiently, clustering points only in the vortical regions. As will be shown, the adapted grid yielded significantly better surface pressure correlations with experiment, using fewer grid points. Cross-sectional planes at FS10.0 and FS18.0 for both the medium and adapted medium grid appear in figures 10 and 11, respectively. Note the clustering of cells above the wing, which represents the primary vortex regions [figs. 10(b) and 11(b)]. The investigator believed that the high density of points in the vicinity of the missile and wingtip generated by the fine spacing was not needed for solution accuracy, and specified a less clustered field grid around the missile for the adapted medium grid (fig. 11).

Once the investigator gained confidence in unstructured grid generation for this configuration, the air dam was added to the fine grid using GRIDTOOL. The original database of the air dam had a constant thickness; however, to facilitate gridding, the top of the air dam was modeled with zero thickness. Additional sources had to be placed on the air dam to resolve the geometry and the channel flow in this region. The initial front and volume were generated by increasing the source strengths by 1.25, the same source strength as that used for the medium grid. The volume grid was adapted for $\alpha = 10°$ by using the same source specifications used for the no-air-dam configuration at $\alpha = 10°$ because the flow field was not expected to change much. The resulting grid contained 1 052 737 cells and 189 283 points, with 18 392 grid points on the surface. Figure 12 shows the surface grid of this configuration, as well as a close-up view of the air-dam geometry and point distributions. As the "Results" section shows, the grid adapted for the $\alpha = 10°$ solution proved to be sufficient for the $\alpha = 13°$ solution, so a new grid did not have to be generated. However, a new adapted grid had to be constructed for the $\alpha = 15°$ case because the vortical core path had moved far enough outside the densely clustered area used for the $\alpha = 10°$ through $13°$ range. A newly generated grid reflected the new locations of the vortical core path. The researcher determined this new path by locating the vortical core in several crossflow planes obtained from a partially converged solution (to minimize use of computer resources) at $\alpha = 15°$ using the grid adapted for the lower angle-of-attack solutions.

Computational Method

The flow field was computed using USM3D (ref. 11), which solves the time-dependent three-dimensional Euler equations in a computational domain discretized by tetrahedral-mesh elements. Spatial discretization was accomplished by using the flux-splitting method of Roe, which is based on a cell-centered finite-volume approach. The solution was advanced in time through use of an implicit Gauss-Seidel scheme, and convergence was accelerated to steady state by local time stepping and implicit residual smoothing. Flow tangency was imposed on solid boundary surfaces, and density and pressure boundary conditions were set to the cell-centered value. Characteristic boundary conditions were applied to the far-field subsonic boundary in which the fixed or extrapolated Riemann invariants were used, depending on the wave direction. Further details about the computational method are discussed in reference 11.

Results

The solution results for each grid are presented and discussed in the same order as outlined in the "Computational Grids and Method" section, namely grid study on F-16XL model (no air dam), adapted grid for $\alpha = 10°$, and adapted grid with air dams for $\alpha = 10°$, $13°$, and $15°$. All solutions obtained were at $M = 0.148$.

Convergence and Performance Characteristics

The computations performed in this study (including the grid generation) were done on the Cray-C90 located at the Ames Numerical Aerodynamic Simulation (NAS) center and the Cray-YMP computer located at Langley Research Center. Figure 13 shows the convergence histories for the coarse, medium, and fine grids obtained at $\alpha = 10°$ and $M = 0.148$. The fine grid required a 206-MW memory allotment and took 1650 iterations to reduce the residuals by 2.5 orders of magnitude. At 31.0 µs per cycle per cell, the solutions took about 16 hr

to converge on the Cray-C90. The fine grid exhibited slow residual and C_L convergence characteristics partly because of the inability to increase the Courant-Friedrichs-Lewy (CFL) number beyond 10. The medium grid required 162 MW of memory and took 700 iterations to reduce the residuals by almost 2.5 orders of magnitude. The medium solution was obtained after approximately 4.3 hr of Cray NAS time and took 24.0 μs per cycle per cell. A rapid convergence was evident for the medium grid, and the CFL number was quickly ramped up to 30. The coarse grid solution was obtained by using the Cray-YMP because of the reduced memory size of 96 MW. The time per cycle on this machine was 50.0 μs per cycle per cell, and the solution converged after 700 iterations, which took about 5.4 hr. As with the medium grid, rapid convergence was achieved for the coarse grid, and the CFL number was ramped up to 30.0. Figure 13(b) shows similar C_L convergence histories for the medium and coarse grids.

Figure 14 shows the convergence history for the adapted medium grid at $\alpha = 10°$ (the configuration without the air dams). The solution converged fairly quickly (and was ramped up to a CFL number of 30.0) after about 900 iterations, which took 5.2 hr on the Cray-C90. The convergence histories for the F-16XL with air dams for $\alpha = 10°$ and 15° are shown in figures 15 and 16, respectively. Compared to the adapted medium grid, the configuration with the air dams at $\alpha = 10°$ required more than double the number of iterations to converge. The poorest convergence characteristics were seen for $\alpha = 15°$, which is shown in figure 16. After 3200 iterations, the C_L was still oscillating, and a decrease of only one order of magnitude in the residuals was noted. The total run time on the Cray-C90 was 24 hr. The large amount of CPU time required (51.7 hr if run on the Cray-YMP) to obtain an "almost converged" solution was impractical. Also the solution may have developed some unsteady flow-field characteristics at that point.

Pressure and Flow-Field Analysis

Without air dams. The fine, medium, and coarse grid surface pressures for the F-16XL configuration without the air dams at $M = 0.148$ and $\alpha = 10°$ are compared with experimental data in figure 17 at 13 different fuselage stations. As stated, this comparison was done to determine the sensitivity of the Euler solutions (using USM3D) to surface grid refinement. However, the small benefits gained in solution accuracy do not justify the added memory and run time required with a finer surface grid.

While the computed pressure coefficients for all the grids, shown in figure 17, follow the general trend of the experimental data, all three grids underpredicted those

surface C_P distributions influenced by vortical flow (see FS7.4–FS15.0). Computed C_P values for all the grids compared better to experiment at FS16.3–FS19.7; however, because there were no pressure ports at these stations in the higher peak regions (except at FS19.7), the researcher could not determine whether the computations also predict suction peaks similar to the measured values. Compared to the medium and coarse grids, the fine grid solution generally yielded greater negative pressures on both upper and lower surfaces for all fuselage stations. The medium and coarse grids yielded almost identical pressures on the lower surface, while the fine grid pressures appeared to be offset by a negative constant. It is difficult to determine which grid correlated better with experiment on the lower surface because measured pressure data were limited; however, the relatively large decrease (compared to the coarse and medium grid) in computed lower surface C_P of the fine grid appears suspect. Although pressure correlations improved slightly for the fine grid for the first eight fuselage stations, the medium and coarse grids correlated better with experiment for FS17.0–FS18.0. From this comparative analysis, it is evident that the small improvement gained from using the fine grid does not warrant the additional computer run time and memory associated with it. The medium grid was, therefore, chosen as the best surface grid because it captured the overall principal flow characteristics in minimal run time.

The surface C_P distributions for the adapted medium grid are plotted with the medium grid results in figure 18. The localized clustering of grid points in the regions of vortical flow resulted in better resolution of the off-surface flow field, which in turn yielded more accurate surface pressure distributions. The computed C_P values obtained with the adapted grid correlated quite well with the experimental data, and the differences between the solutions for the adapted and nonadapted grids were substantial. Both grids yielded the same lower surface pressure distributions because the point distributions were the same on the lower part of the wing. The computed suction peak at FS10.3 appears to have been overpredicted, and a slightly lower computed suction peak is seen at FS13.5 and FS15.0. At the last fuselage station, the adapted medium grid solution showed an additional low-pressure region (peak at $y/(b/2)_l = 0.72$).

Off-body C_P contours for the medium and adapted medium grid at FS10.0, FS18.0, and FS19.7 appear in figures 19, 20, and 21, respectively. Compared to the medium grid, the adapted grid solution yielded a more developed vortical flow system with larger negative pressure values in the vortex core for all fuselage stations. The low-pressure region at $y/(b/2)_l = 0.72$ predicted by the adapted grid previously mentioned can be further explained by examining figure 21. The adapted vortex

core (fig. 21(b)), which had moved outboard of the actuator pod, affected the wing surface below it, causing the low suction peak seen in figure 18 at FS19.7. Because the primary vortex core was positioned directly over the actuator pod for the medium grid, only one negative suction peak resulted, and that formed over the actuator pod or at $y/(b/2)_1 = 0.63$ at FS19.7 (fig. 18). Figure 22 shows a close-up view of the velocity vectors in this region. The effect of the computed adapted vortex on the wing is evident in figure 22(b), which shows increased circulation near the surface.

The computed C_P and $C_{P,t}$ contours and crossflow velocity vectors obtained from the adapted grid are compared to the experimental five-hole pressure probe data in figures 23–31. All contour values are displayed with a gray scale to provide a clear depiction of the vortex size and shape, as well as its varying magnitude. Corresponding minimum and maximum limits at each fuselage station were used to scale the C_P and $C_{P,t}$ contours. The computed and measured velocity vector magnitudes were multiplied by their appropriate nondimensional values for comparison purposes. Because of the size of the pressure probe, flow-field data could not be obtained very close to the surface. The computed C_P contours are compared to experiment at FS9.0 in figure 23. The computed vortex-core C_P value was -2.05 in the vortex core, located at $y = 2.79$ in. and $z = 3.87$ in., and was slightly inboard and closer to the wing surface than the measured vortex core, which had a value of -1.25 and was located at $y = 2.82$ in. and $z = 3.92$ in. These results appear to substantiate the surface pressure distributions plotted in figure 18 for FS8.6 and FS10.3, which show that the computations indeed overpredicted the experiment.

The $C_{P,t}$ contours shown in figure 24 are more representative of the oval shape of the vortex depicted by the velocity vectors in figure 25. A greater total pressure loss is seen for the computed vortex, which had a core value of -1.28 compared to a -0.60 measured value. These numerically induced computed total pressure losses were largest in areas of high gradients and in regions with concentrated vorticity (ref. 4). The crossflow velocity vector plots compared in figure 25 show similar magnitude and direction. The computed and measured C_P contours at FS14.0 appear in figure 26. The computed C_P for the vortex core located at $y = 3.98$ in. and $z = 4.11$ in. had a magnitude of -1.27, and the experimental vortex core positioned at $y = 4.11$ in. and $z = 4.16$ in. reported a magnitude of -1.31. This trend is consistent with the C_P plots in figure 18 at FS13.5 and FS15.0, which show the measured C_P vortex core value to be slightly higher than the computed value. The vortical structures look very similar, except at the surface where the absence of the bound-

ary layer in the inviscid CFD solution did not affect the vortex shape, as seen in the experiment. The computed and measured vortical shapes and structures appear more alike in figure 27, which plots the $C_{P,t}$ contours. The computed $C_{P,t}$ value in the vortex center was approximately double the measured value, which was also true at FS9.0. The velocity vector plots shown in figure 28 reveal a similar pattern and trend. Both the computed and measured C_P values in the vortical core for station FS18.0 (fig. 29) were approximately -0.88. As occurred for the two previous fuselage stations, the predicted vortex core located at $y = 5.05$ in. and $z = 4.22$ in. was slightly inboard and closer to the wing surface than was the experimental vortex core ($y = 5.25$ in., $z = 4.39$ in.). The predicted and measured $C_{P,t}$ contour plots (fig. 30) showed similar vortex structure, and the computed pressure loss was double that measured in the vortex core. Figure 32 shows corresponding crossflow velocity vectors.

With air dams. This section presents and discusses the pressure distribution plots and crossflow pressure contours and velocity vectors for the F-16XL configuration with air dams at $\alpha = 10°$, $13°$, and $15°$. As before, all grids were adapted to the vortical flow field. The computations were compared to experiment at 10 butt-line stations and 13 fuselage stations.

The computational pressure distributions for $\alpha = 10°$ are compared with experiment in figures 32 and 33. Very good correlation is seen at all the butt-line stations plotted in figure 32. The extracted computational pressures at BL2.2 and BL2.5 are rather nonsmooth because of the sparse number of grid points used to define the inboard wing area near the fuselage. The largest discrepancy between the data sets appears forward on the wing at station BL3.8, where the computations failed to predict the suction peak at $x/c = 0.04$. This low-pressure region may have been caused by a secondary vortex that the Euler method could not capture or by leading-edge suction that the solution did not pick up because the grid was not fine enough in that area. The computational pressure results also correlated well with experiment at all the fuselage stations (fig. 33). The calculated suction peak at FS7.4 was underpredicted and most likely the result of an insufficient number of grid points being generated in this area. Compared to the configuration without the air dams in which only one vortex was generated from the leading edge, the more complicated flow with the air dam exhibited multiple vortices. The influence of the air dam on the flow was first seen at FS15.0, where a sharp transition from high to low pressure occurred at about the 0.93 local spanwise location. A more detailed account of the differences between the configurations with and without the air dam follows.

The calculated particle traces for the F-16XL with air dams (shown in fig. 34) trace the path of each vortex, and are labeled for easy reference. The vortices depicted in the C_P contours and velocity vector plots shown in figures 35–37 are labeled likewise. Figure 35 shows the vortex generated from the apex of the leading edge in a crossflow plane at FS10.0. This vortex, labeled A, propagated along the inboard portion of the wing. A smaller, clockwise-rotating vortex, B, emanated from the sharp leading edge of the air dam and traced an outboard path (fig. 36). Another vortex, C, which rotated in the counterclockwise direction and appeared outboard of vortex B, formed as a result of a saddle-point or off-surface separation in the flow. The effect of this vortical system on the surface is evident in the pressure distribution plot at FS16.3 (fig. 33). Vortex A had a suction peak at $y/(b/2)_l = 0.72$, and vortices B and C had C_P values of approximately -0.60 and -0.70 at $y/(b/2)_l = 0.84$ and 0.89, respectively. As the vortical system propagated downstream, it continued to expand, and a newly formed vortex D appeared at FS20.2 (fig. 37). This vortex must have been very weak because there is no intertwining of the particle traces in figure 34. Figure 38 shows a close-up view of the velocity vectors in the missile area at FS20.2. One sees a vortex on three of the missile fins and one in the middle of the upper two fins.

The computed versus experimental surface pressure coefficient comparisons at $\alpha = 13°$ appear in figures 39 and 40. The computational pressures match well at this angle of attack, and the grid, which was adapted for the $\alpha = 10°$ solution, appears sufficiently clustered to accurately resolve the flow at $\alpha = 13°$. Figures 41–43 show the computed pressure contours and velocity vectors in three crossflow planes. The overall flow features and vortical footprints were similar to the $\alpha = 10°$ solution; therefore, the off-surface particle traces are not presented. Examination of the labeled vortices depicted in figures 41–43 reveals the same vortical system identified for $\alpha = 10°$. At FS10.0, one sees a single vortex, A, on the wing that is similar (although greater in magnitude) to the one that developed for the $\alpha = 10°$ solution. Likewise, at FS16.3, shown in figure 42, multiple vortices developed as a result of the flow impinging on the air dam, and vortex A appears to have split in two. However, the off-surface particle traces revealed only a single vortex in that region, and as shown in figure 43, vortex A did indeed remain intact. In contrast to the $\alpha = 10°$ solution, vortex C appears to be merging with the others in the flow field, and vortex D is more developed. The velocity vectors plotted around the missile in a crossflow plane are shown in figure 44. A small vortex, which did not exist for the $\alpha = 10°$ solution, formed on the lower left fin.

The computed pressure distributions at all fuselage and butt-line stations correlated well with experiment for $\alpha = 15°$, as shown in figures 45 and 46. Compared with the $\alpha = 10°$ and $\alpha = 13°$ solutions, which showed a smooth distribution of pressures on the upper surface at the last three butt-line stations, the $\alpha = 15°$ solution yielded a more uneven distribution of pressures (BL5.9–BL6.9 in fig. 45). This uneven pressure distribution may have been caused by the increase in spanwise flow on the outboard portion of the wing. In general, computational and experimental pressure distribution trends remained similar for all three angle-of-attack solutions. The computed off-surface particle traces are shown in figure 47, and the computed pressure contours and velocity vectors are presented in three crossflow planes in figures 48–51. Unlike the previous two solutions in which vortex B remained intact near the trailing edge, vortex B merged with vortex A at FS20.3 (fig. 50). Also vortex C occurred more outboard on the wing as a result of the increased spanwise flow. In figure 50, the increased circulation of the vortex A,B and vortex C appears to prevent the formation of the smaller vortices evident in the lower angle-of-attack solutions. Flow in the vicinity of the wingtip missile fins shown in figure 51 closely resembled that of the $\alpha = 13°$ solution (fig. 39) only more well-defined.

Figure 52 shows the effect of adding the air dam on the overall surface C_P of the F-16XL for $\alpha = 10°$. The C_P pattern remained basically the same for both configurations up to about FS13.5, and similar computational and experimental C_P data were noted at this station (fig. 53). In contrast to the surface flow without the air dam, the vortical flow of the air-dam configuration split and was directed to each side of the air dam, as shown in figure 52(b). The flow that traveled outboard accelerated spanwise toward the wingtip, which resulted in greater negative C_P values on the outboard wing compared to those of the no-air-dam configuration. Higher suction peak values were noted for both experiment and computations (outboard of the air dam) for FS16.3–FS19.7, shown in figure 53. The experimental peak pressure values at FS13.5 and FS15.0 were slightly higher for the model without the air dam (fig. 53) although the computations show the opposite. This discrepancy probably was caused by the grid. Because more points were required to resolve the air dam, the higher grid density in this area may have resolved the flow better.

Concluding Remarks

The subsonic ($M = 0.148$) flow field about the basic F-16XL cruise configuration, with and without air dams, was modeled with an inviscid unstructured grid technique, namely VGRID and USM3D. In order to assess the grid dependency of the solution, a grid study

was performed in which coarse, medium, and fine grids were generated for the model without air dams. No significant improvements in solution accuracy were seen (through comparison of computations to experiment) when the number of grid points was globally increased. In fact, all the USM3D solutions that used these grids exhibited poor correlation with experiment when compared to the adapted grid. The finest grid, which had over 1 000 000 points, exhibited very slow convergence characteristics and took about 16.0 hr on the Cray-C90 to converge. The grid distribution of the medium grid was chosen as the most efficient surface representation in terms of memory, run time, and convergence qualities. The researcher used the medium grid as a starting point, and the off-surface grid of the basic configuration with air dams was locally adapted to the vortical flow at $\alpha = 10°$, $13°$, and $15°$. Increases in the grid-point density in the vortical regions resulted in a more resolved flow and a marked improvement in the comparison between computational and experimental pressure distributions when compared to the nonadapted grid. An integrated package that couples the adaptive grid process with the grid generator and flow solver would be an invaluable tool for the designer and researcher. Not only would the grid generation time and effort be reduced but also any guess work on the part of the investigator in terms of locating the vortex core for adaption purposes would be eliminated.

The computed off-surface static and total pressure coefficient contours and velocity vectors compared well with the BART five-hole probe flow-field data (F-16XL without air dams) and provided a more comprehensive description of the flow physics when used in conjunction with the surface pressure distributions. For all crossflow planes examined, the computed vortex-core static-pressure-coefficient value was located slightly inboard and closer to the wing surface than was the measured value. In contrast to the F-16XL model without air dams, in which only one vortex was generated from the leading edge, the flow with the air dams was more complicated in that multiple vortices were produced. Comparison of computed results with experimental data shows that most of the primary features of the flow were correctly simulated. Differences between the predicted and measured

results were attributed mainly to viscous effects, such as secondary separation.

NASA Langley Research Center
Hampton, VA 23681-0001
August 26, 1996

References

1. Rickard, Susan J.; Washburn, Anthony E.; Morris, Martin J.; and Donovan, John F.: *Pressure Sensitive Paint Studies of Vortical Flow at Low Speed*. SAE Paper 951989, Sept. 1995.

2. Sellers, William L., III; and Kjelgaard, Scott O.: The Basic Aerodynamics Research Tunnel—A Facility Dedicated to Code Validation. AIAA-88-1997, May 1988.

3. Newsome, Richard W.; and Kandil, Osama A.: Vortical Flow Aerodynamics—Physical Aspects and Numerical Simulation. AIAA-87-0205, Jan. 1987.

4. Hoeijmakers, H. W. M.; and Van Den Berg, J. I.: Application of an Euler-Equation Method to a Sharp-Edged Delta-Wing Configuration With Vortex Flow. AIAA-91-3310, Sept. 1991.

5. Parikh, Paresh; Pirzadeh, Shahyar; and Frink, Neal T.: Unstructured Grid Solutions to a Wing/Pylon/Store Configuration Using VGRID3D/USM3D. AIAA-92-4572, Aug. 1992.

6. Ghaffari, Farhad: On the Vortical-Flow-Prediction Capability of an Unstructured-Grid Euler Solver. AIAA-94-0163, Jan. 1994.

7. Pirzadeh, Shahyar: Recent Progress in Unstructured Grid Generation. AIAA-92-0445, Jan. 1992.

8. Peraire, J.; Morgan, K.; and Peiro, J.: Unstructured Mesh Methods for CFD. *Numerical Grid Generation*, Imperial College of Science and Technology, London (England), 1990, pp. 37–66.

9. Löhner, Rainald; and Parikh, Paresh: Generation of Three-Dimensional Unstructured Grids by the Advancing-Front Method. *Int. J. Numer. Methods Fluids,* vol. 8, 1988, pp. 1135–1149.

10. Samareh-Abolhassani, Jamshid: Unstructured Grids on NURBS Surfaces—NonUniform Rational B-Splines. AIAA-93-3454, Aug. 1993.

11. Frink, Neal T.: Upwind Scheme for Solving the Euler Equations on Unstructured Tetrahedral Meshes. *AIAA J.*, vol. 30, Jan. 1992, pp. 70–77.

Figure 1. F-16XL model with air dams in BART tunnel.
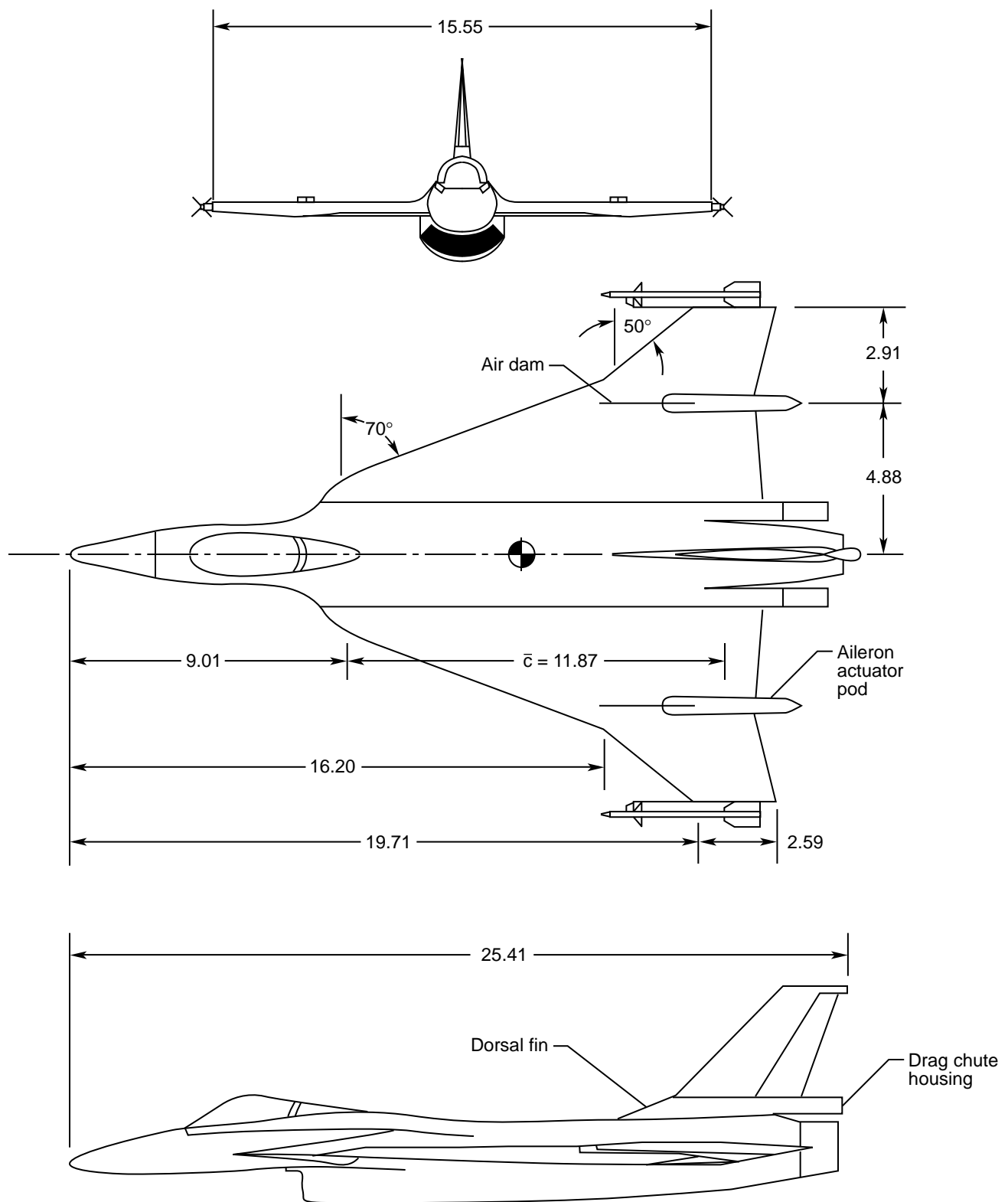
Figure 2. Three-view sketch of 0.04-scale F-16XL model. Dimensions are given in inches.

9

FS = fuselage station
BL = butt-line station

FS 5.6
FS 6.4
FS 7.4
FS 8.1
FS 8.6
FS 9.2
FS 10.3
FS 11.3
FS 12.0
FS 13.5
FS 15.0
FS 15.6
FS 16.3
FS 17.0
FS 17.5
FS 18.0
FS 18.5
FS 19.7

BL 1.2
BL 1.5
BL 1.7
BL 2.0
BL 2.2
BL 2.5
BL 2.8
BL 3.2
BL 3.5
BL 3.8
BL 4.2
BL 4.8
BL 5.1
BL 5.5
BL 5.9
BL 6.4
BL 6.9
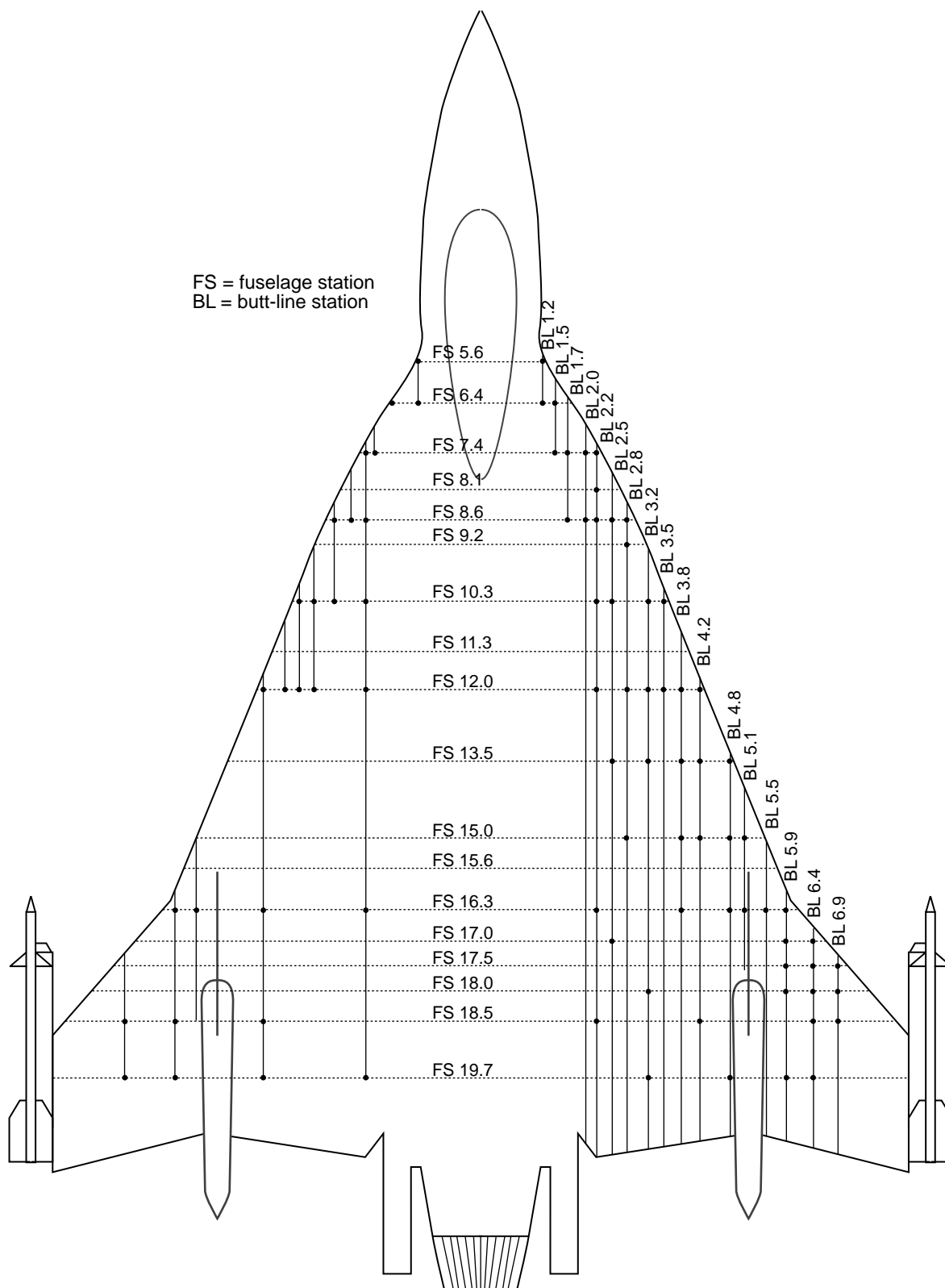
Figure 3. Pressure port locations on 0.04-scale F-16XL model. Dimensions are given in inches.
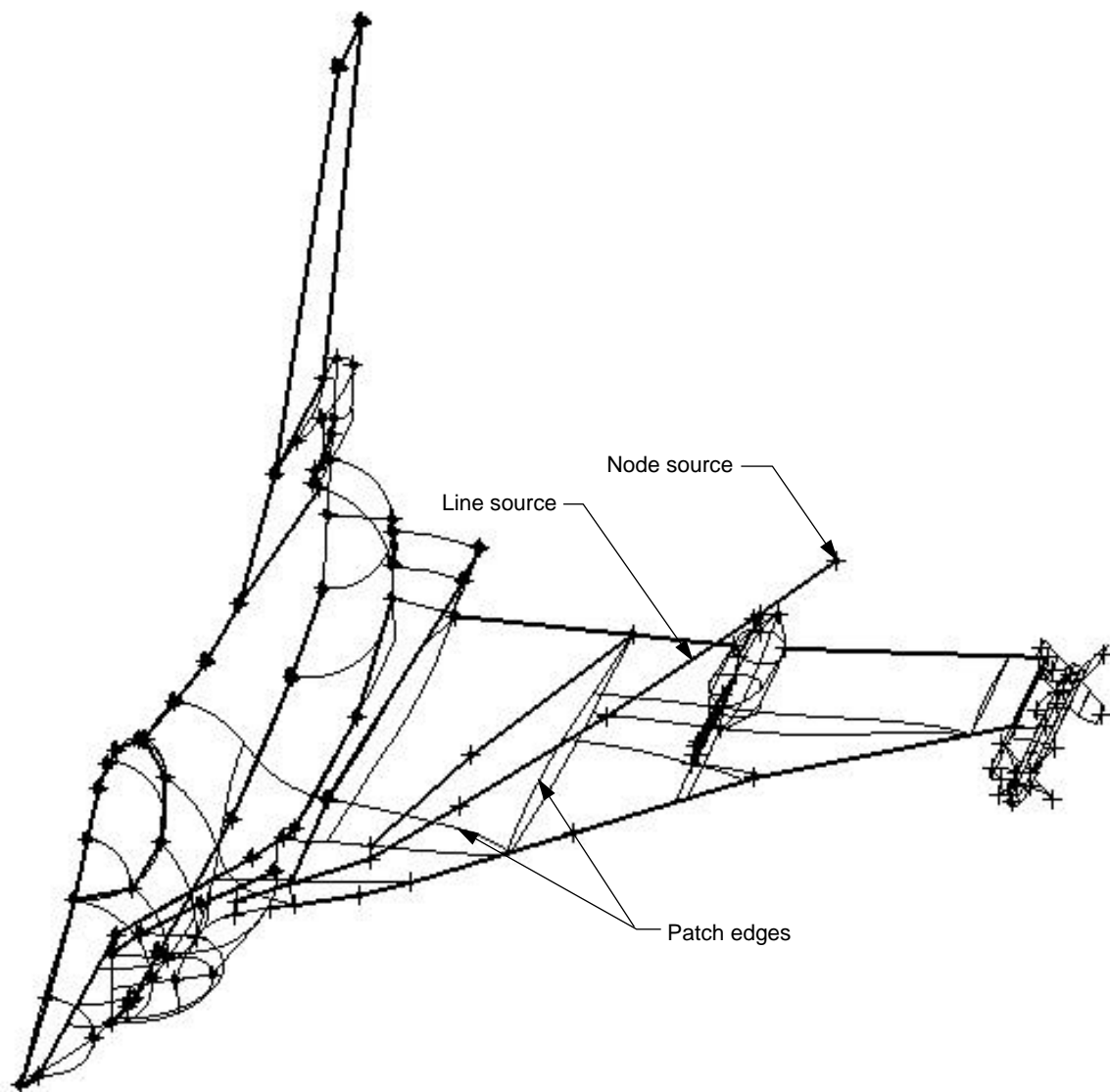
Figure 4. Patched surface depicting node and line source locations for F-16XL with air dams, $\alpha = 15°$.
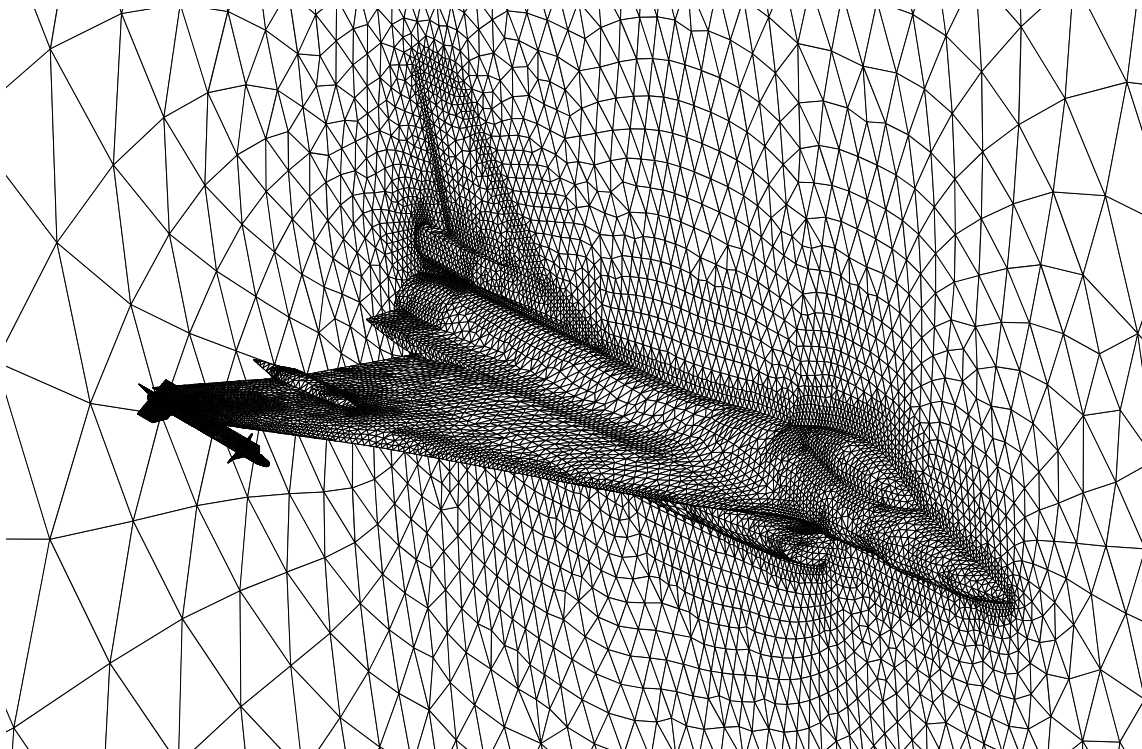
(a) Surface and symmetry plane.
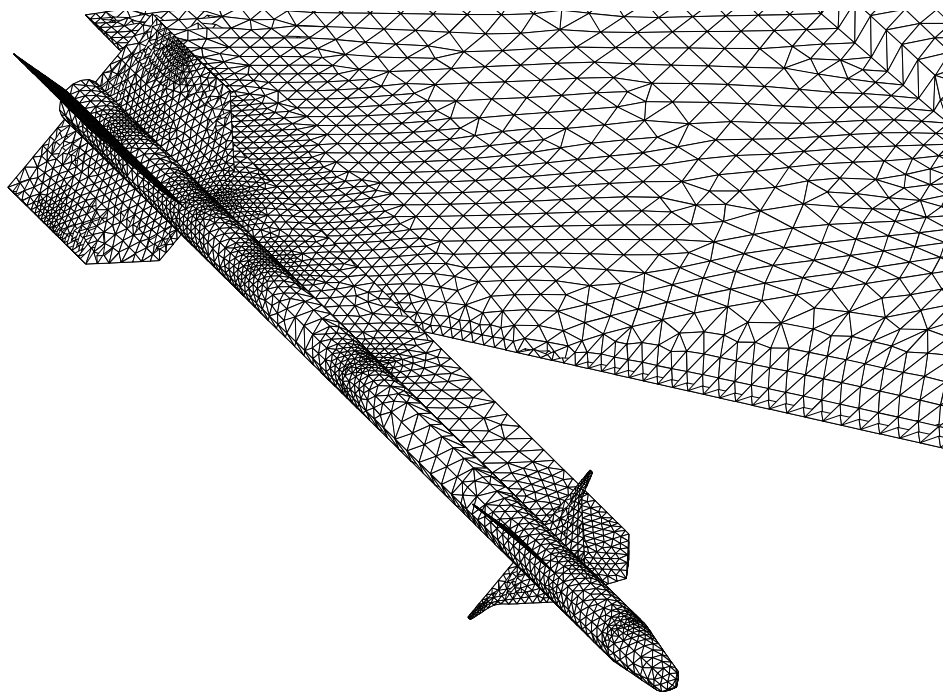
(b) Close-up view of missile surface.

Figure 5. Unstructured fine grid for F-16XL without air dams.
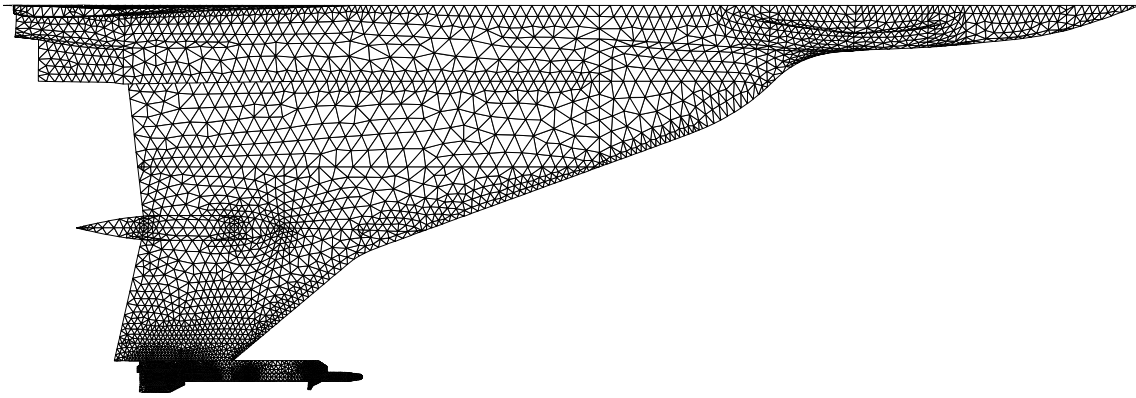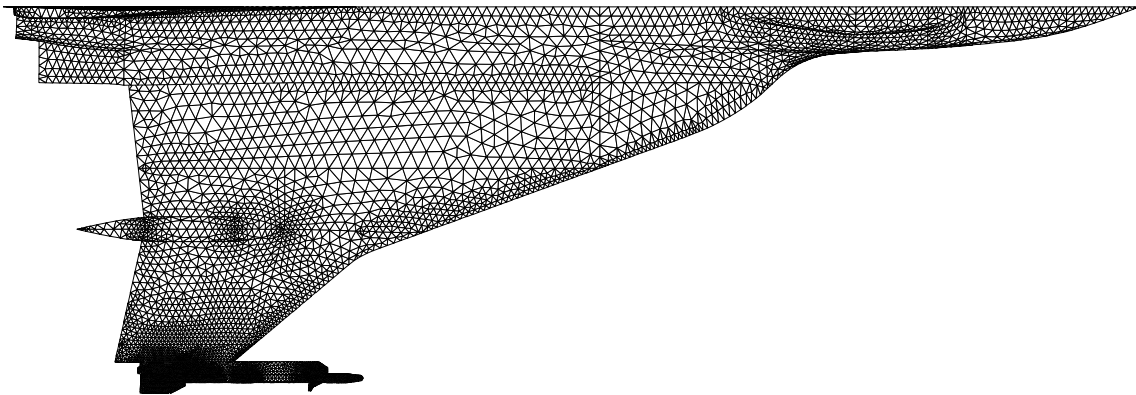
(a) Coarse grid.
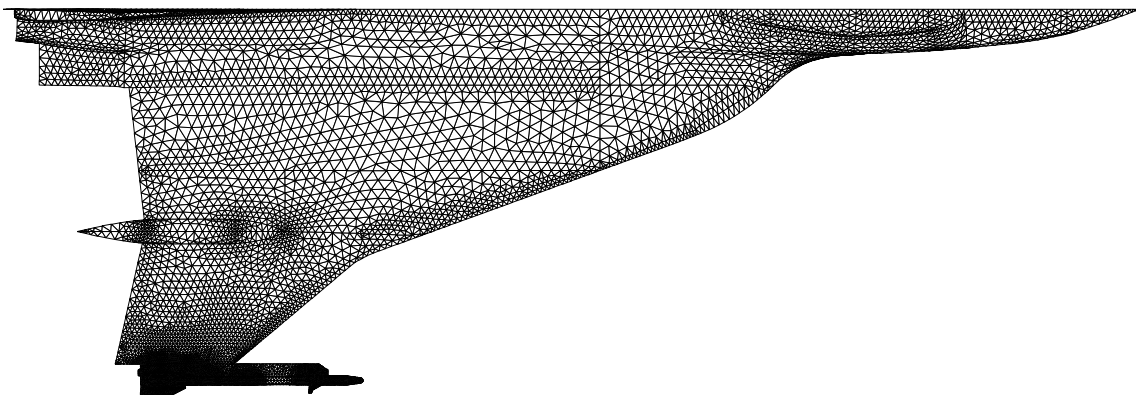
(b) Medium grid.

(c) Fine grid.

Figure 6. Surface grids of varying densities for F-16XL without air dams.
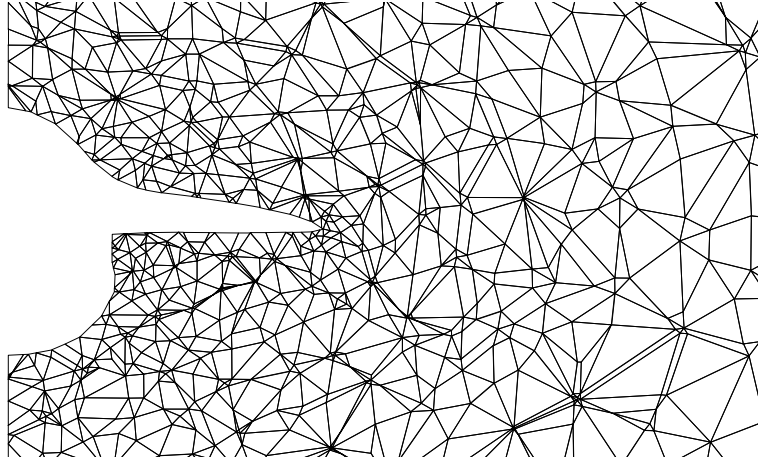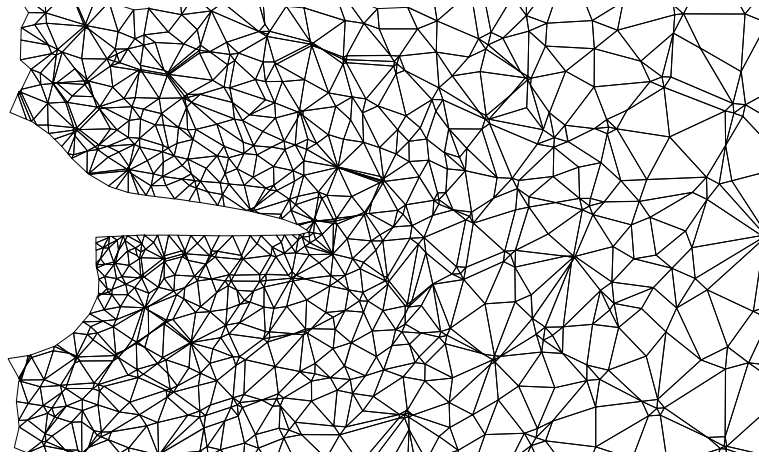
(a) Coarse grid.
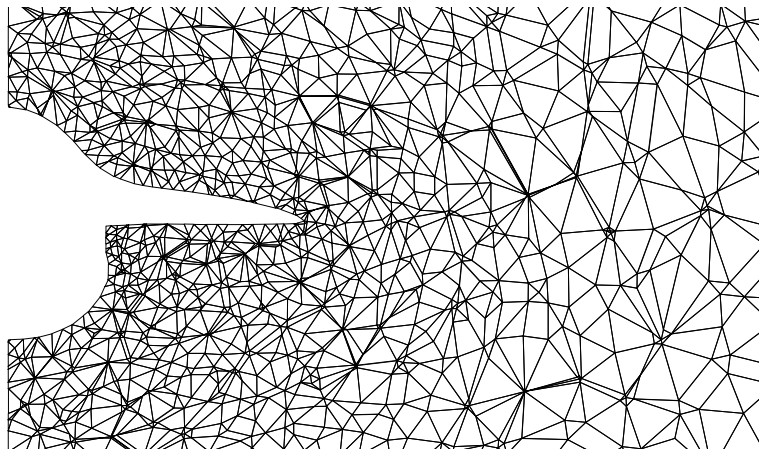
(b) Medium grid.

(c) Fine grid.

Figure 7. Cross-sectional grid planes at FS10.0 for F-16XL without air dams.
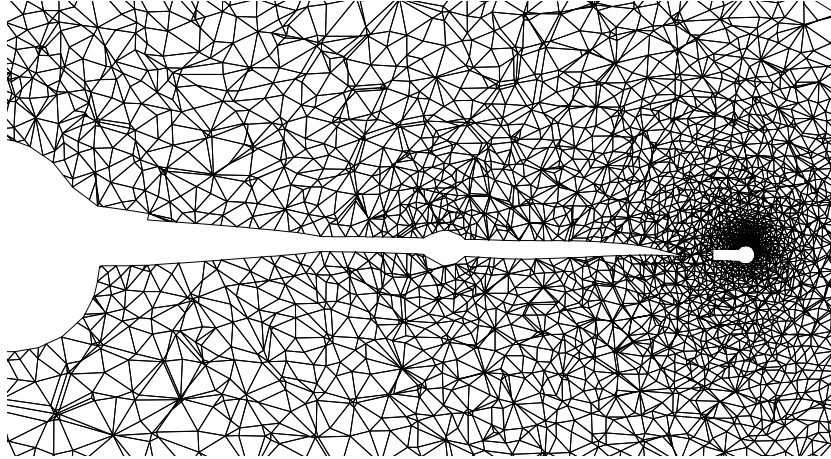
(a) Coarse grid.
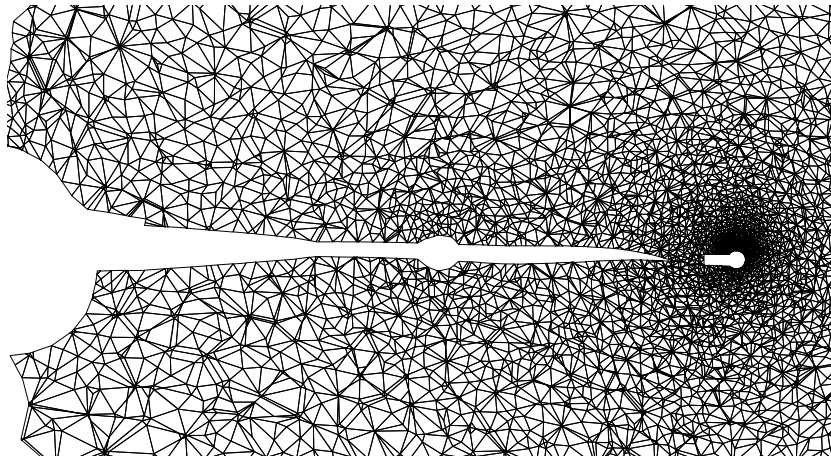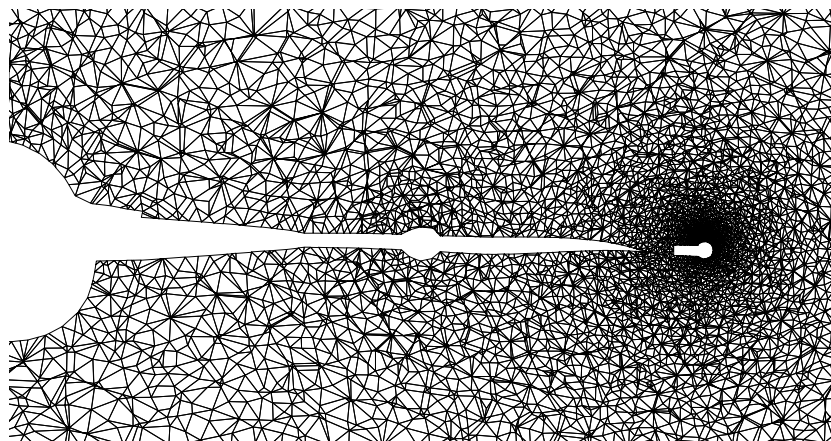
(b) Medium grid.

(c) Fine grid.

Figure 8. Cross-sectional grid planes at FS18.0 for F-16XL without air dams.
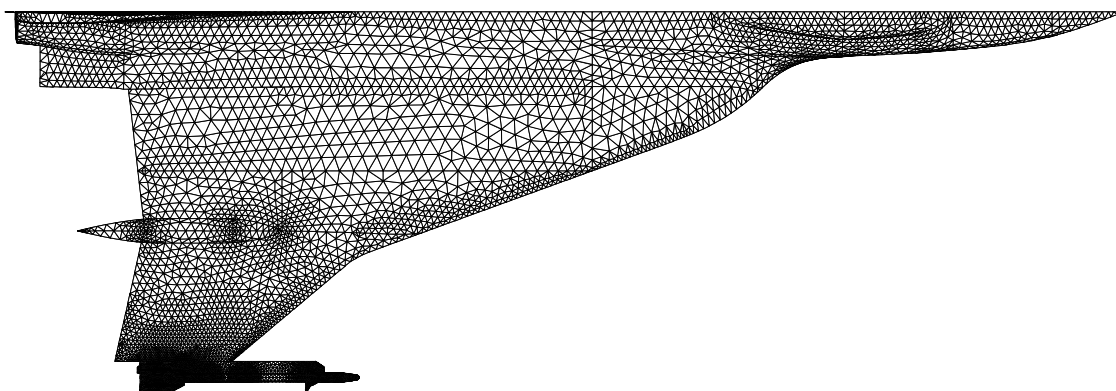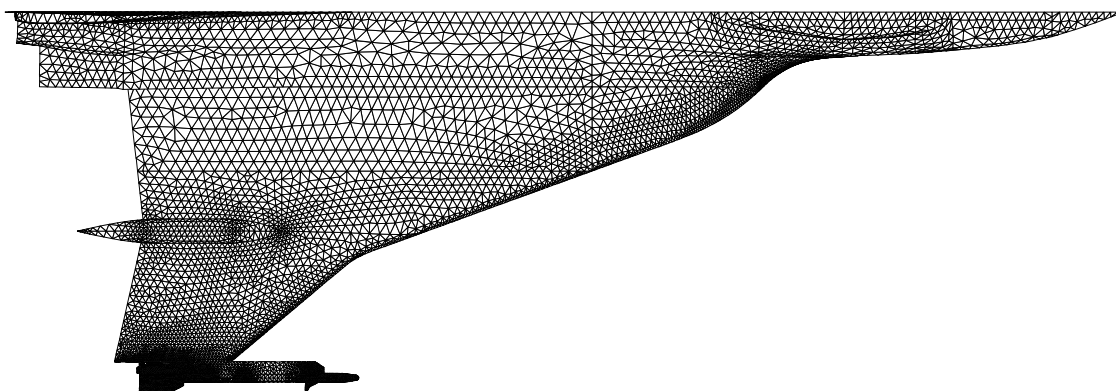
(a) Medium grid.

(b) Adapted medium grid.

Figure 9. Adapted and nonadapted surface grids for F-16XL without air dams.
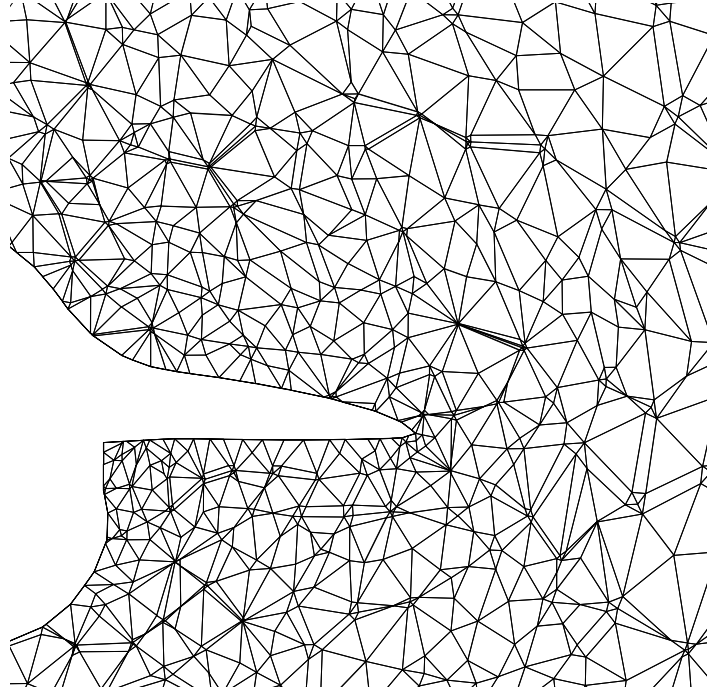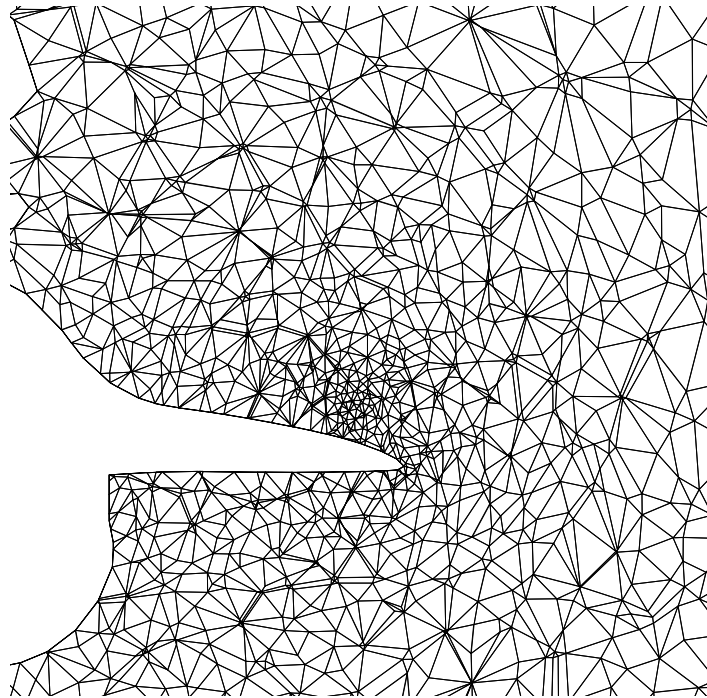
(a) Medium grid.

(b) Adapted medium grid.

Figure 10. Cross-sectional planes of adapted and nonadapted grids at FS10.0 for F-16XL without air dams, $\alpha = 10°$.
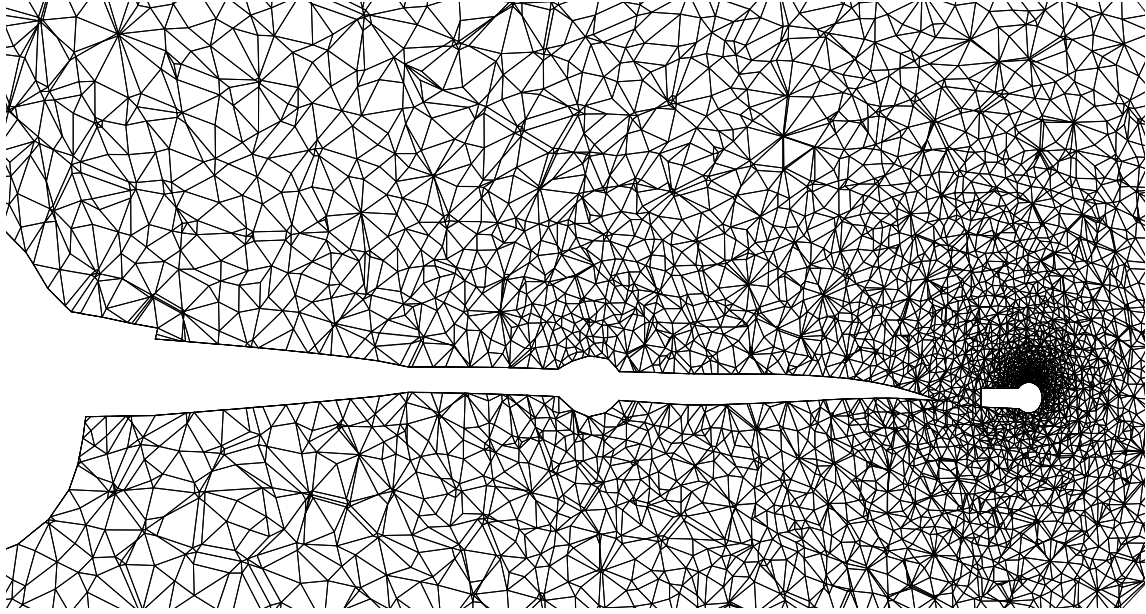
(a) Medium grid.
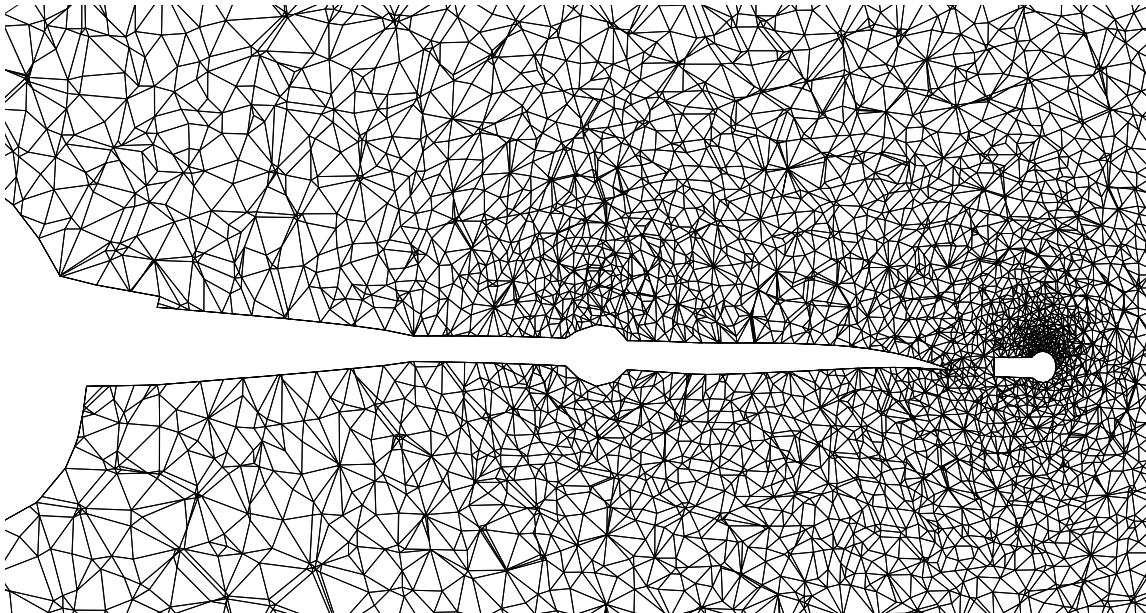
(b) Adapted medium grid.

Figure 11. Cross-sectional planes of adapted and nonadapted grids at FS18.0 for F-16XL without air dams, $\alpha = 10°$.
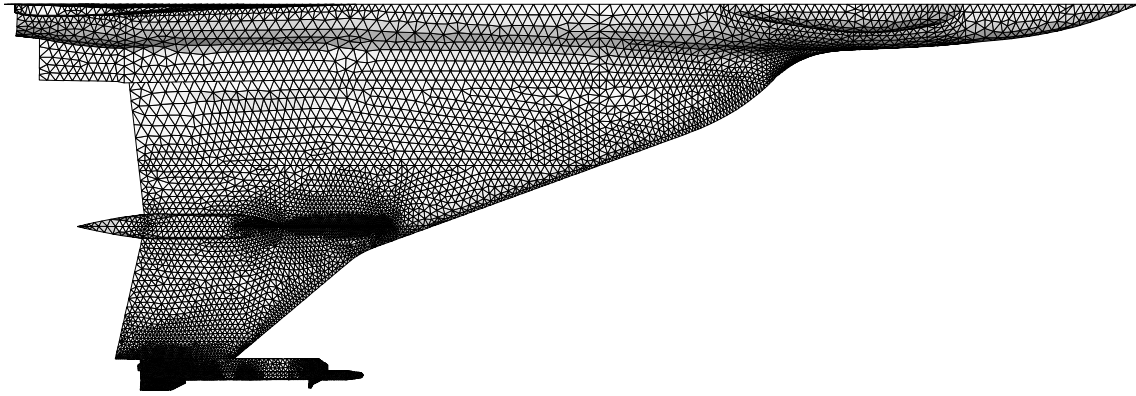
(a) Planform view of upper surface mesh.
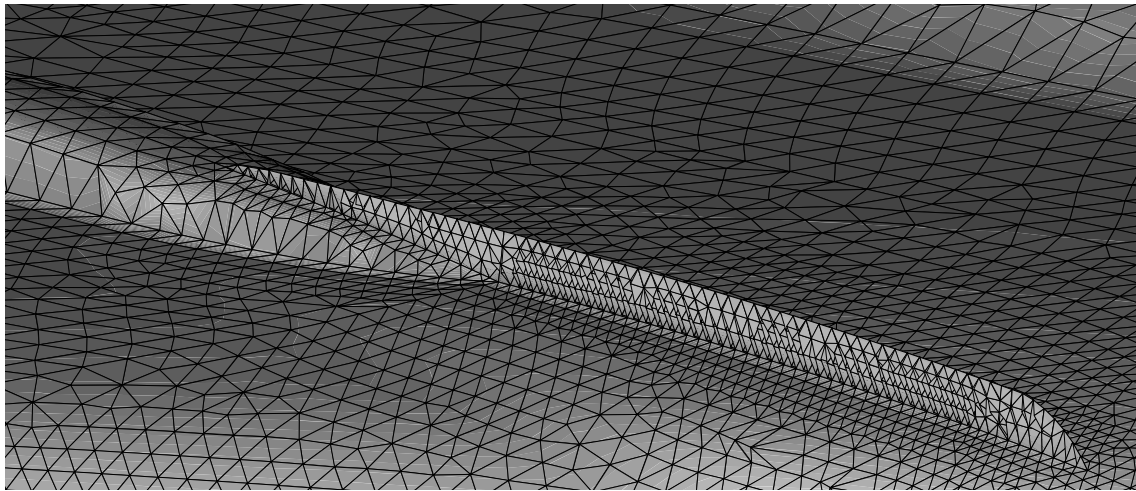
(b) Close-up view of air-dam geometry.

Figure 12. Adapted surface mesh for F-16XL with air-dams, $\alpha = 10°$.

(a) Residual convergence.
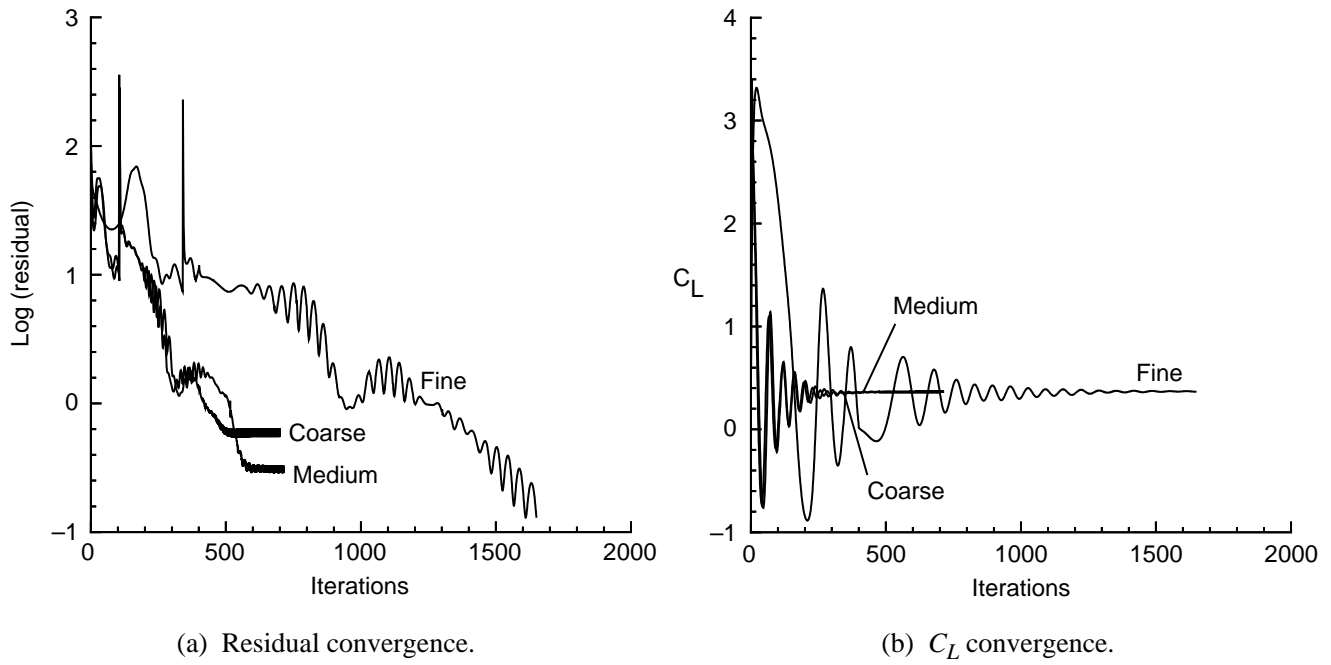
(b) C_L convergence.

Figure 13. Grid study convergence characteristics for F-16XL without air dams, $\alpha = 10°$, $M = 0.148$.

(a) Residual convergence.
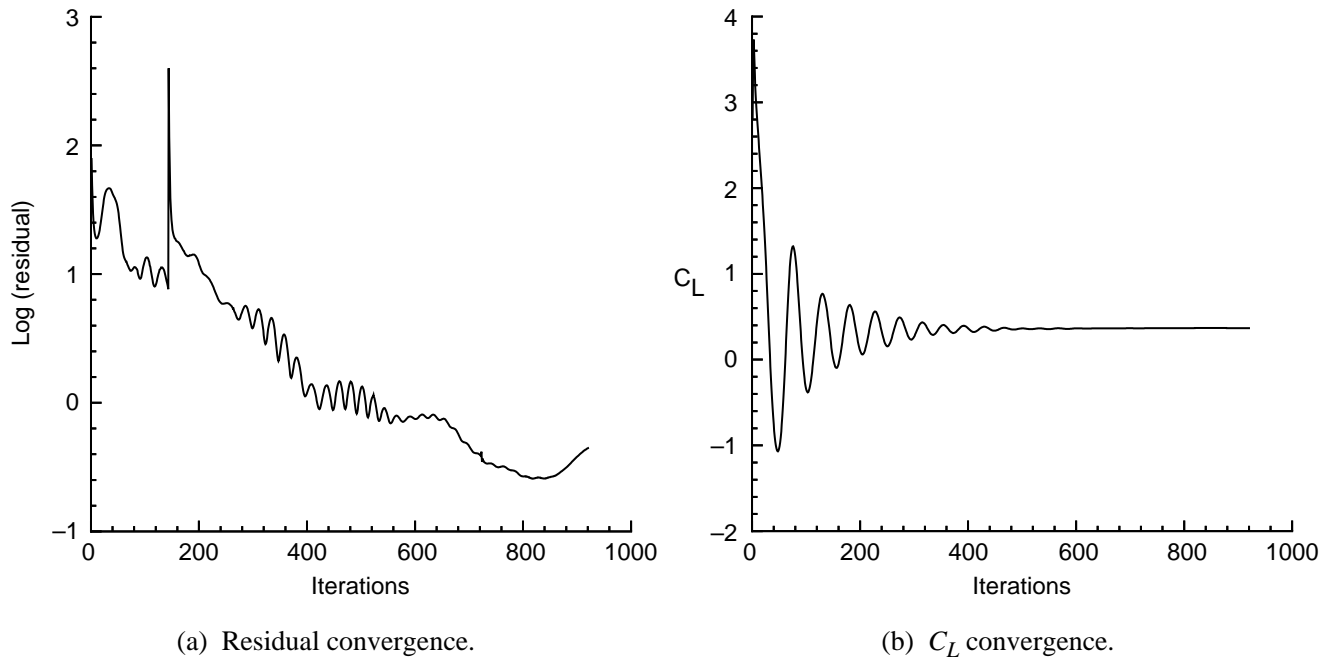
(b) C_L convergence.

Figure 14. Convergence characteristics of adapted medium grid for F-16XL without air dams, $\alpha = 10°$, $M = 0.148$.
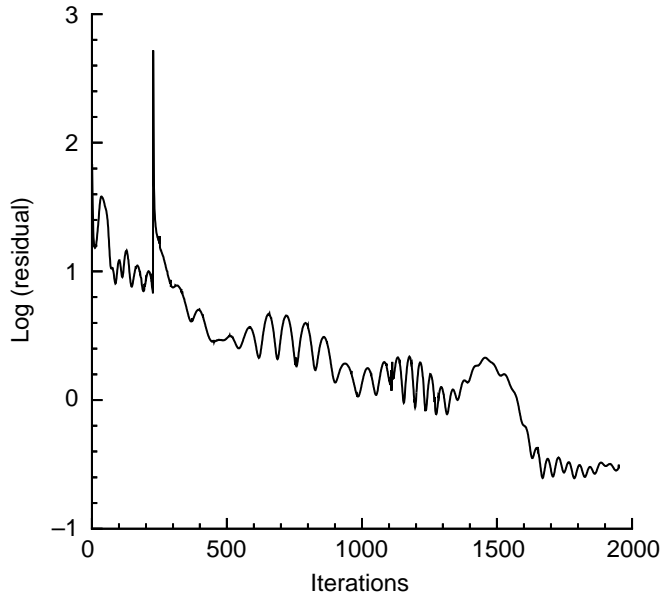
(a) Residual convergence.
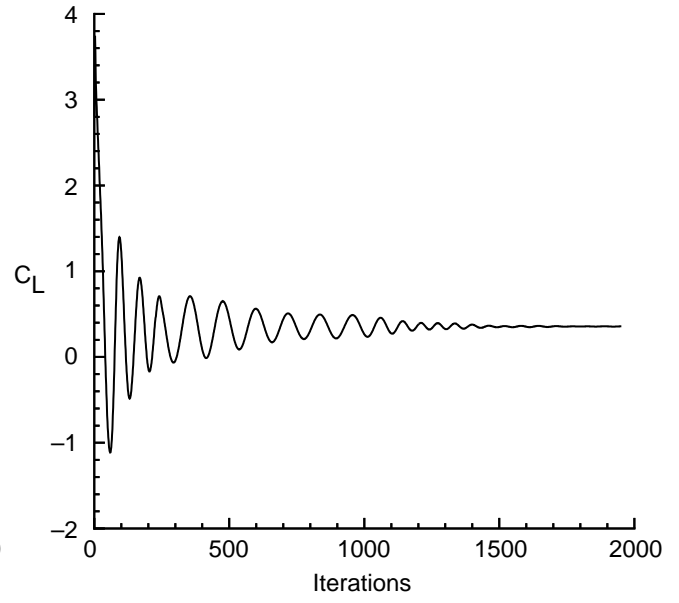
(b) C_L convergence.

Figure 15. Convergence characteristics for F-16XL with air dams, $\alpha = 10°$, $M = 0.148$.
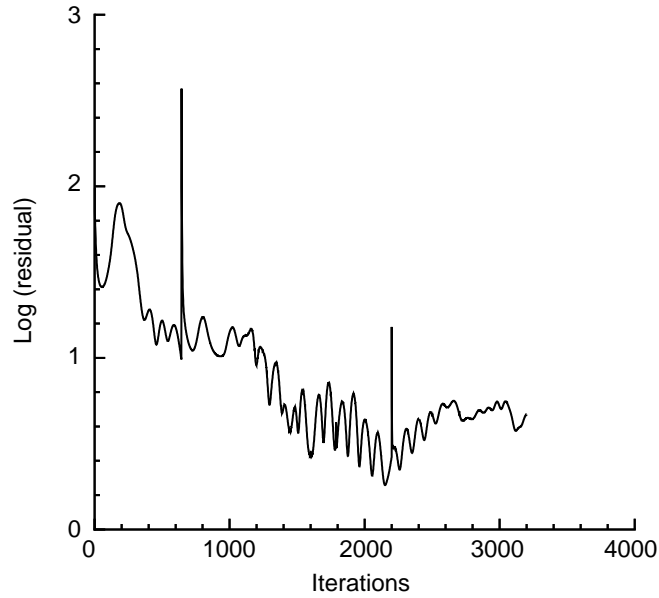
(a) Residual convergence.
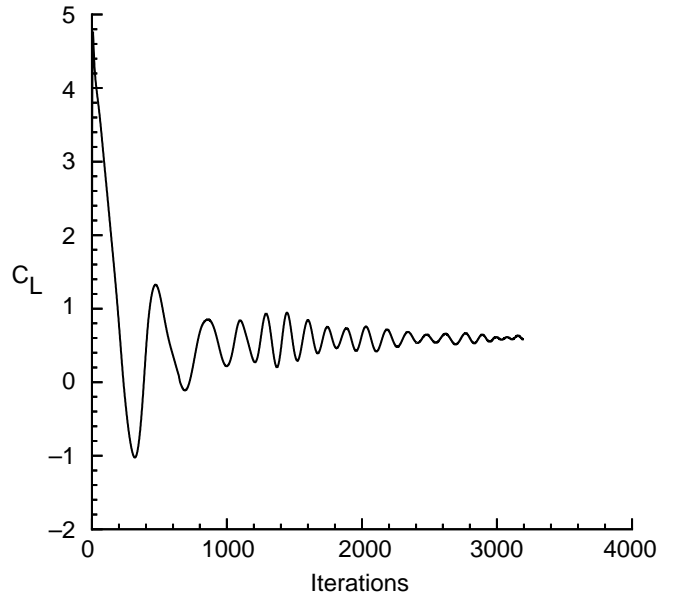
(b) C_L convergence.

Figure 16. Convergence characteristics for F-16XL with air dams, $\alpha = 15°$, $M = 0.148$.
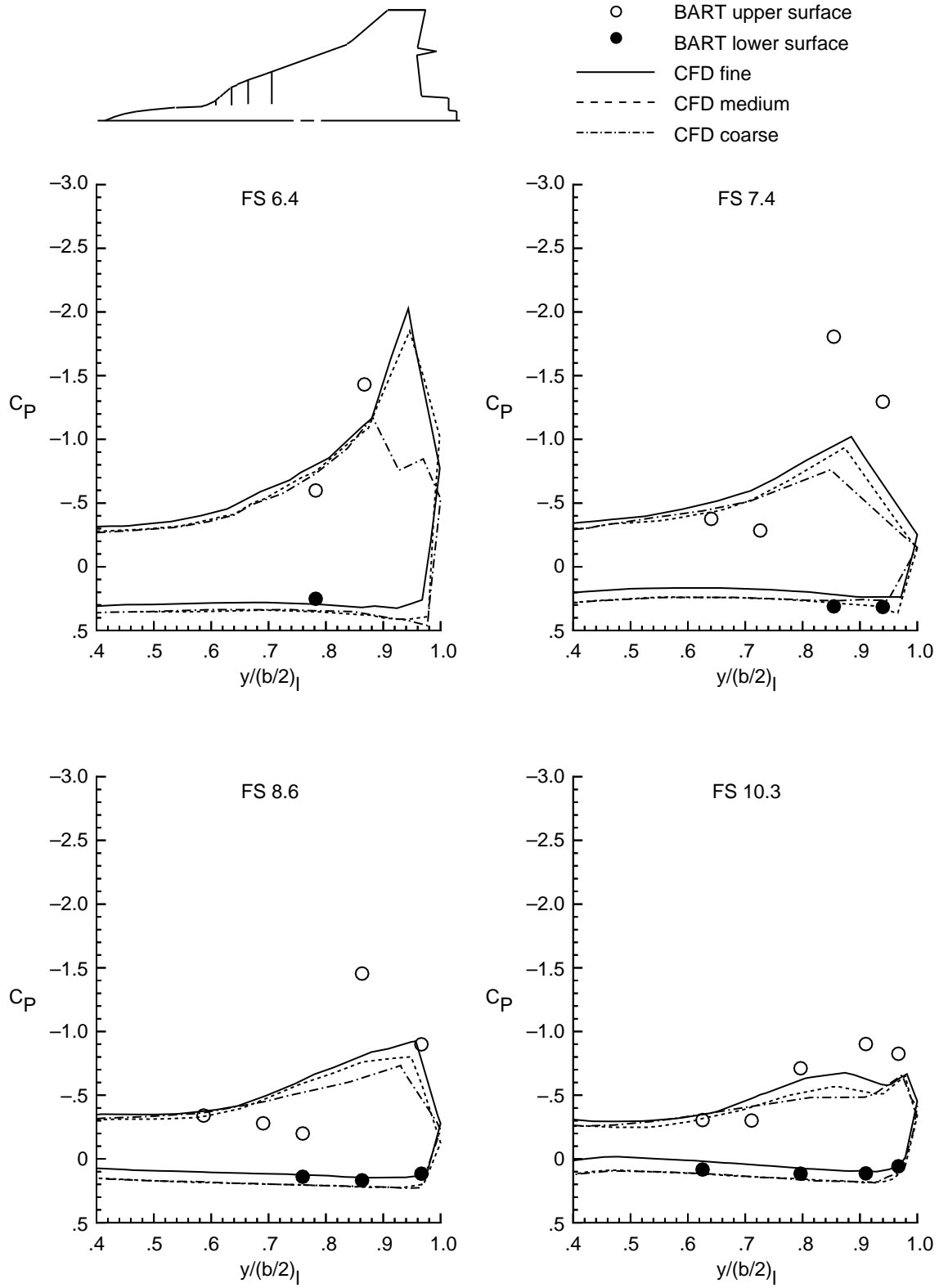
Figure 17. Computed spanwise C_P distributions from grid study compared to experiment for F-16XL without air dams, $\alpha = 10°$, $M = 0.148$.
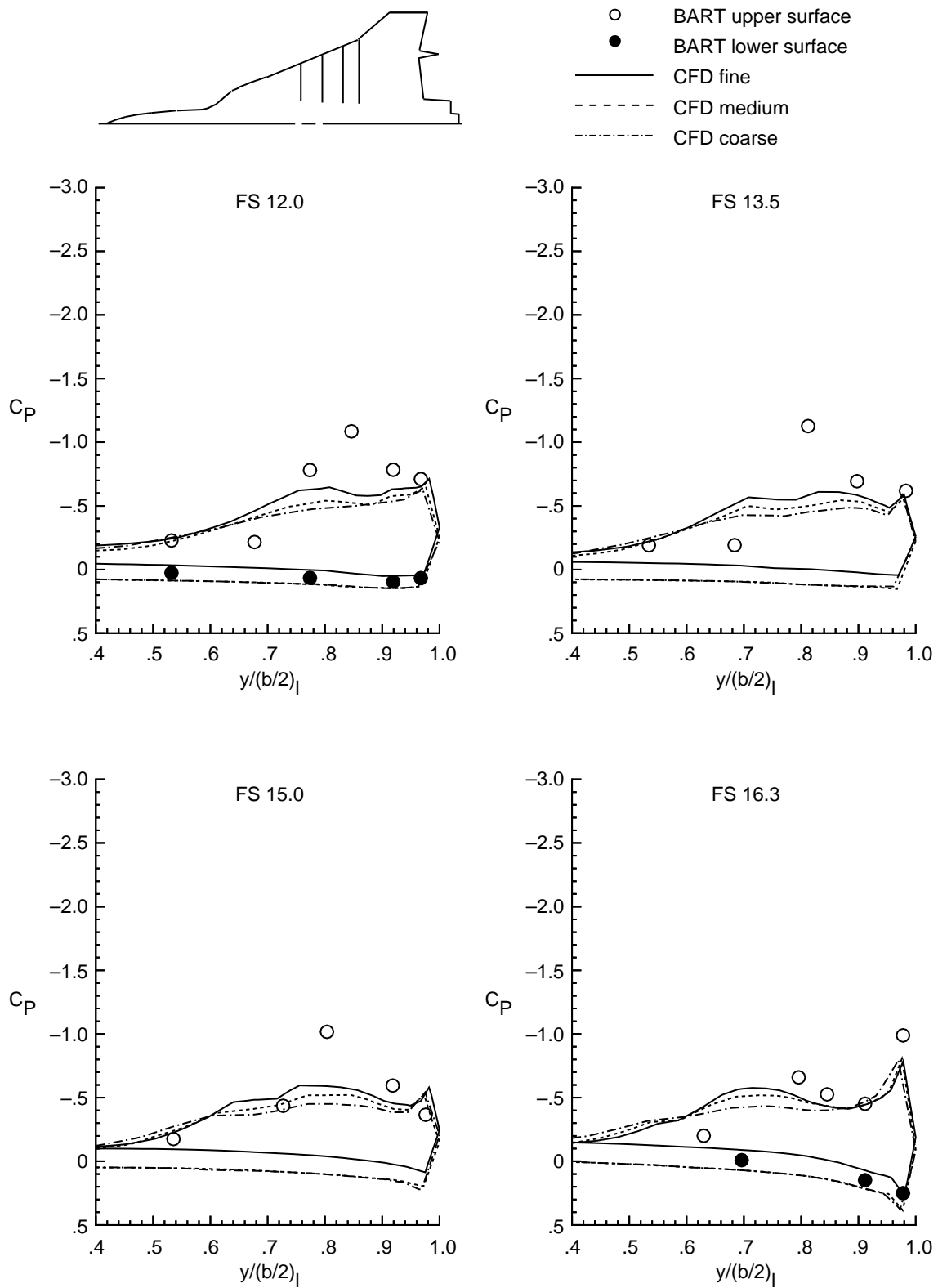
Figure 17. Continued.
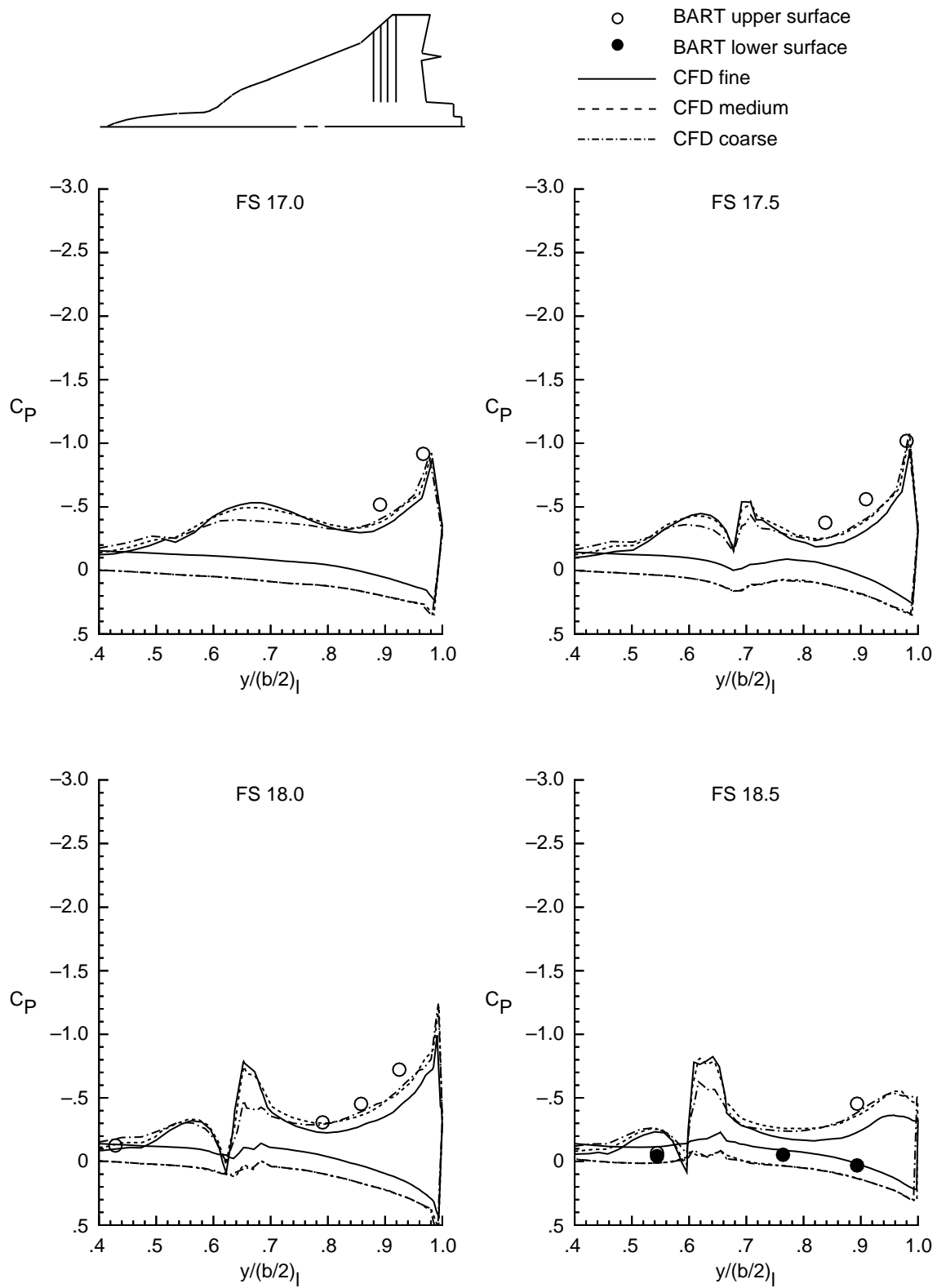
Figure 17. Continued.
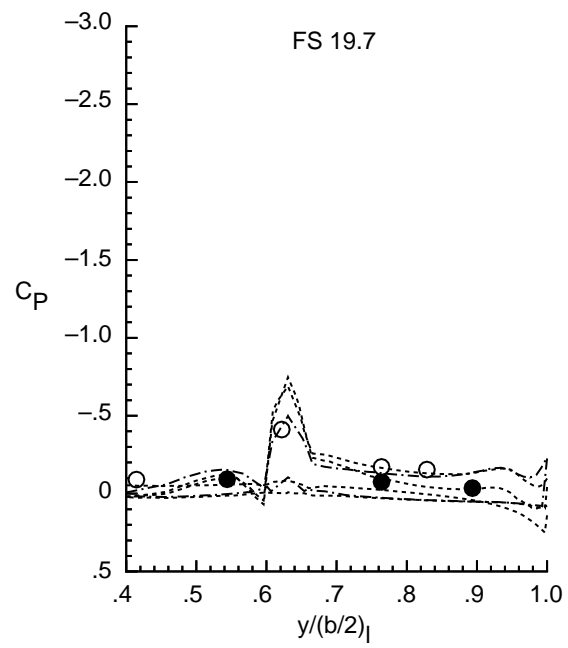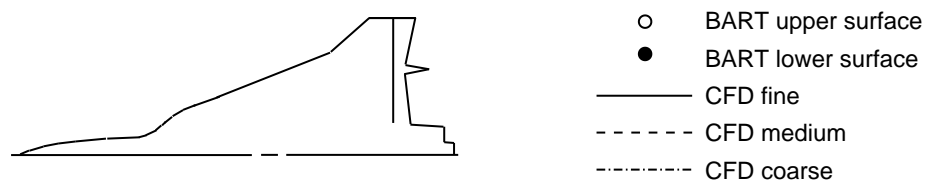
Figure 17. Concluded.
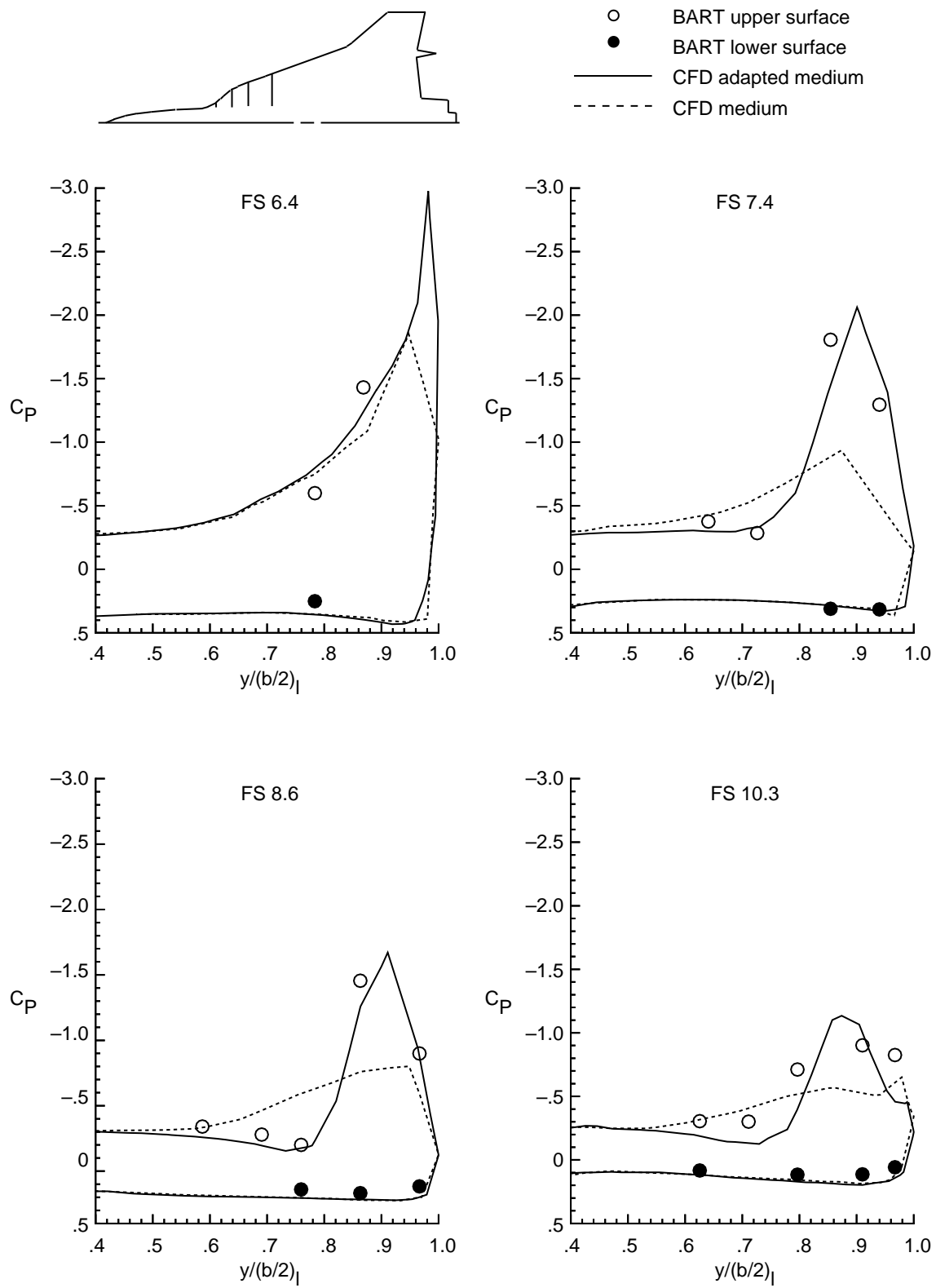
Figure 18. Computed spanwise C_P distributions from adapted and nonadapted grids compared to experiment for F-16XL without air dams, $\alpha = 10°$, $M = 0.148$.
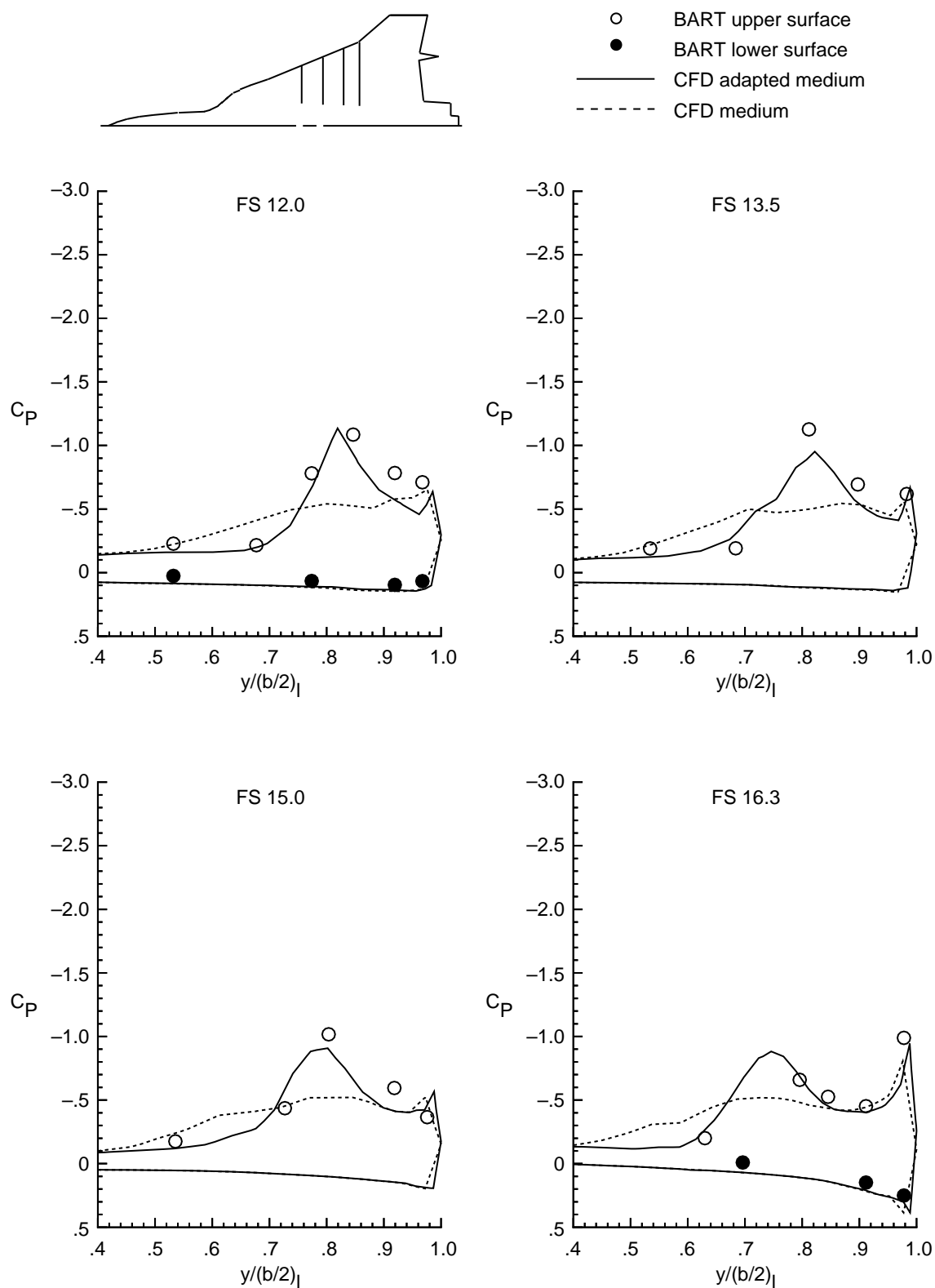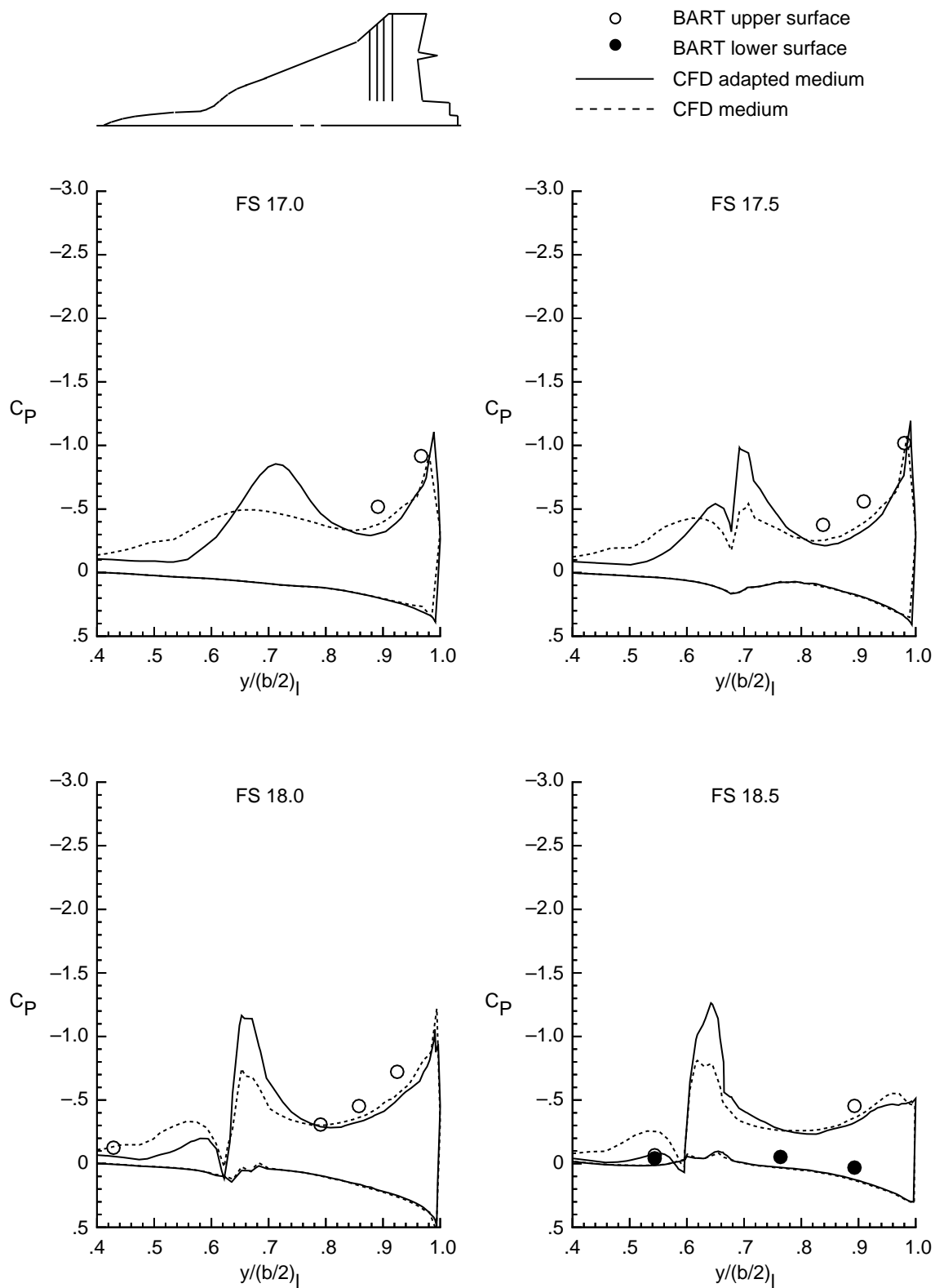
Figure 18. Continued.

Figure 18. Continued.

BART upper surface
BART lower surface
———— CFD adapted medium
- - - - - CFD medium

FS 19.7

C_P

−3.0
−2.5
−2.0
−1.5
−1.0
−.5
0
.5

.4   .5   .6   .7   .8   .9   1.0

$y/(b/2)_l$
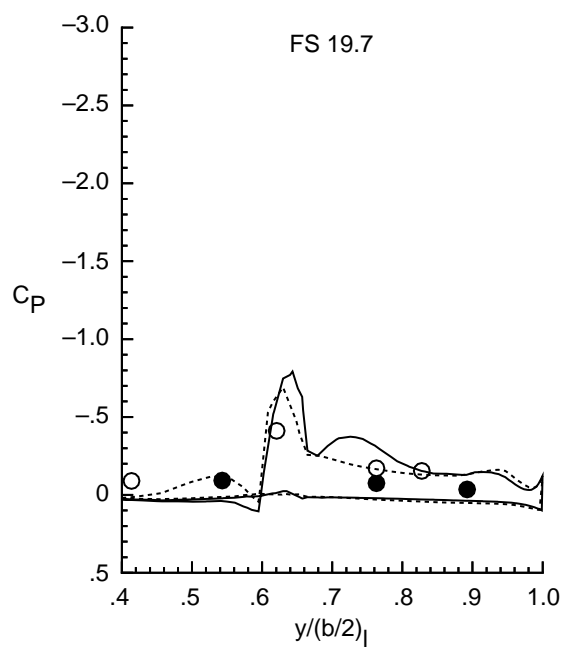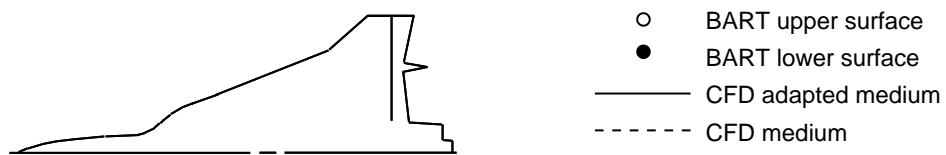
Figure 18. Concluded.
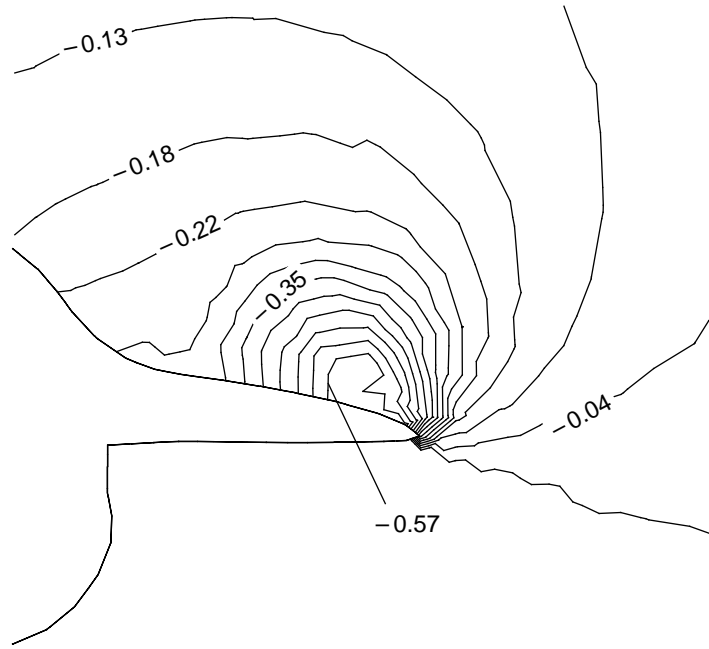
(a) Medium grid.
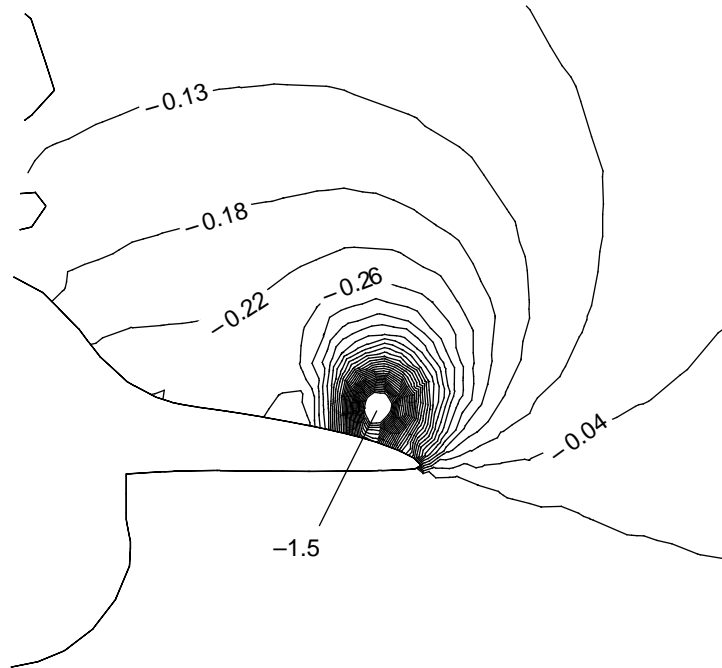
(b) Adapted medium grid.

Figure 19. Computed C_P contours for adapted and nonadapted grids at FS10.0 for F-16XL without air dams, $\alpha = 10°$, $M = 0.148$.
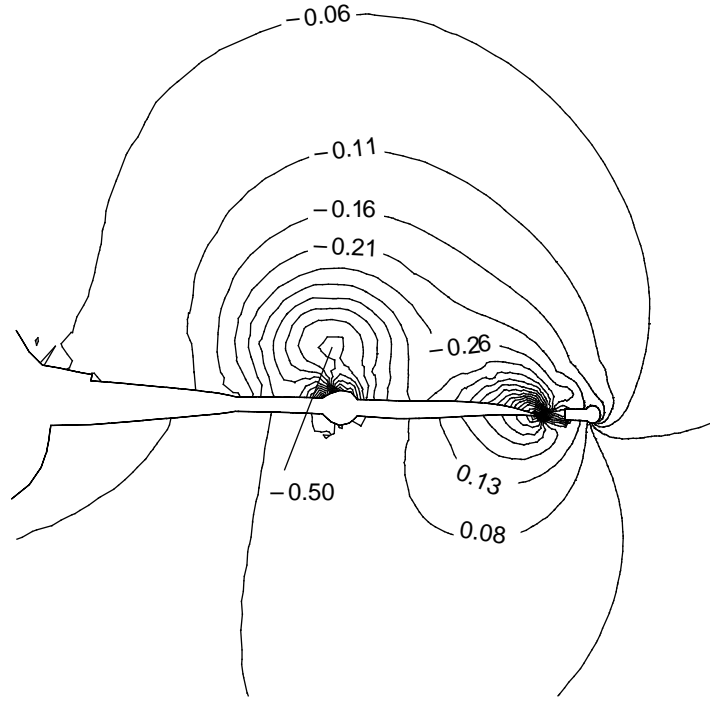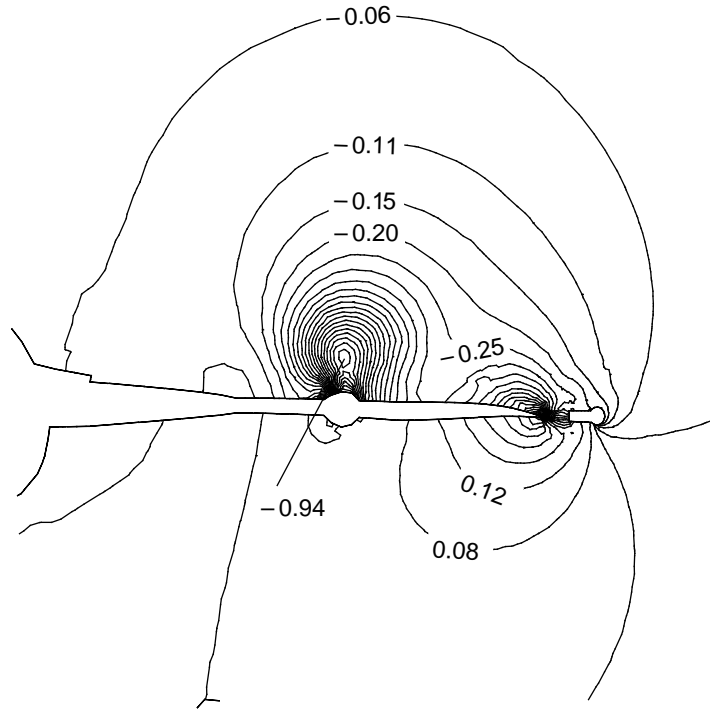
(a) Medium grid.

(b) Adapted medium grid.

Figure 20. Computed C_P contours for adapted and nonadapted grids at FS18.0 for F-16XL without air dams, $\alpha = 10°$, $M = 0.148$.
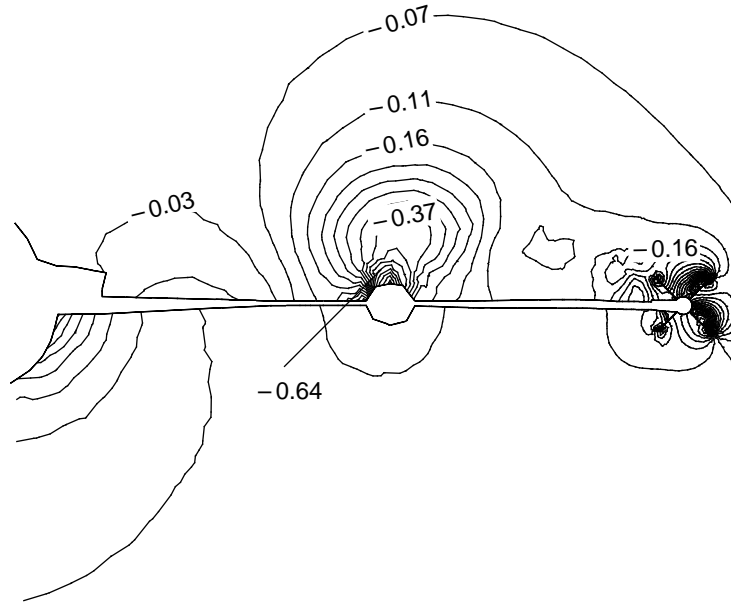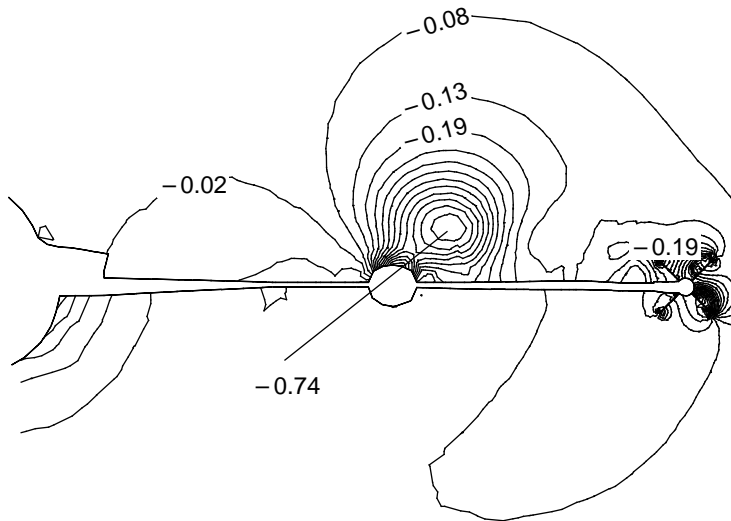
(a) Medium grid.

(b) Adapted medium grid.

Figure 21. Computed C_P contours for adapted and nonadapted grids at FS19.7 for F-16XL without air dams, $\alpha = 10°$, $M = 0.148$.
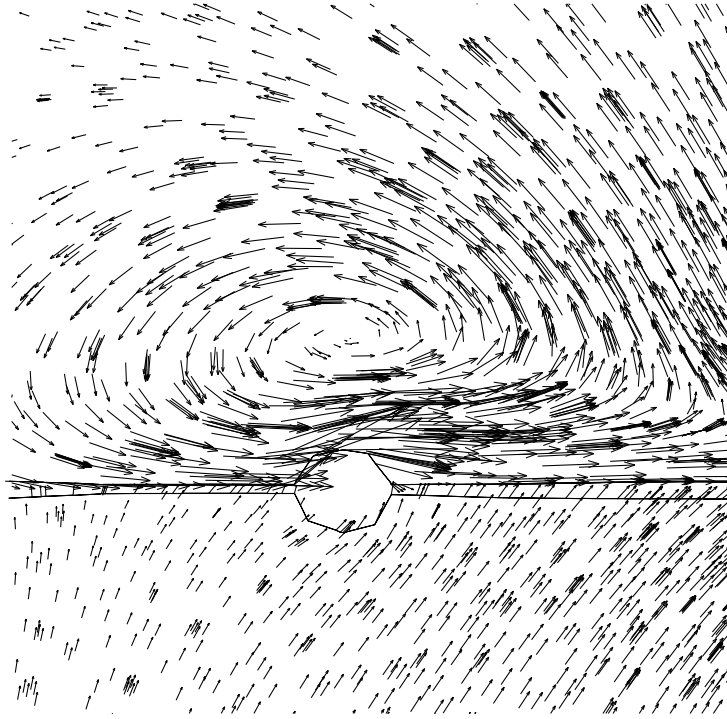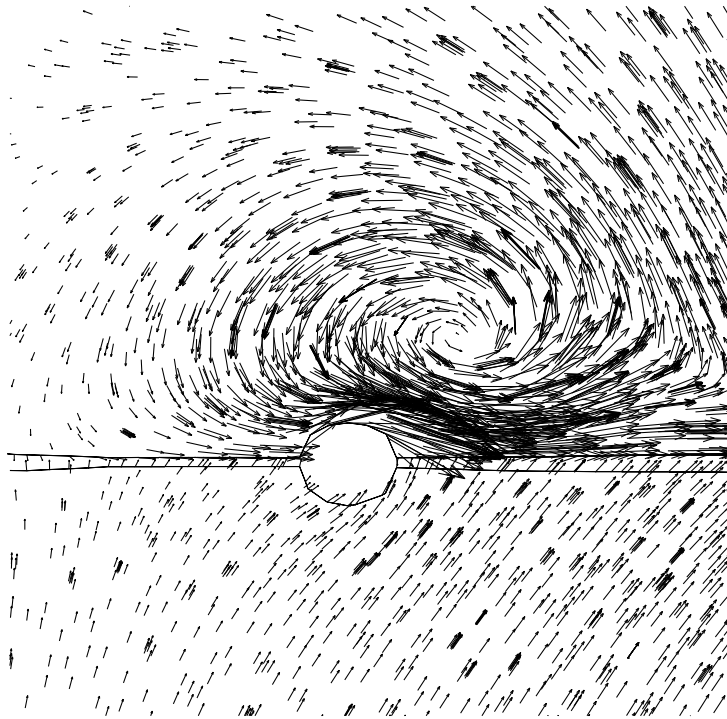
(a) Medium grid.

(b) Adapted medium grid.

Figure 22. Computed velocity vectors for adapted and nonadapted grids at FS19.7 for F-16XL without air dams, $\alpha = 10°$, $M = 0.148$.
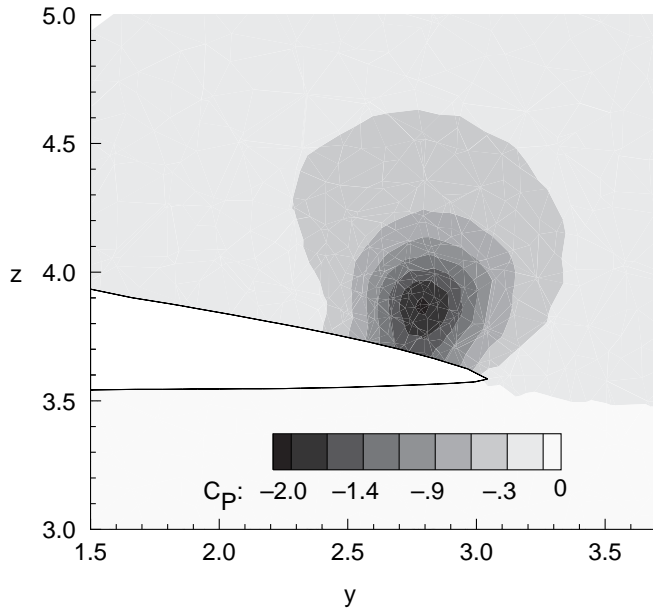
(a) Computed C_P contours.
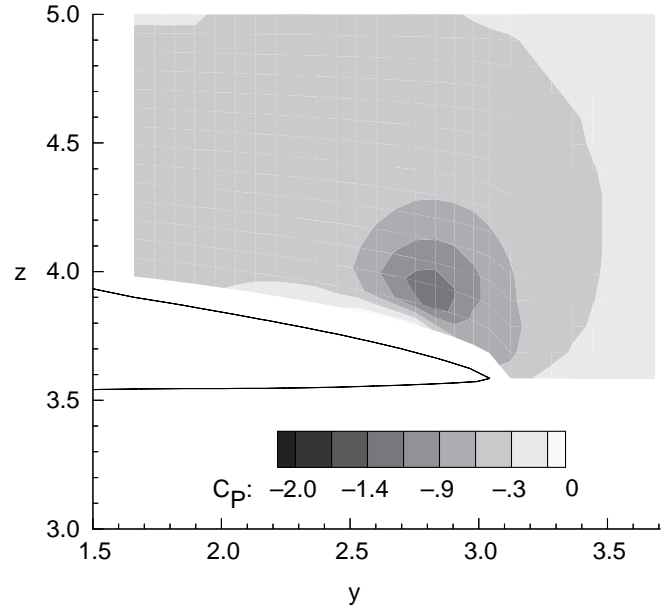
(b) Experimental C_P contours.

Figure 23. Computed and measured C_P contours at FS9.0 for F-16XL without air dams, $\alpha = 10°$, $M = 0.148$.
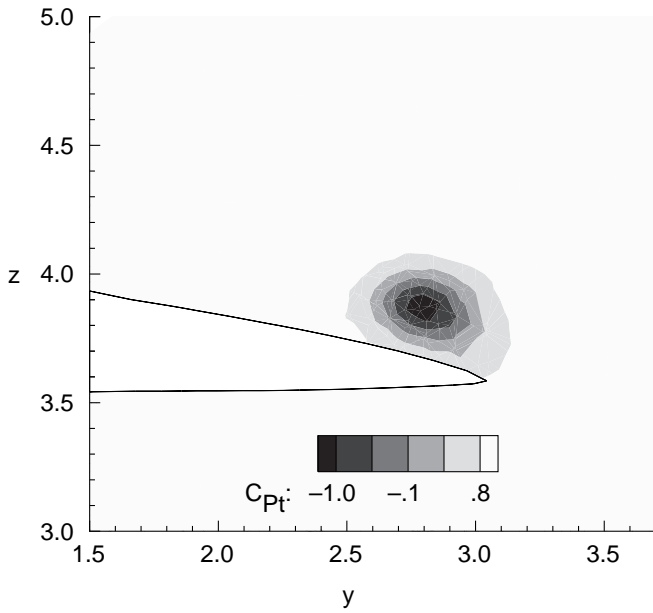
(a) Computed C_P contours.
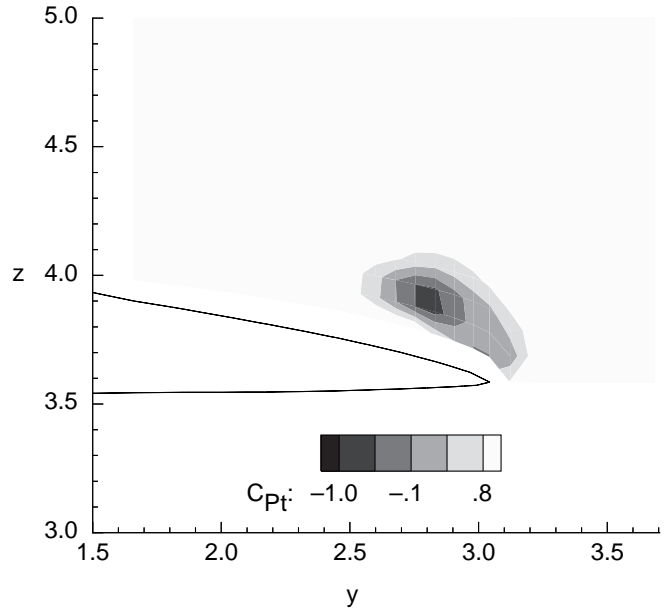
(b) Experimental C_P contours.

Figure 24. Computed and measured $C_{P,t}$ contours at FS9.0 for F-16XL without air dams, $\alpha = 10°$, $M = 0.148$.
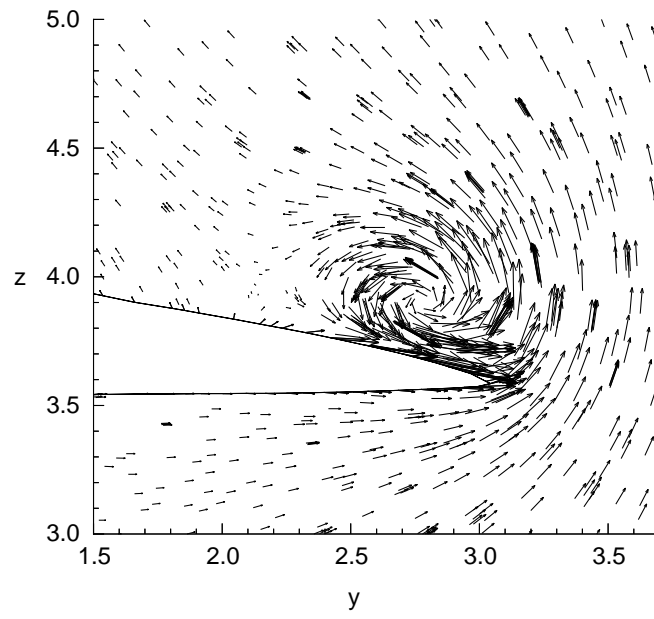
(a) Computed velocity vectors.
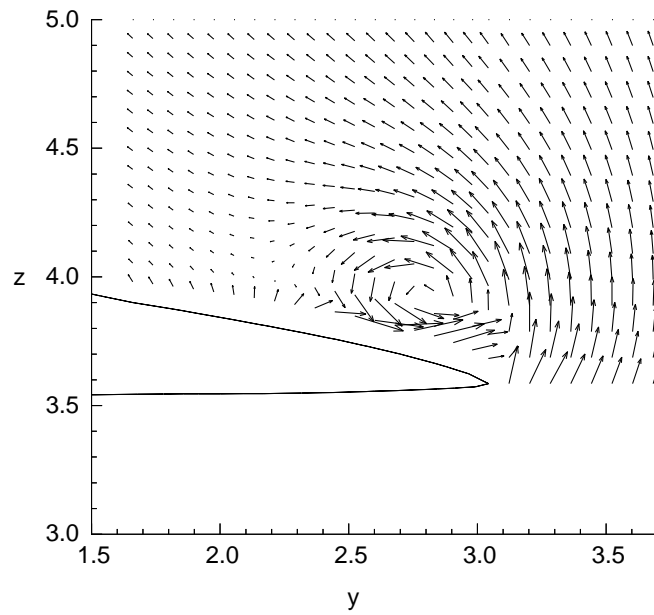
(b) Experimental velocity vectors.

Figure 25. Computed and measured velocity vectors at FS9.0 for F-16XL without air dams, $\alpha = 10°$, $M = 0.148$.
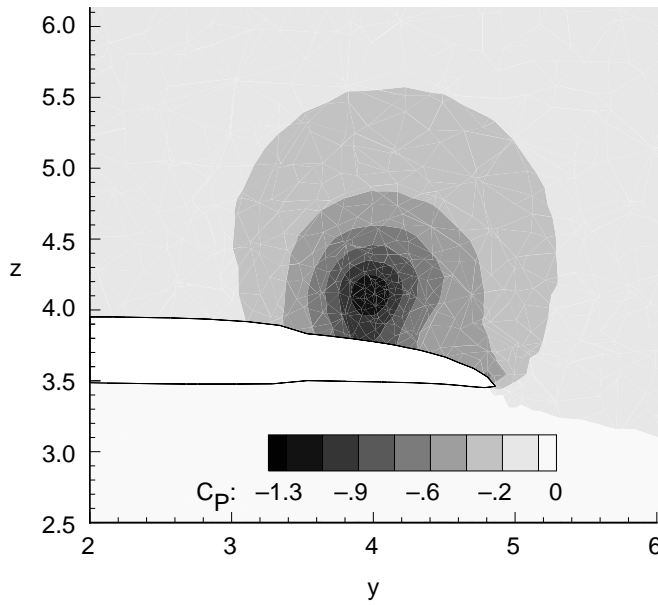
(a) Computed C_P contours.
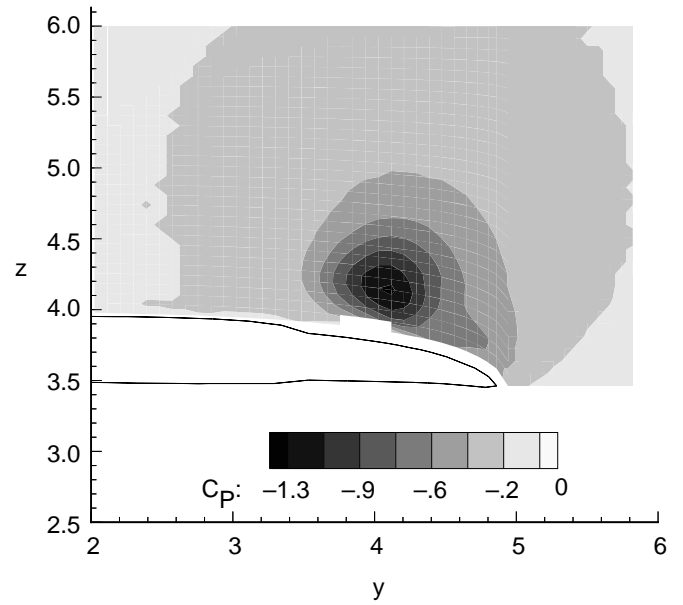
(b) Experimental C_P contours.

Figure 26. Computed and measured C_P contours at FS14.0 for F-16XL without air dams, $\alpha = 10°$, $M = 0.148$.
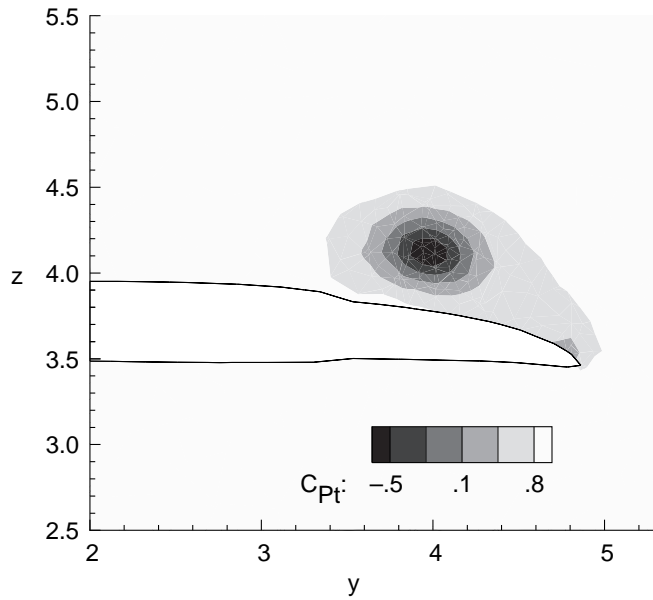
(a) Computed $C_{P,t}$ contours.
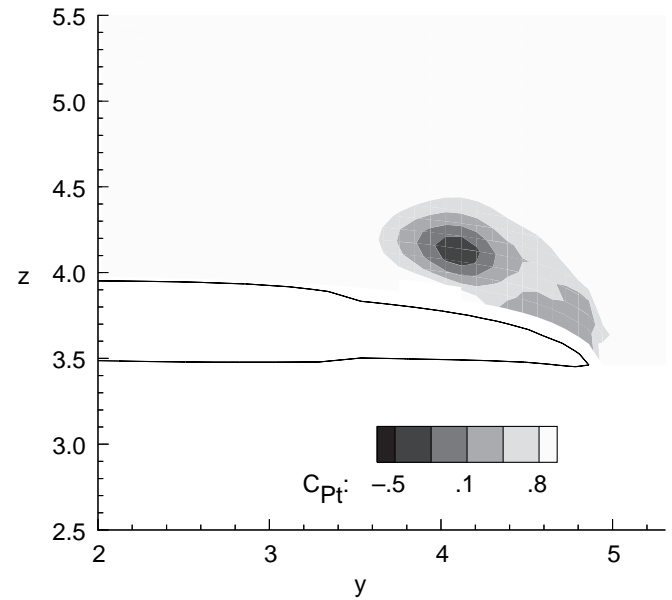
(b) Experimental $C_{P,t}$ contours.

Figure 27. Computed and measured $C_{P,t}$ contours at F14.0 for F-16XL without air dams, $\alpha = 10°$, $M = 0.148$.
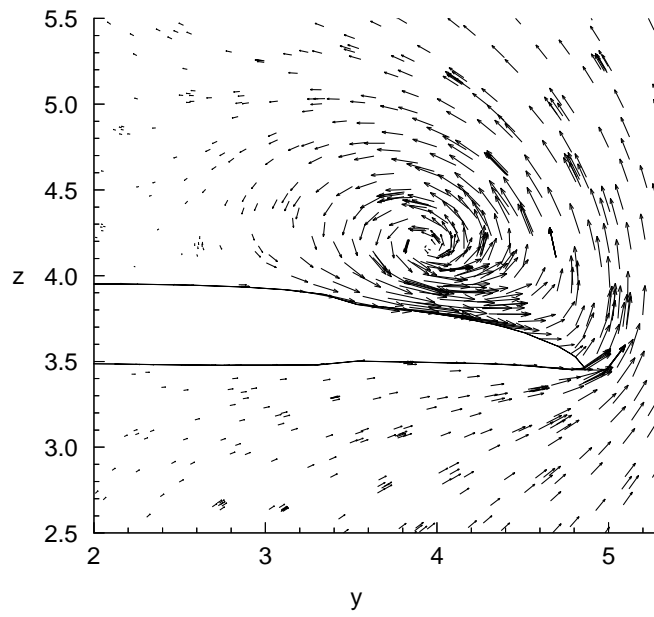
(a) Computed velocity vectors.
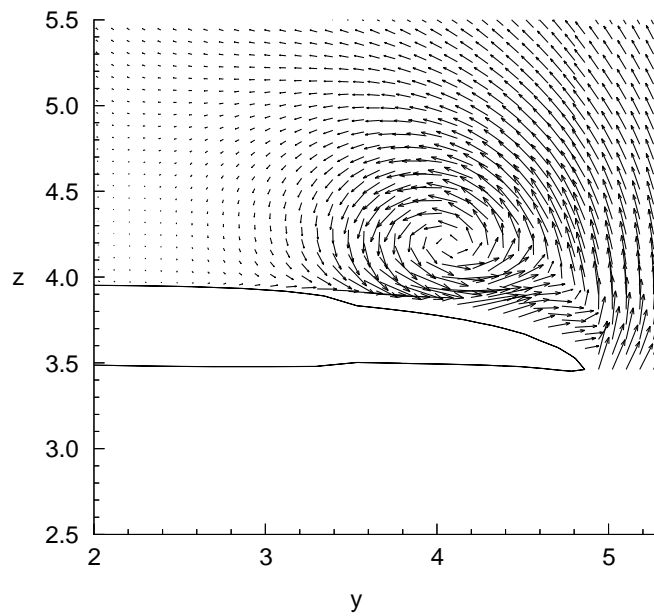
(b) Experimental velocity vectors.

Figure 28. Computed and measured velocity vectors at F14.0 for F-16XL without air dams, $\alpha = 10°$, $M = 0.148$.
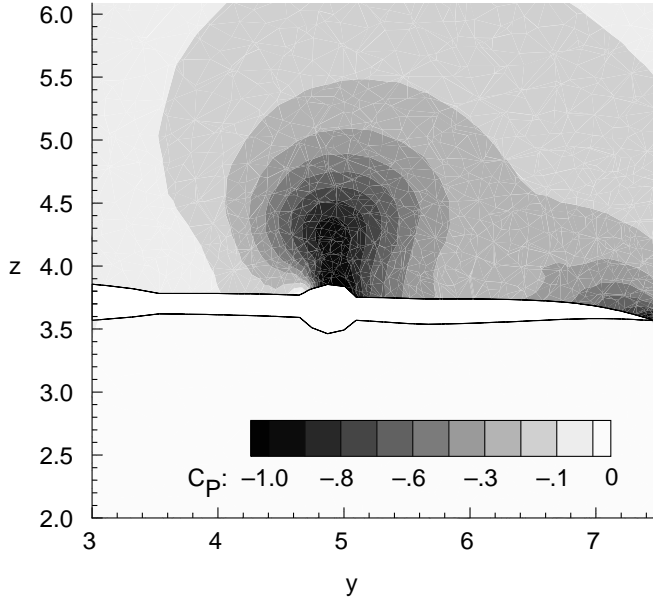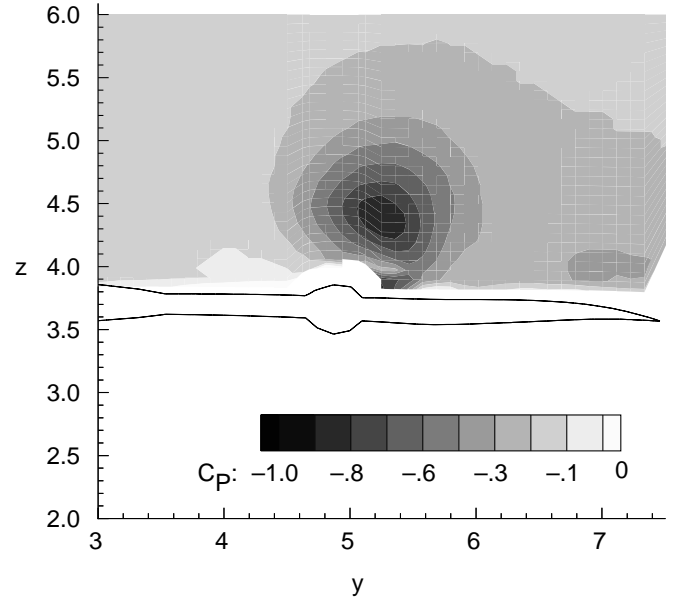
(a) Computed C_P contours.　　　　　　(b) Experimental C_P contours.

Figure 29. Computed and measured C_P contours at FS18.0 for F-16XL without air dams, $\alpha = 10°$, $M = 0.148$.
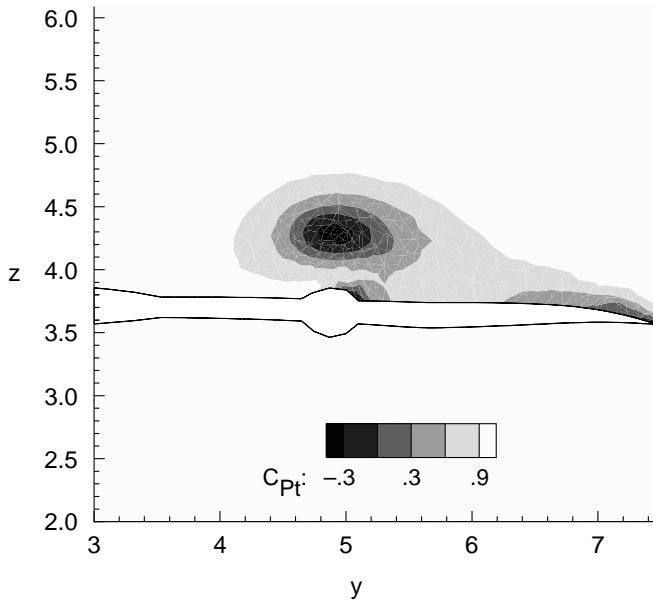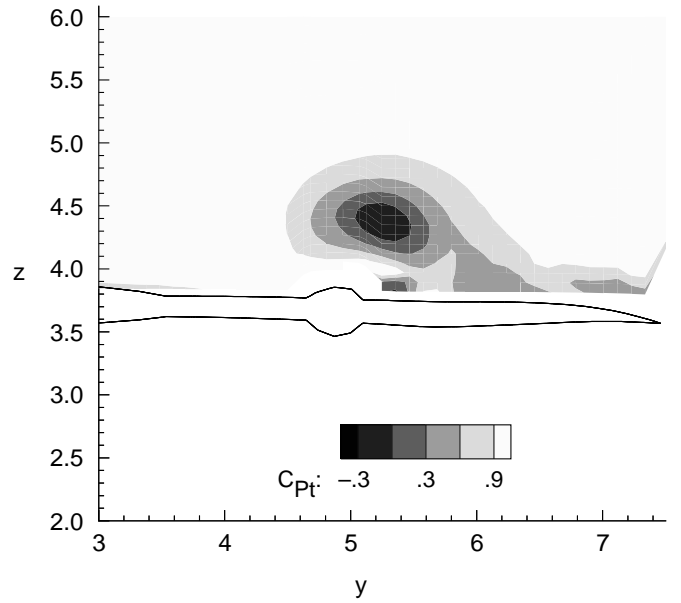
(a) Computed $C_{P,t}$ contours.　　　　　　(b) Experimental $C_{P,t}$ contours.

Figure 30. Computed and measured $C_{P,t}$ contours at FS18.0 for F-16XL without air dams, $\alpha = 10°$, $M = 0.148$.
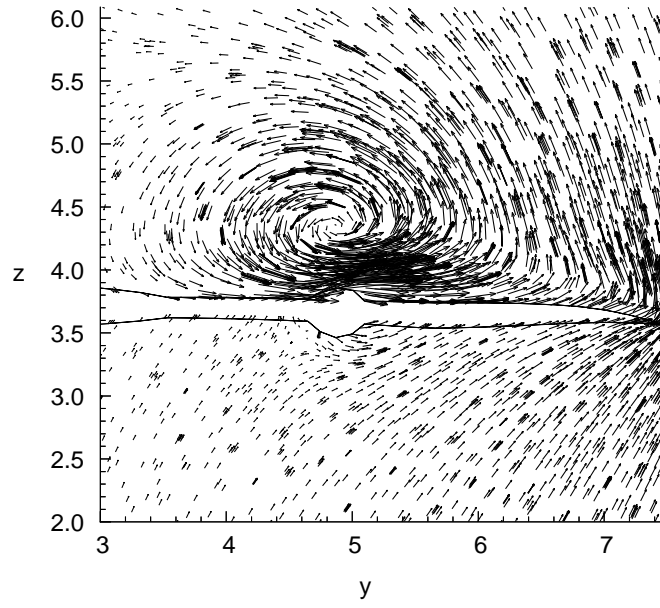
(a) Computed velocity vectors.
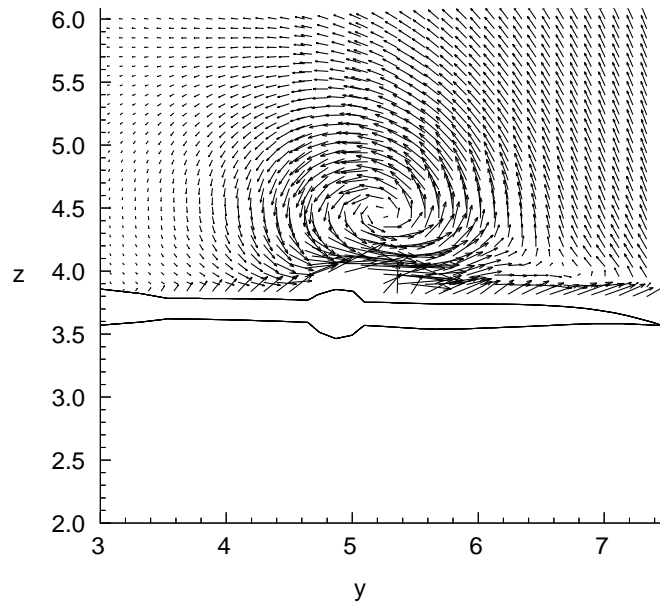
(b) Experimental velocity vectors.

Figure 31. Computed and measured velocity vectors at FS18.0 for F-16XL without air dams, $\alpha = 10°$, $M = 0.148$.
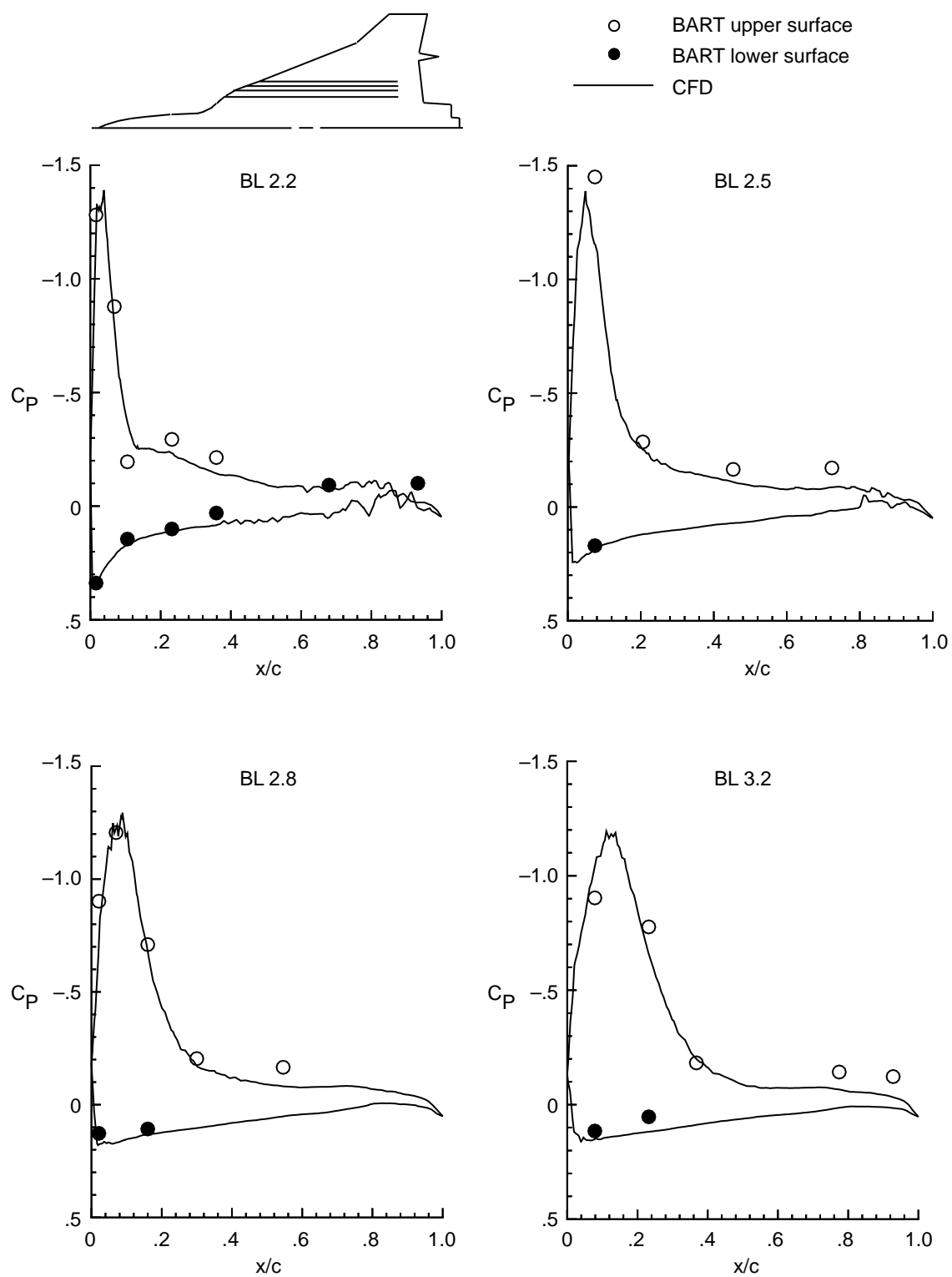
Figure 32. Streamwise distributions of experimental and computational C_P for F-16XL with air dams, $\alpha = 10°$, $M = 0.148$.
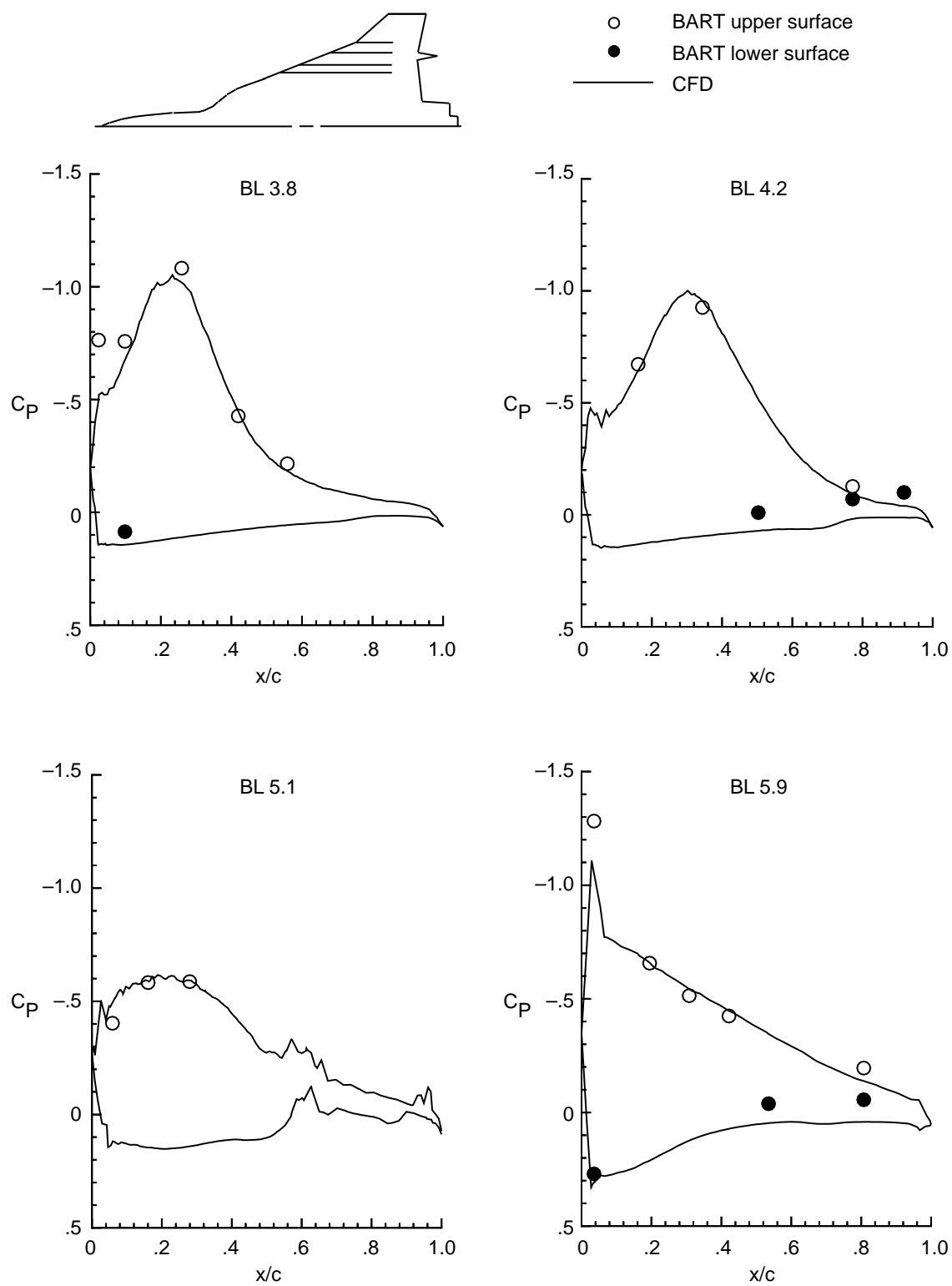
Figure 32. Continued.
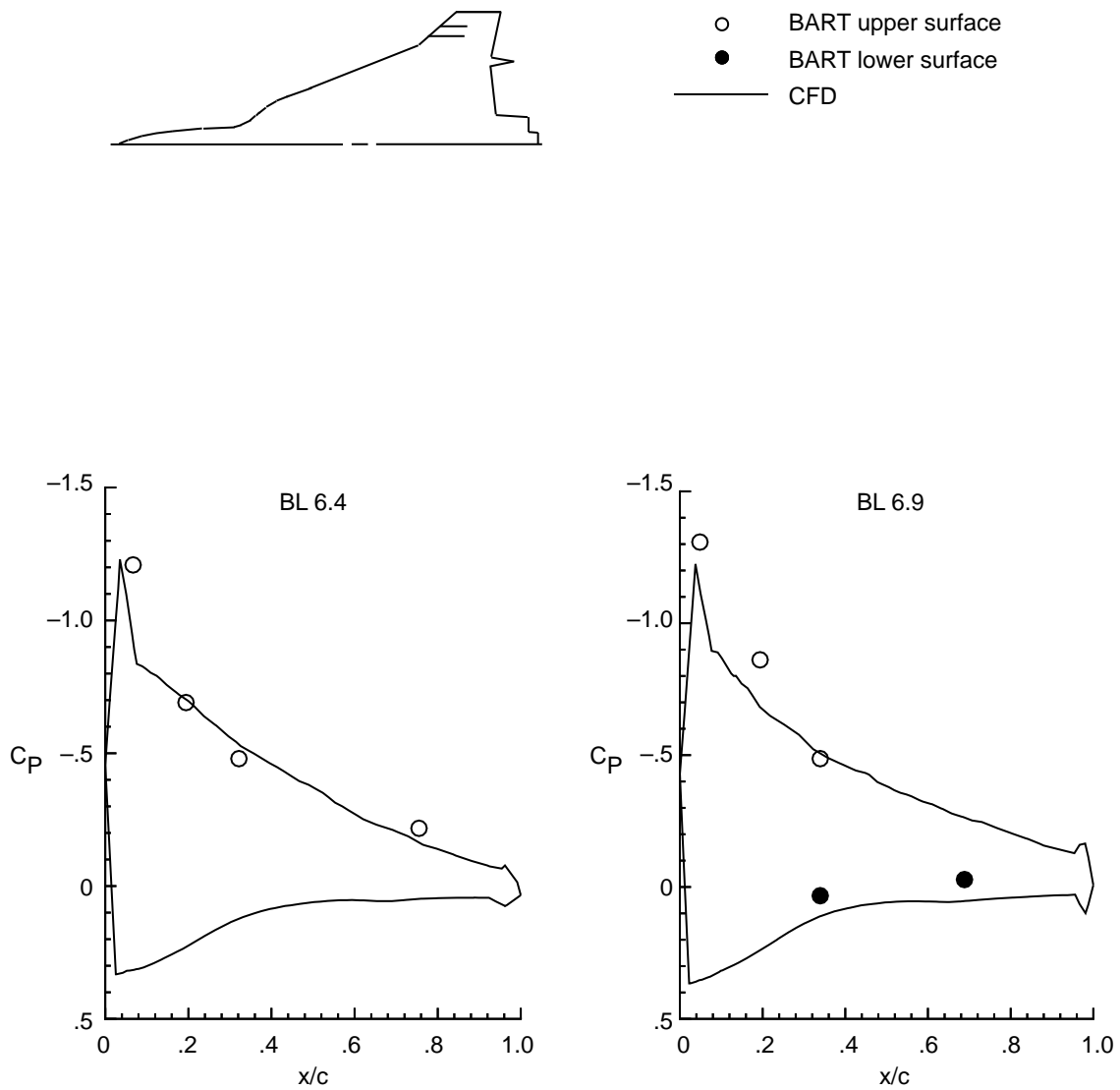
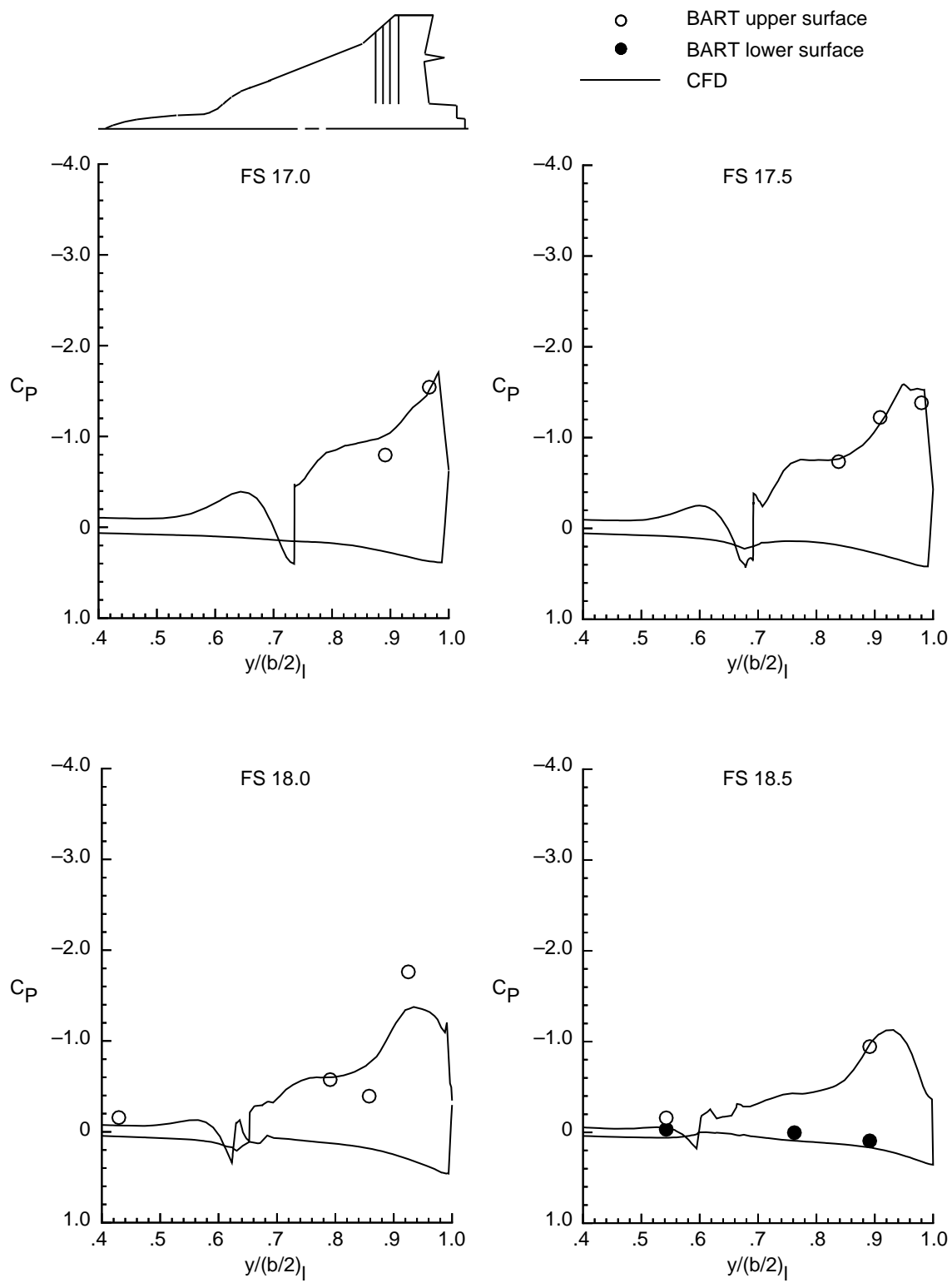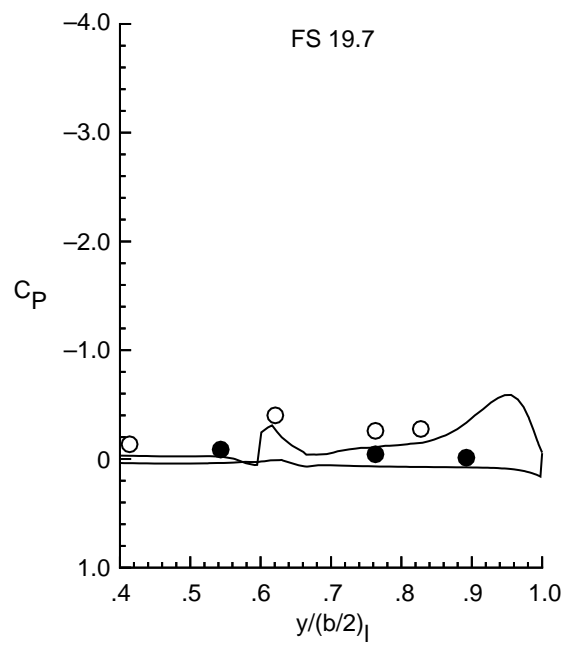Figure 32. Concluded.
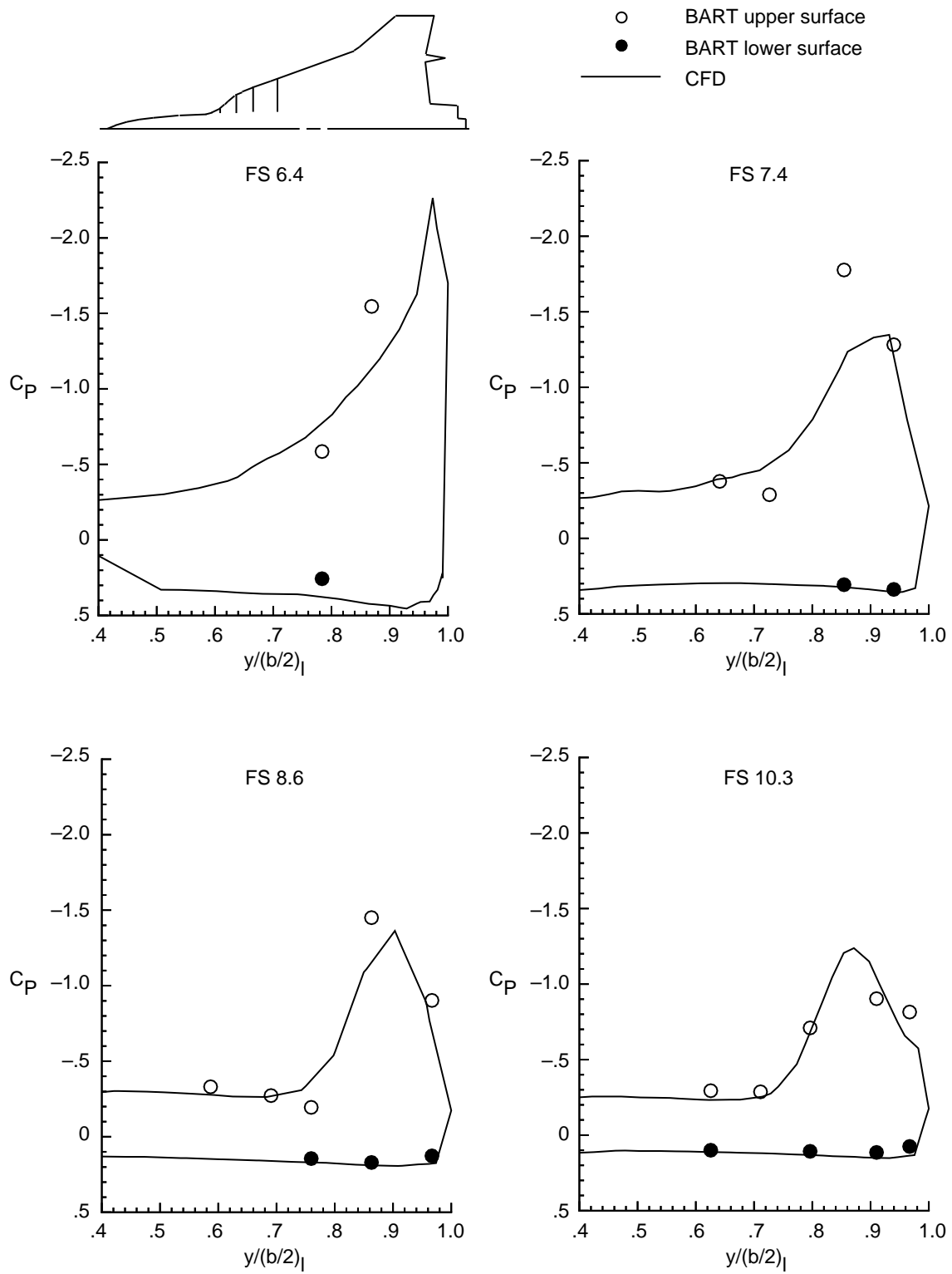
Figure 33. Spanwise distributions of experimental and computational C_P for F-16XL with air dams, $\alpha = 10°$, $M = 0.148$.
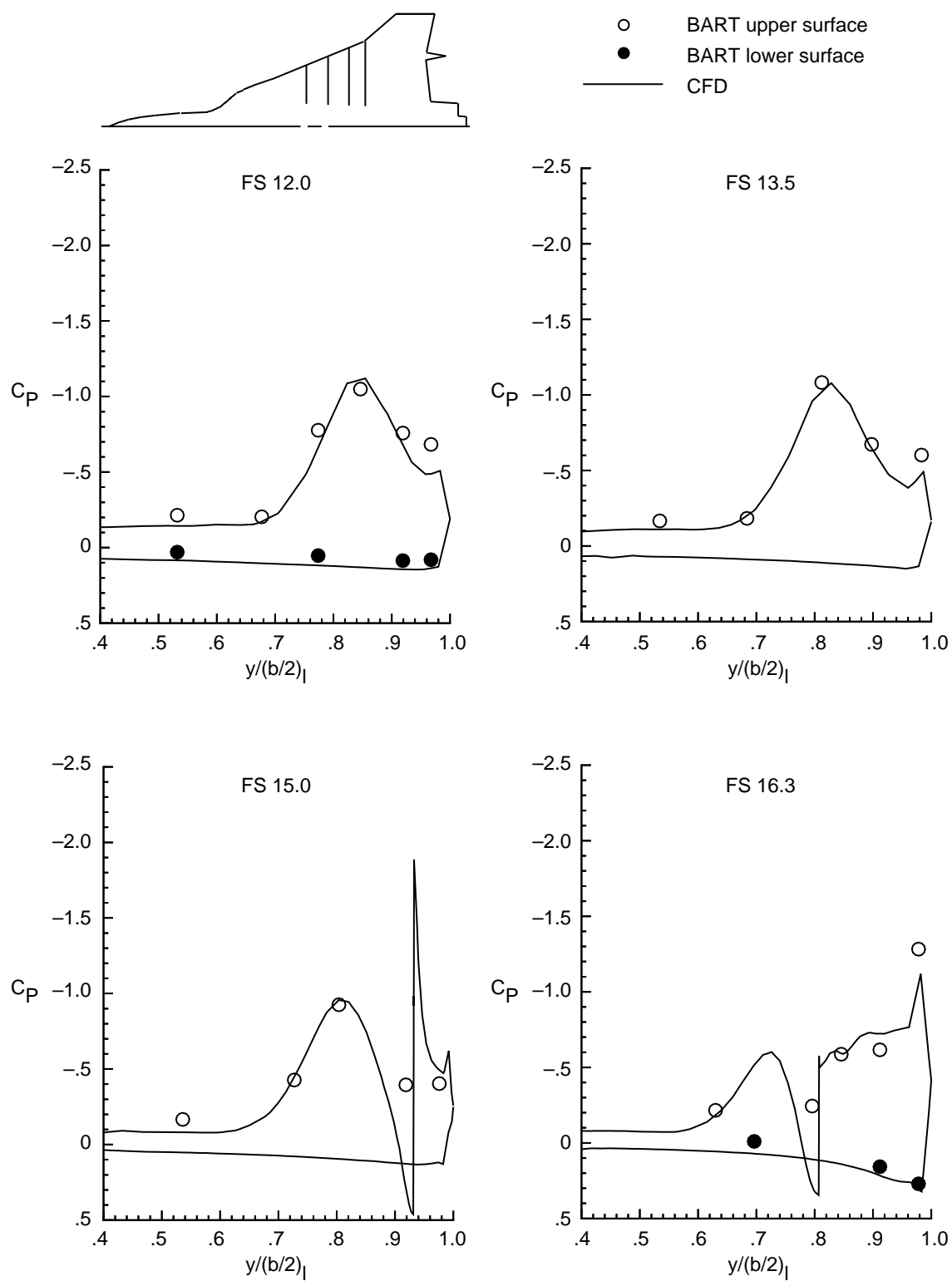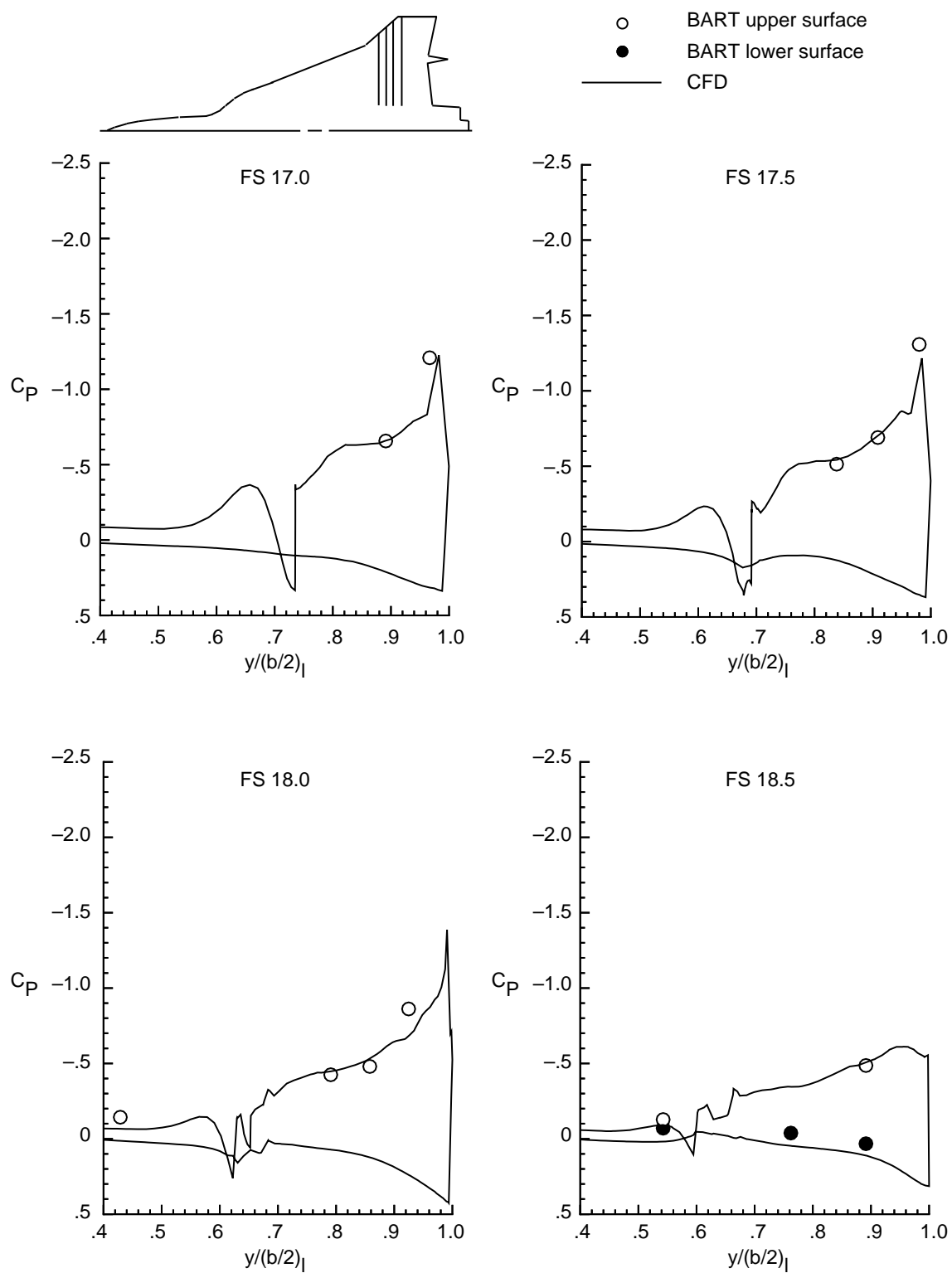
Figure 33. Continued.

Figure 33. Continued.

FS 19.7

○   BART upper surface
●   BART lower surface
─── CFD
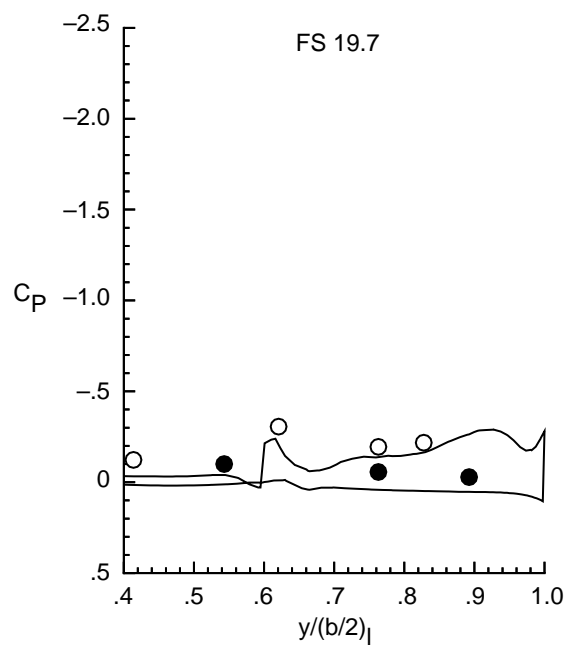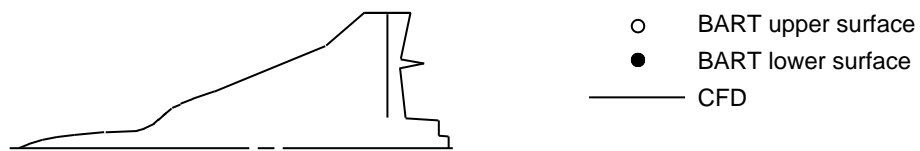
Figure 33. Concluded.
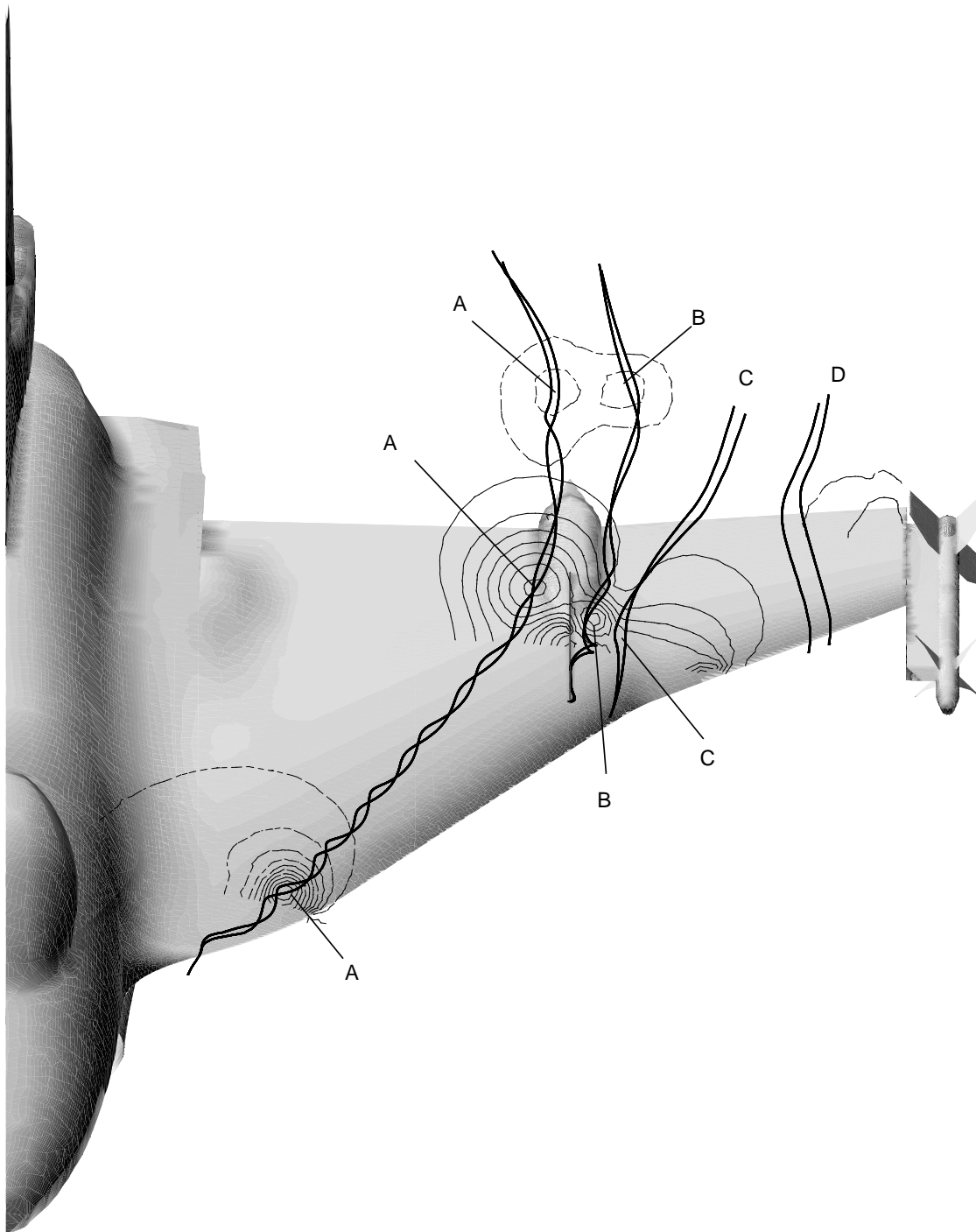
Figure 34. Computed off-surface particle traces for F-16XL with air dams, $\alpha = 10°$, $M = 0.148$.
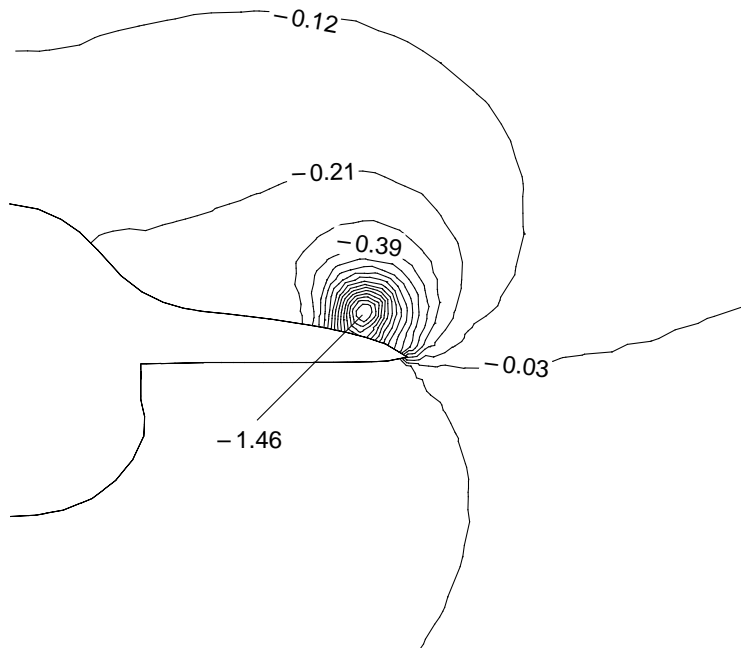
(a) Computed C_P contours.
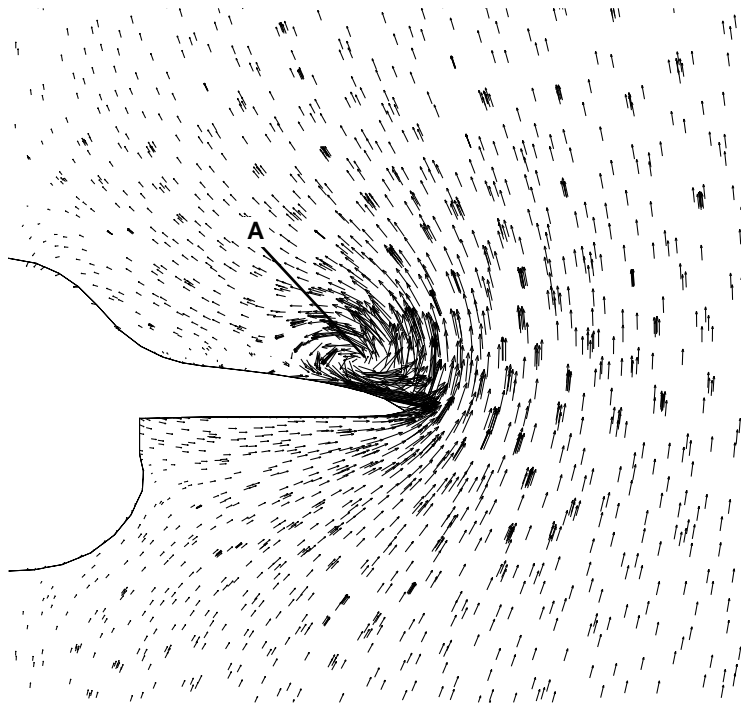
(b) Computed velocity vectors.

Figure 35. Computed C_P contours and velocity vectors at FS10.0 for F-16XL with air dams, $\alpha = 10°$, $M = 0.148$.
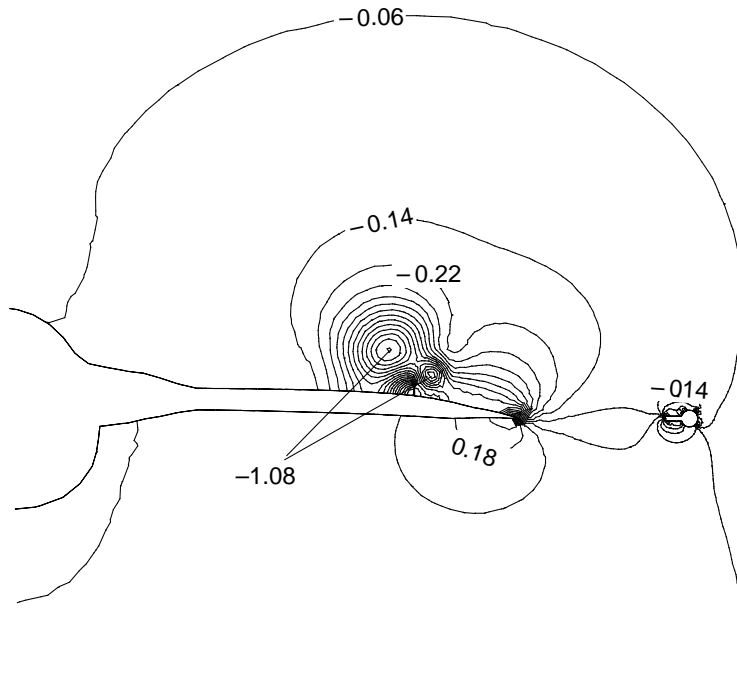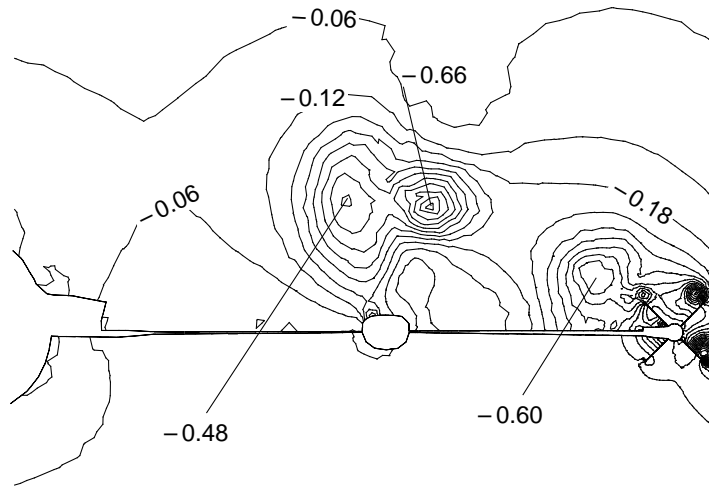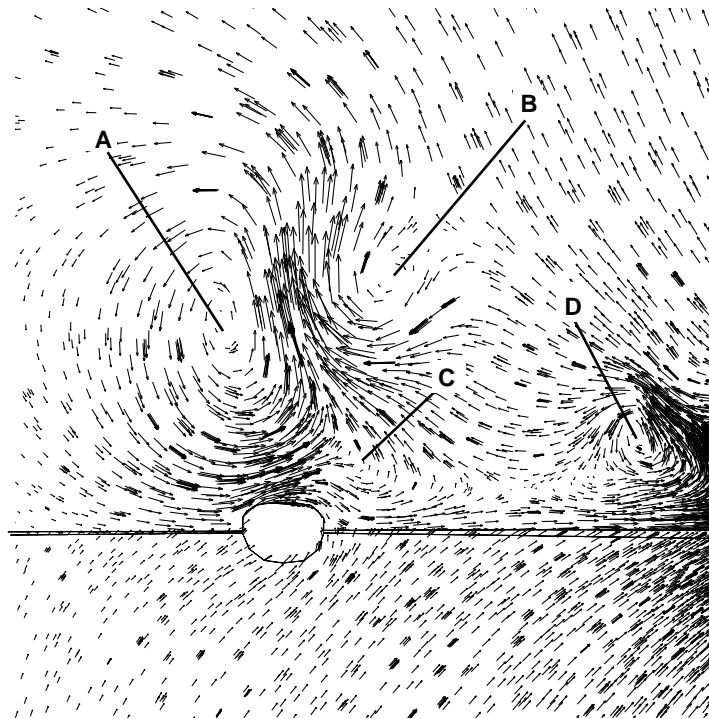
(a) Computed C_P contours.
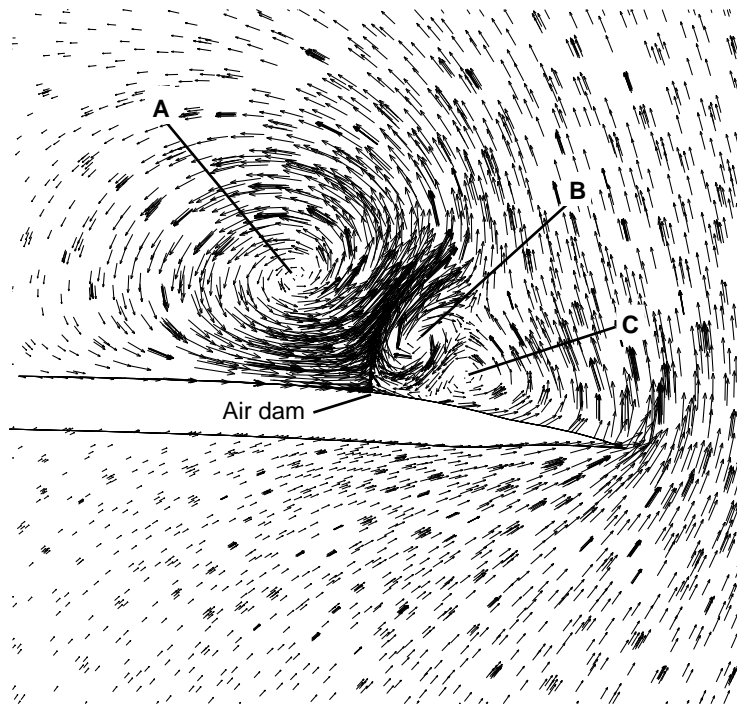
(b) Close-up view of computed velocity vectors.

Figure 36. Computed C_P contours and velocity vectors at FS16.3 for F-16XL with air dams, $\alpha = 10°$, $M = 0.148$.
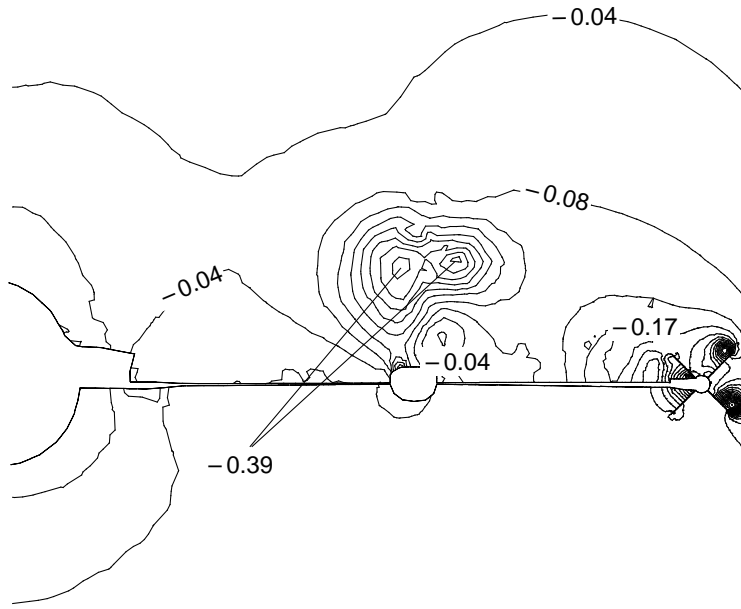
(a) Computed C_P contours.
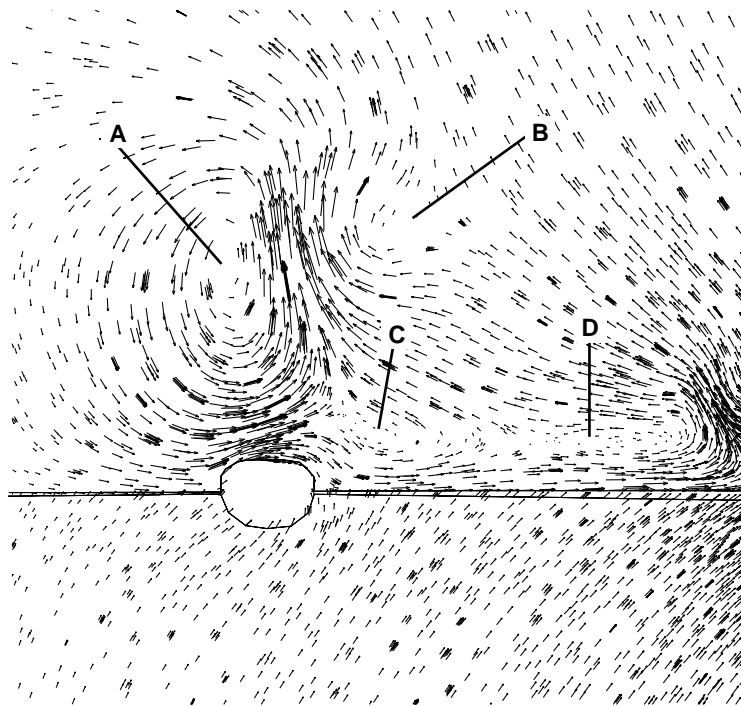
(b) Close-up view of computed velocity vectors.

Figure 37. Computed C_P contours and velocity vectors at FS20.2 for F-16XL with air dams, $\alpha = 10°$, $M = 0.148$.
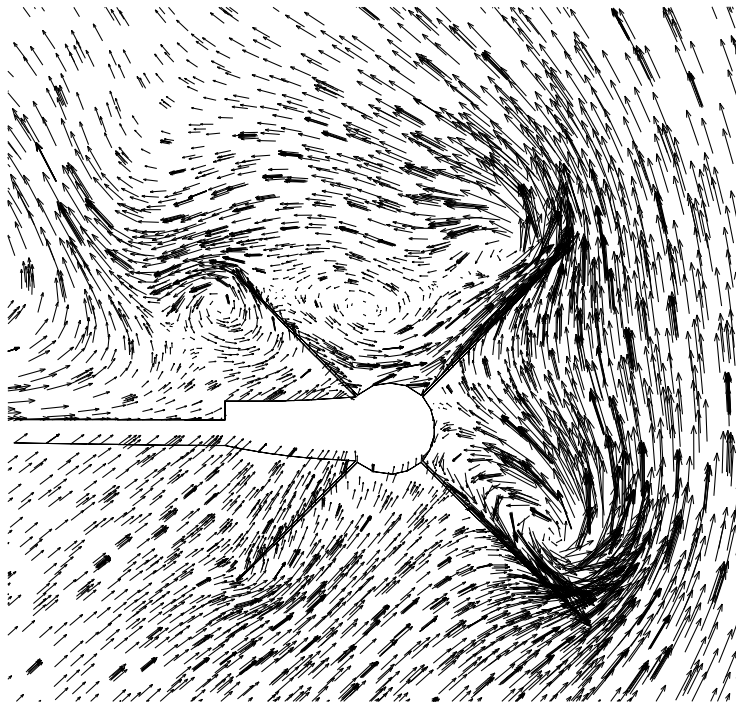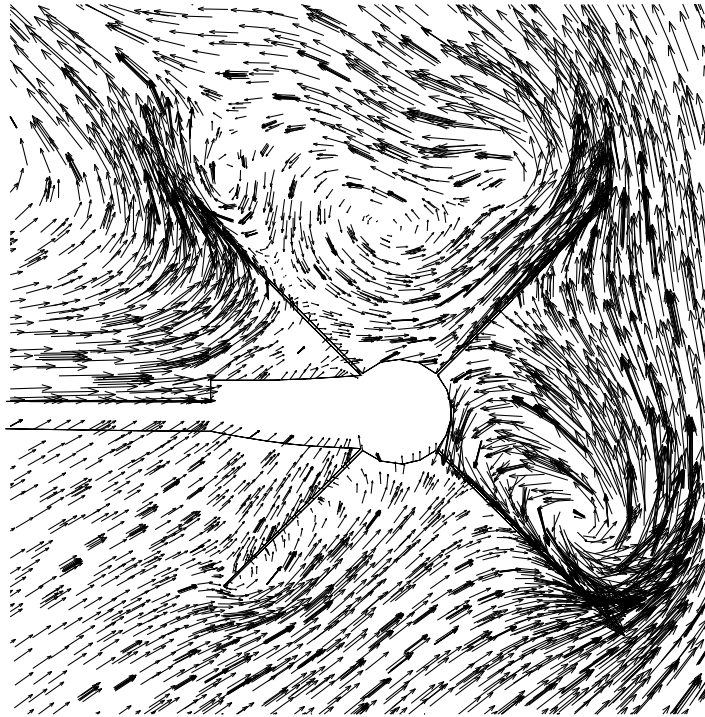
Figure 38. Close-up view of missile region depicting computed velocity vectors at FS20.2 for F-16XL with air dams, $\alpha = 10°$, $M = 0.148$.
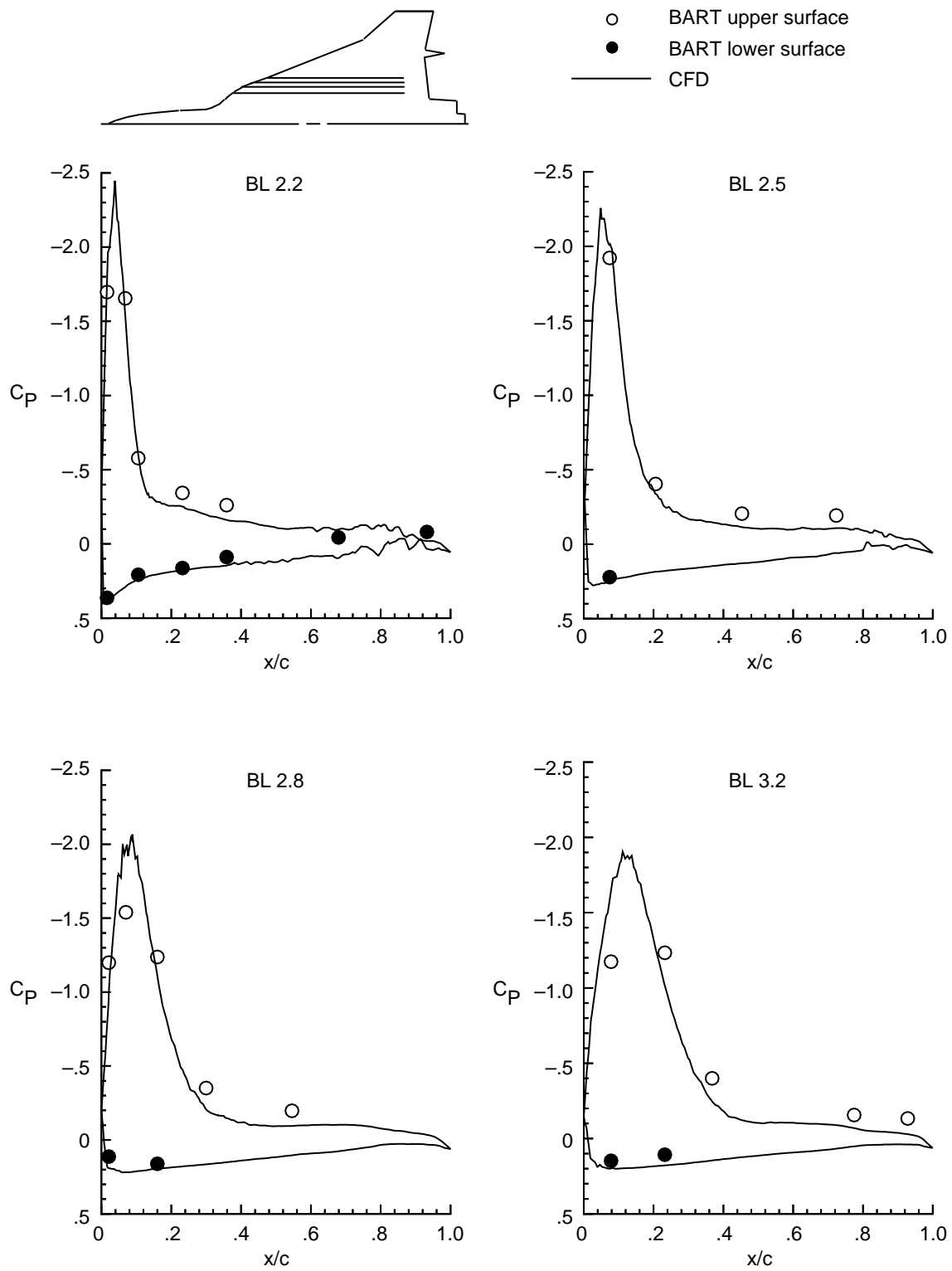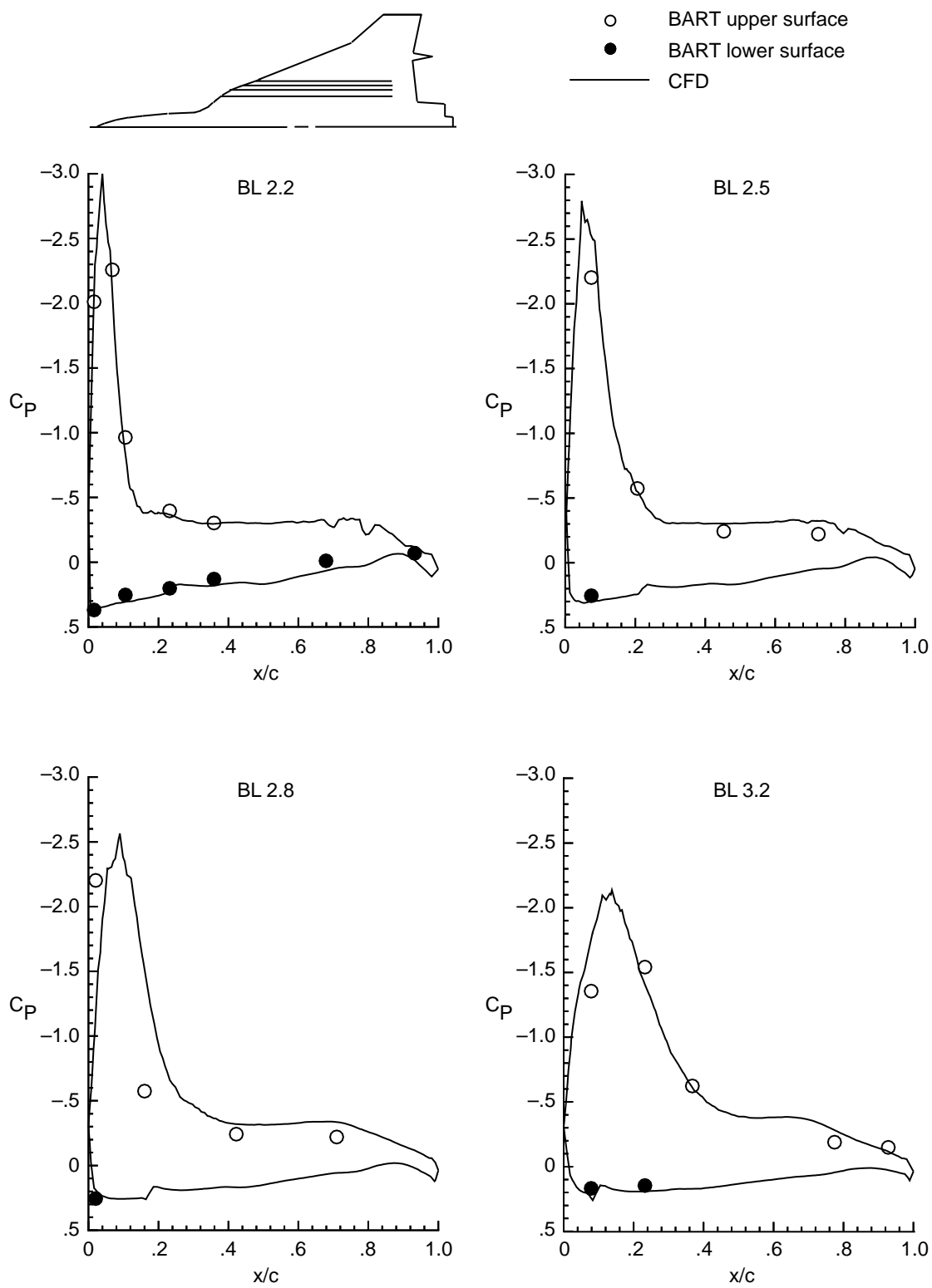
Figure 39. Streamwise distributions of experimental and computational C_P for F-16XL with air dams, $\alpha = 13°$, $M = 0.148$.

BART upper surface
BART lower surface
CFD

BL 3.8

−2.5
−2.0
−1.5
−1.0
−.5
0
.5

C_P

0   .2   .4   .6   .8   1.0

x/c

BL 4.2

−2.5
−2.0
−1.5
−1.0
−.5
0
.5

C_P

0   .2   .4   .6   .8   1.0

x/c

BL 5.1

−2.5
−2.0
−1.5
−1.0
−.5
0
.5

C_P

0   .2   .4   .6   .8   1.0

x/c

BL 5.9

−2.5
−2.0
−1.5
−1.0
−.5
0
.5

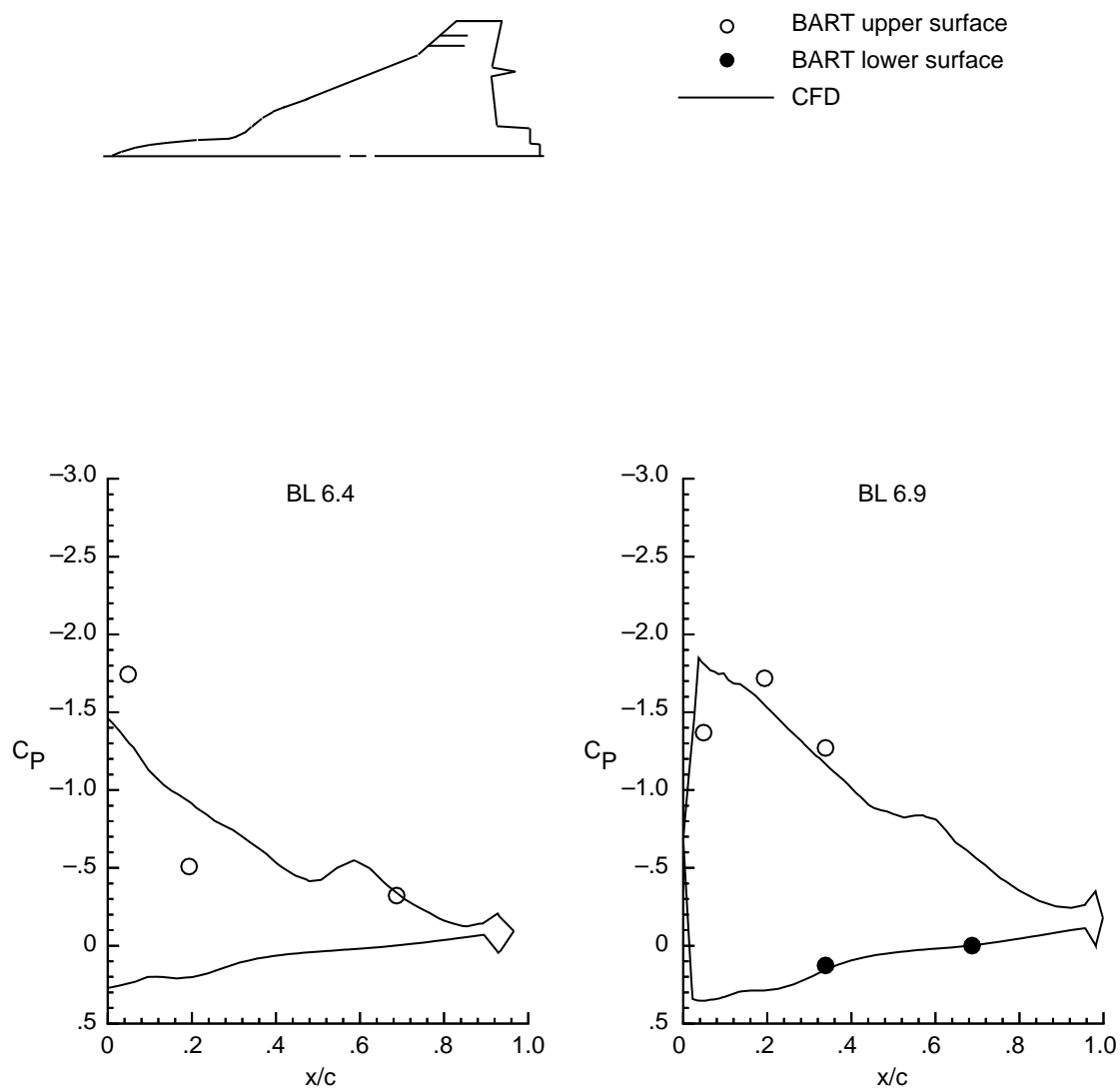C_P

0   .2   .4   .6   .8   1.0

x/c
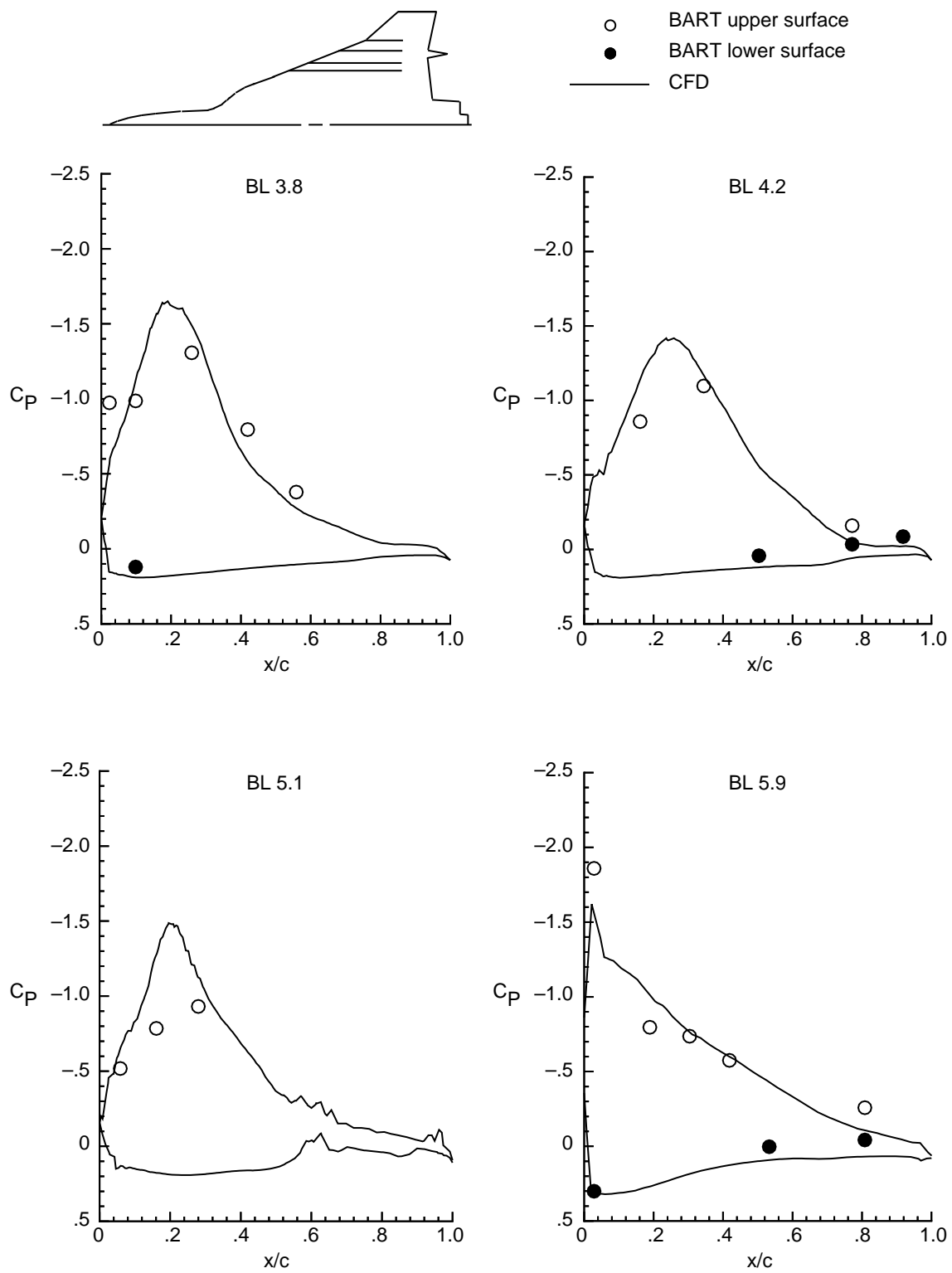
Figure 39. Continued.
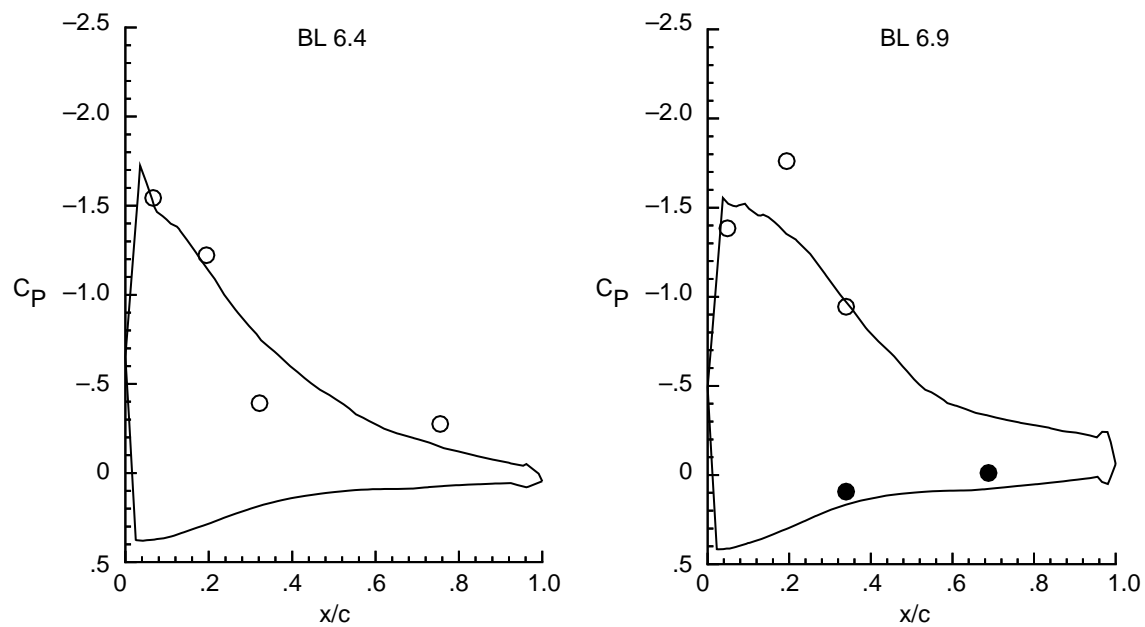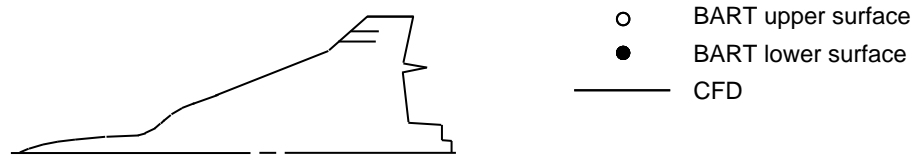
Figure 39. Concluded.
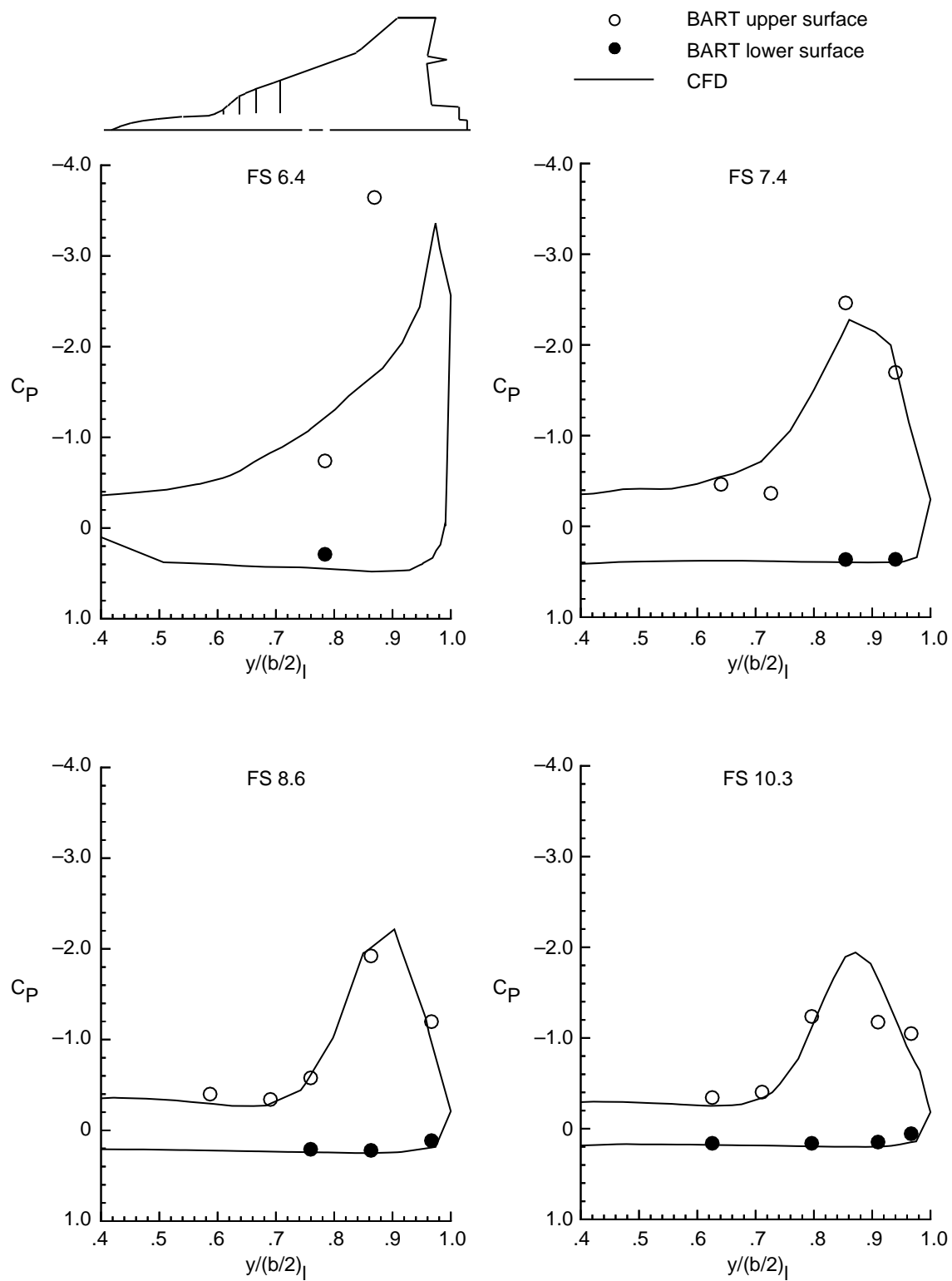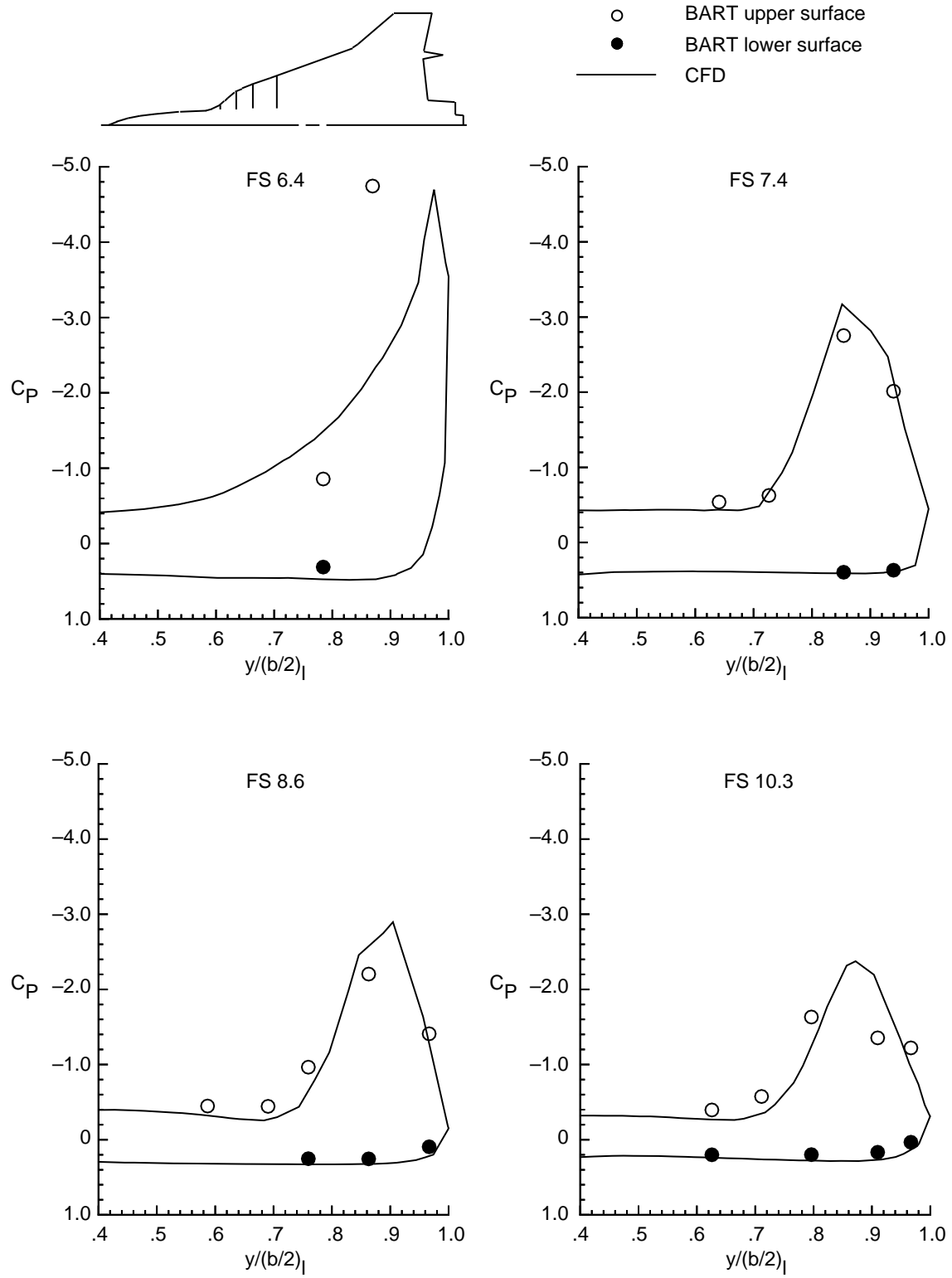
Figure 40. Spanwise distributions of experimental and computational C_P for F-16XL with air dams, $\alpha = 13°$, $M = 0.148$.
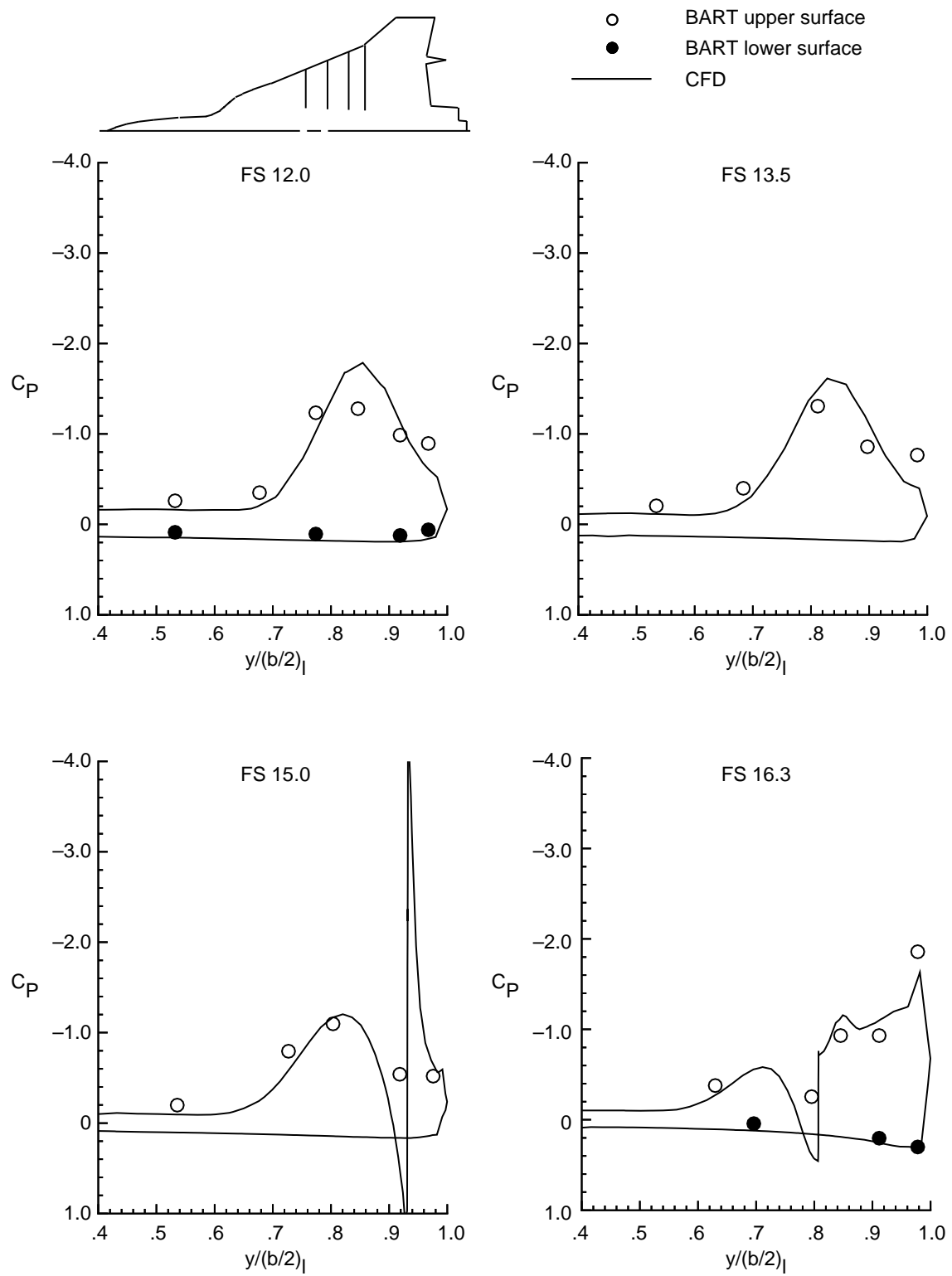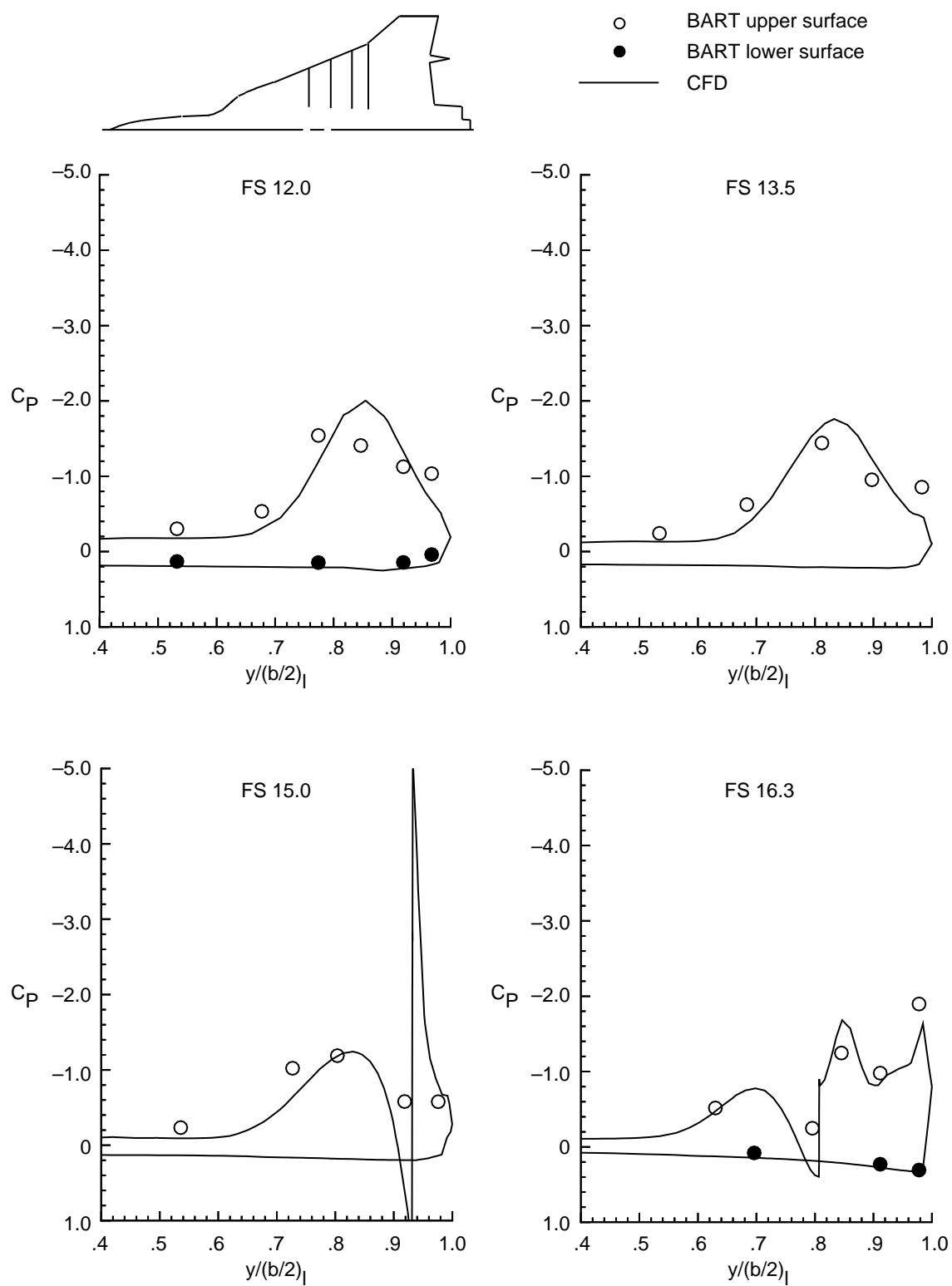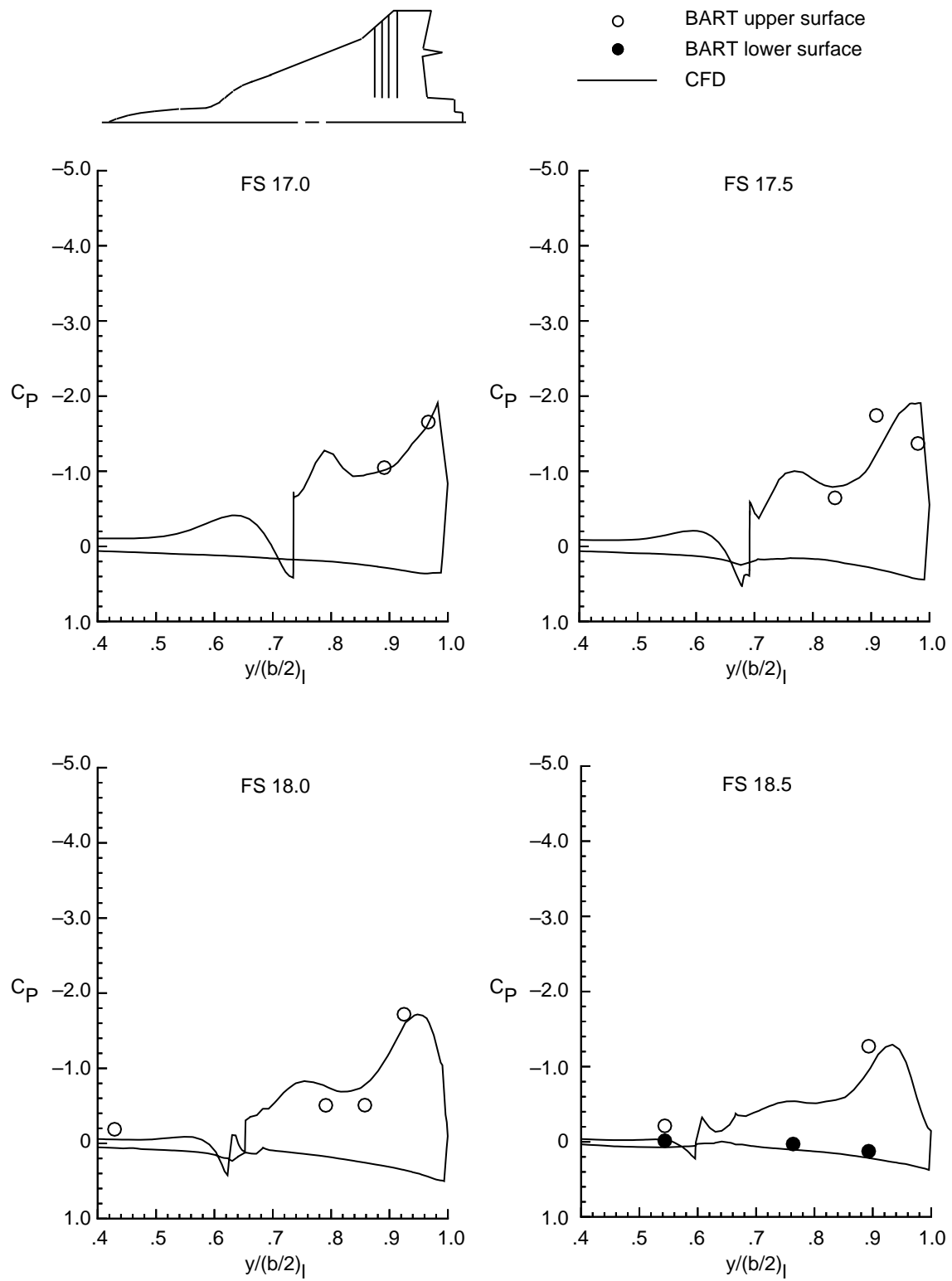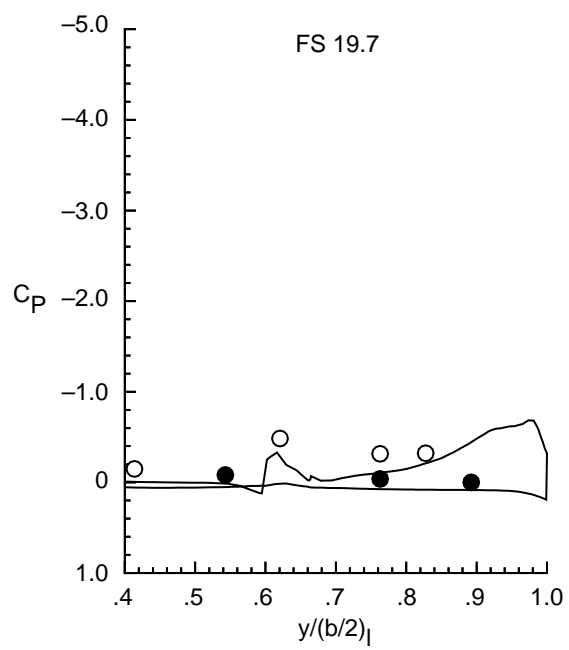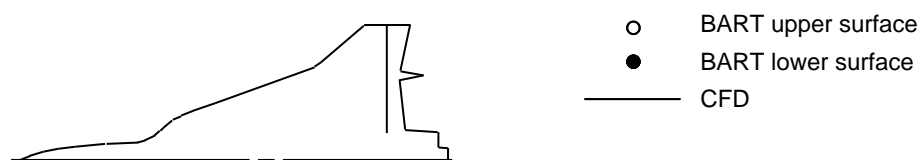
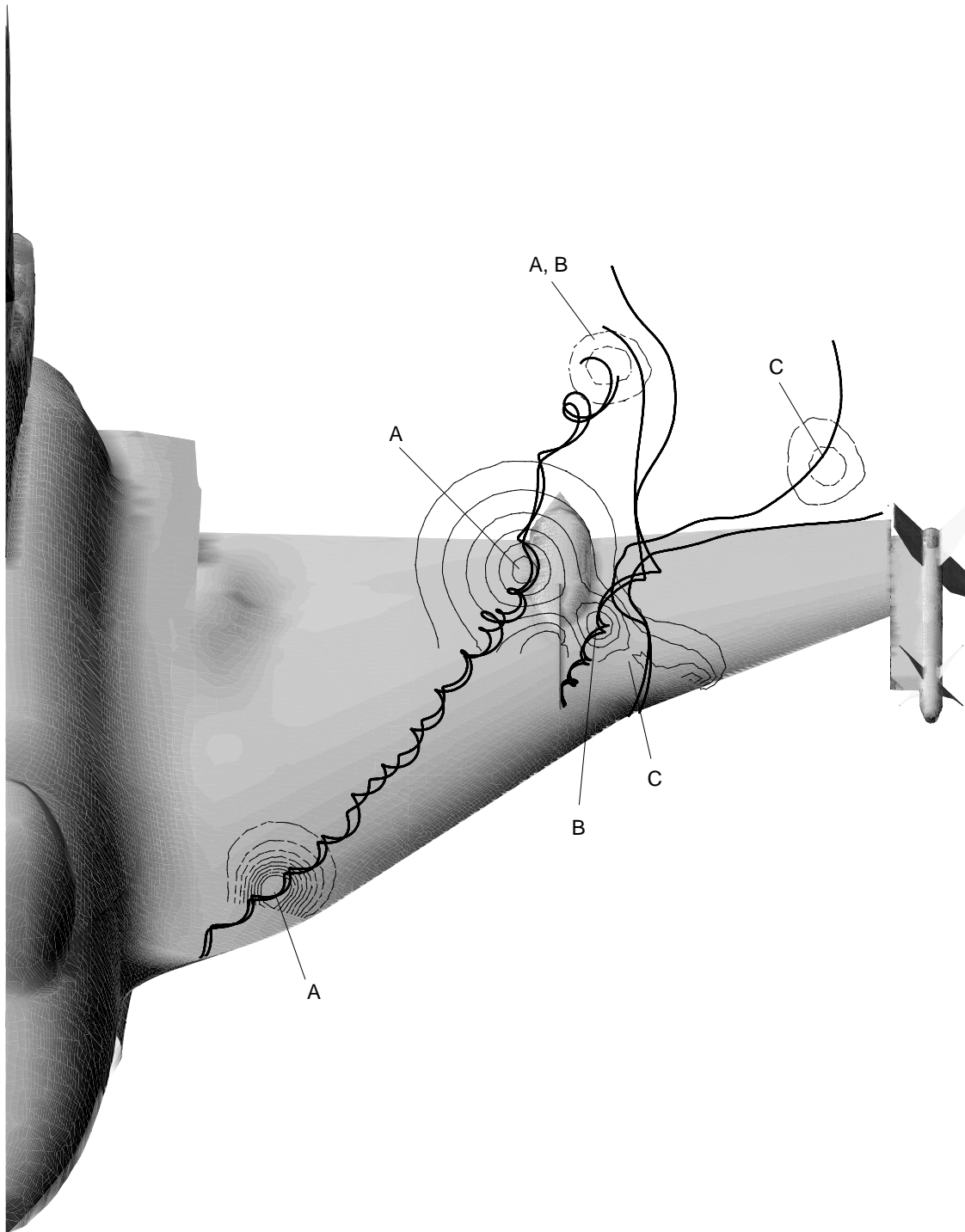Figure 40. Continued.

Figure 40. Continued.

Figure 40. Concluded.
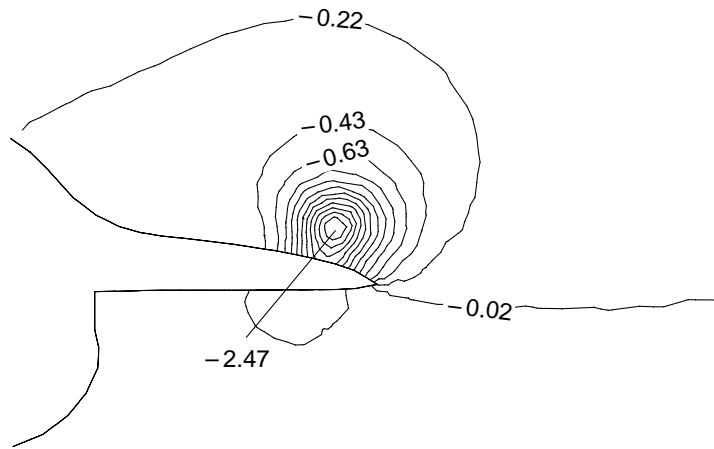
(a) Computed C_P contours.
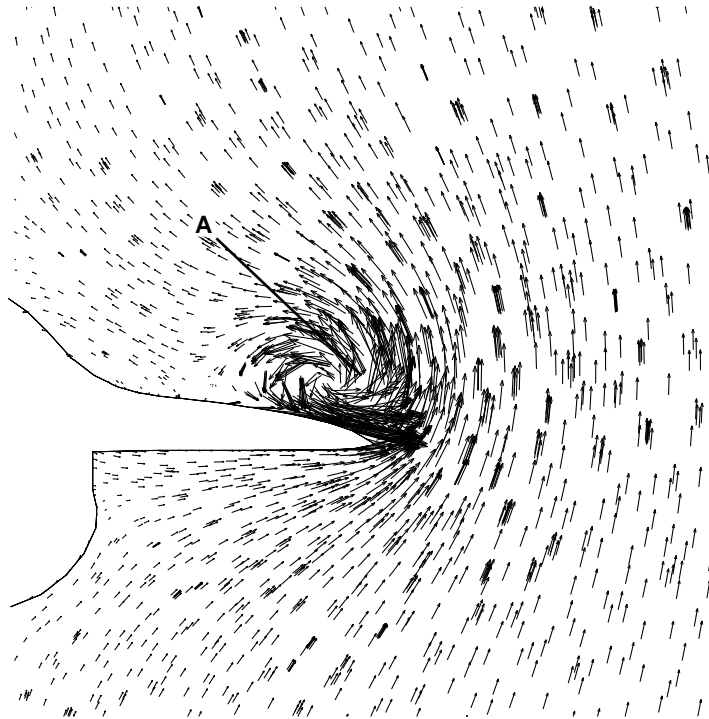
(b) Computed velocity vectors.

Figure 41. Computed C_P contours and velocity vectors at FS10.0 for F-16XL with air dams, $\alpha = 13°$, $M = 0.148$.
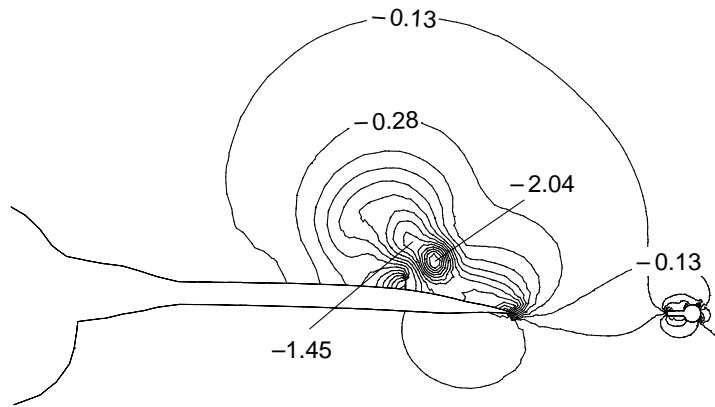
(a) Computed C_P contours.
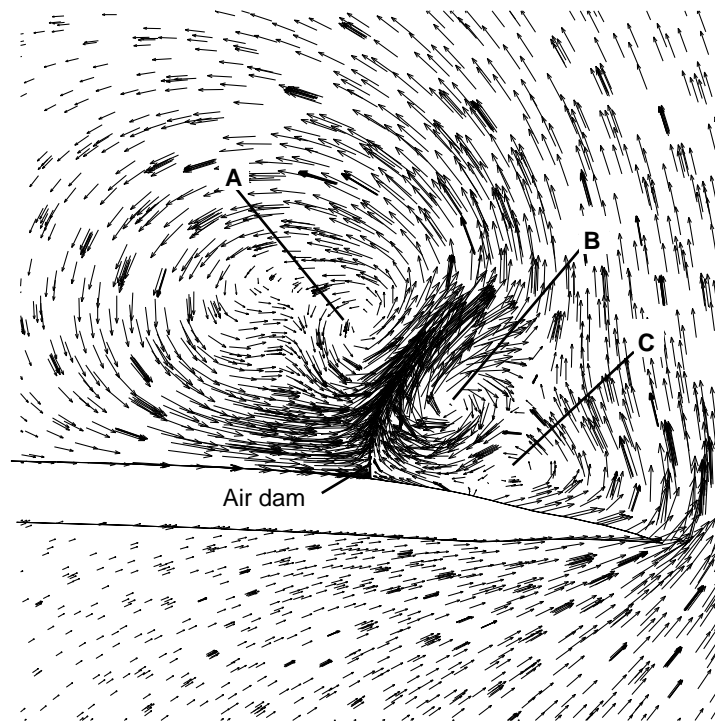
(b) Close-up view of computed velocity vectors.

Figure 42. Computed C_P contours and velocity vectors at FS16.3 for F-16XL with air dams, $\alpha = 13°$, $M = 0.148$.

(a) Computed C_P contours.

(b) Close-up view of computed velocity vectors.

Figure 43. Computed C_P contours and velocity vectors at FS20.2 for F-16XL with air dams, $\alpha = 13°$, $M = 0.148$.

Figure 44. Close-up view of missile region depicting computed velocity vectors at FS20.2 for F-16XL with air dams, $\alpha = 13°$, $M = 0.148$.

Figure 45.   Streamwise distributions of experimental and computational C_P for F-16XL with air dams, $\alpha = 15°$, $M = 0.148$.
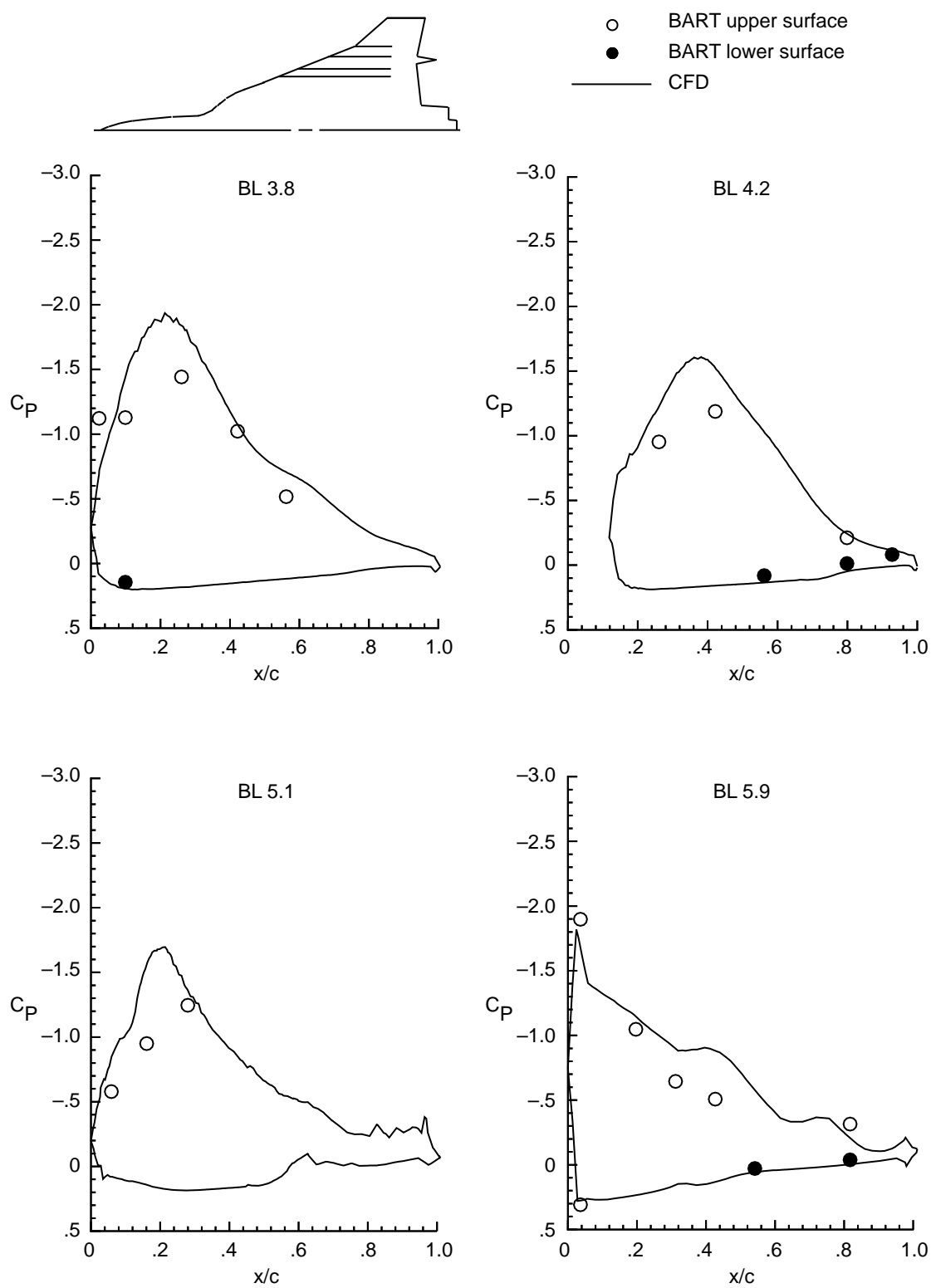
Figure 45. Continued.

Figure 45. Concluded.

Figure 46. Spanwise distributions of experimental and computational C_P for F-16XL with air dams, $\alpha = 15°$, $M = 0.148$.

Figure 46. Continued.

Figure 46. Continued.

Figure 46. Concluded.

Figure 47. Computed off-surface particle traces for F-16XL with air dams, $\alpha = 15°$, $M = 0.148$.
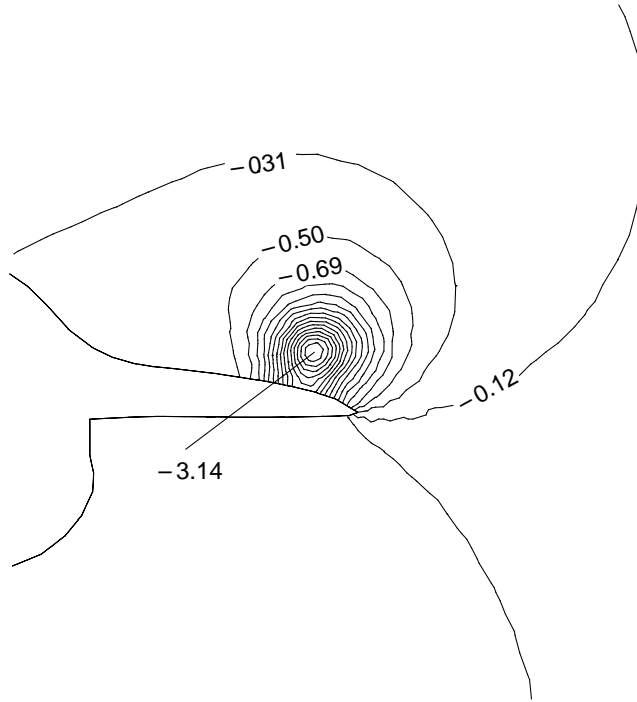
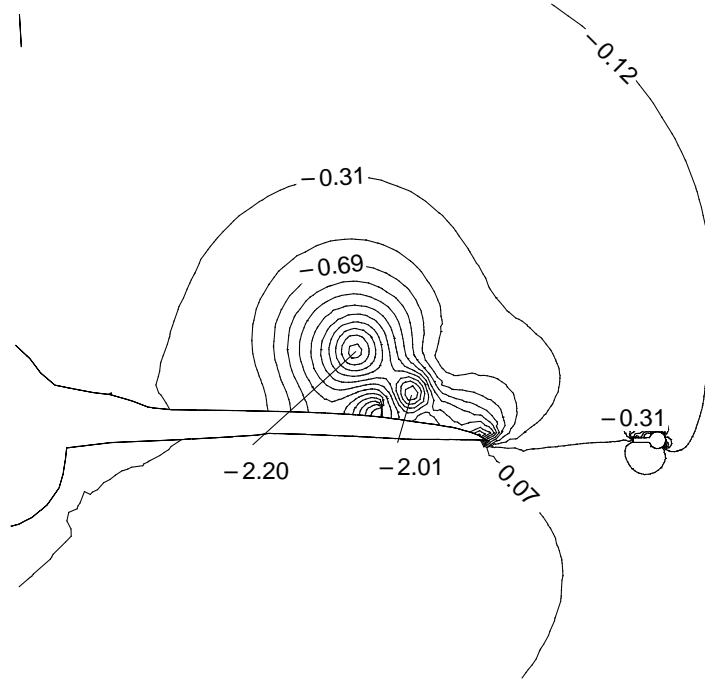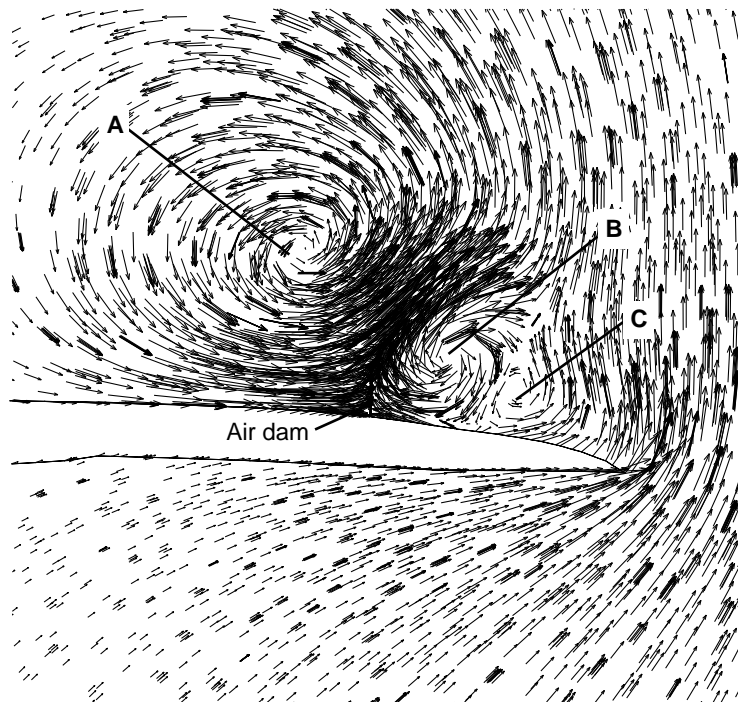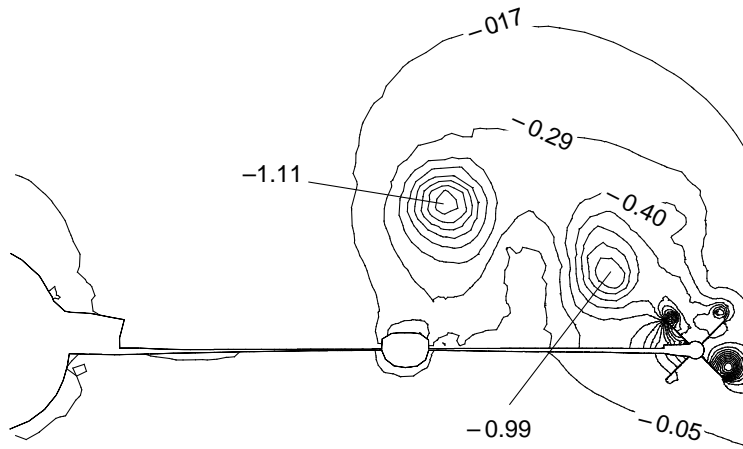(a) Computed C_P contours.
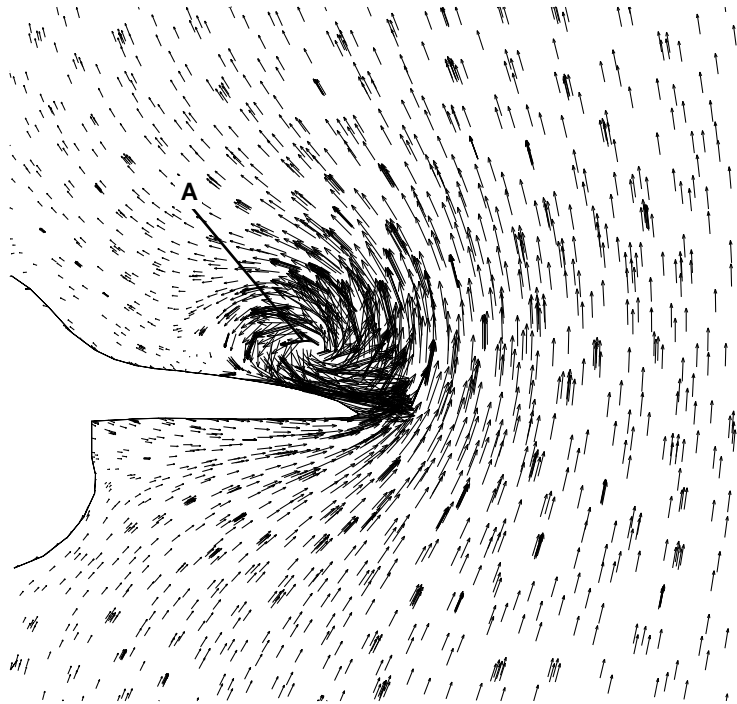
(b) Computed velocity vectors.

Figure 48. Computed C_P contours and velocity vectors at FS10.0 for F-16XL with air dams, $\alpha = 15°$, $M = 0.148$.
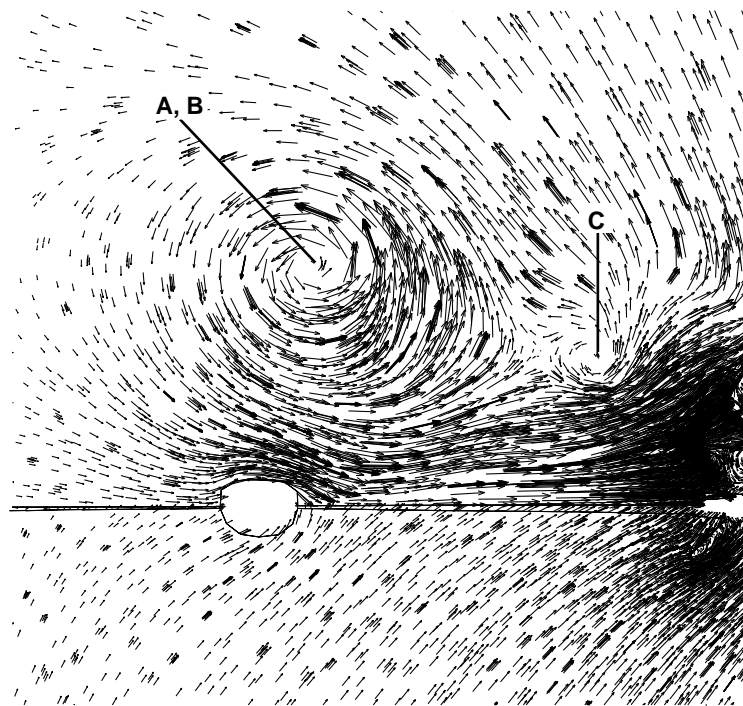
(a) Computed C_P contours.

(b) Computed velocity vectors.

Figure 49. Computed C_P contours and velocity vectors at FS18.0 for F-16XL with air dams, $\alpha = 15°$, $M = 0.148$.

(a) Computed C_P contours.

(b) Computed velocity vectors.

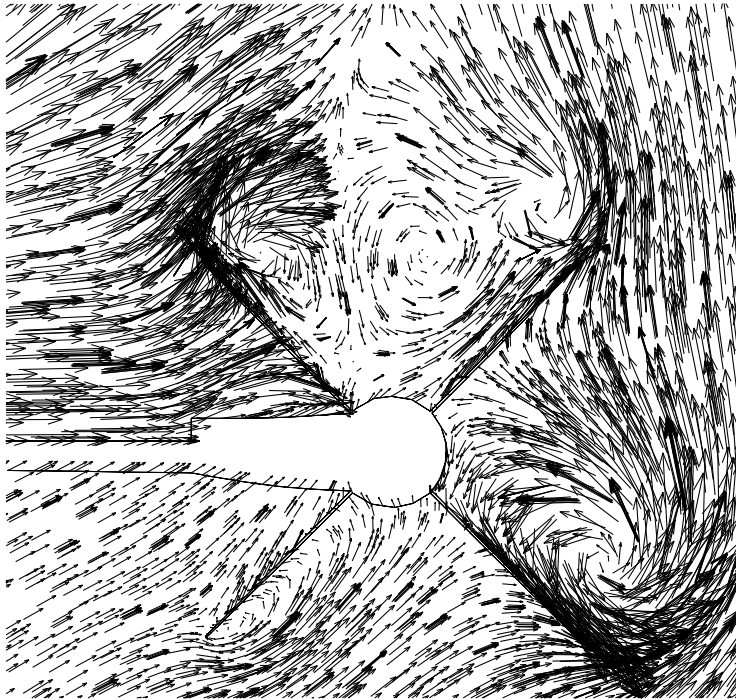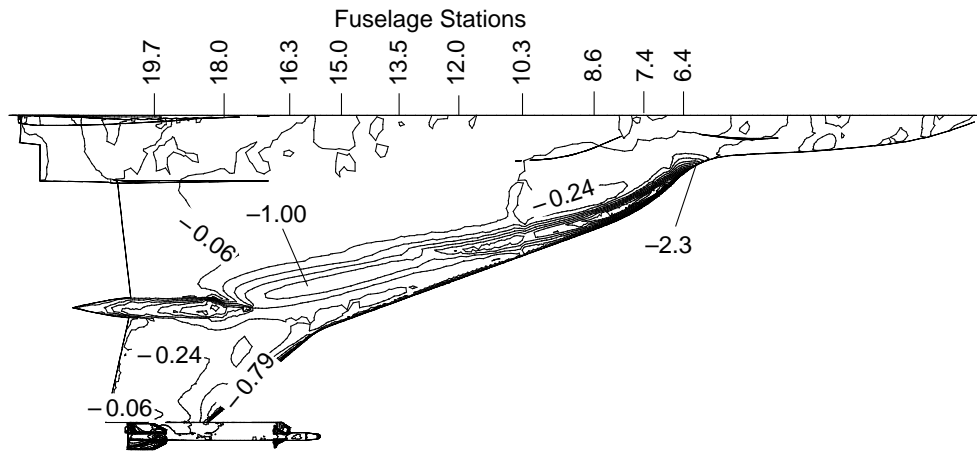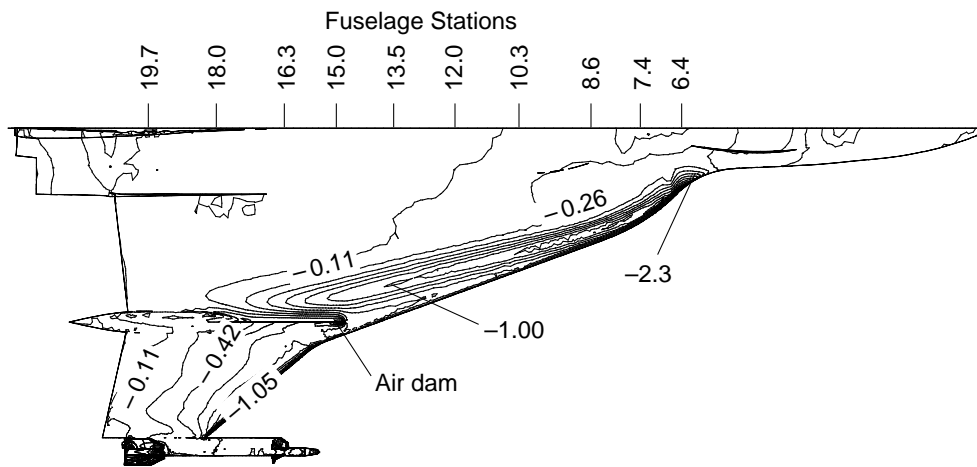Figure 50. Computed C_P contours and velocity vectors at FS20.3 for F-16XL with air dams, $\alpha = 15°$, $M = 0.148$.

Figure 51. Close-up view of missile region depicting computed velocity vectors at FS20.3 for F-16XL with air dams, $\alpha = 15°$, $M = 0.148$.

Fuselage Stations

19.7 18.0 16.3 15.0 13.5 12.0 10.3 8.6 7.4 6.4

−0.06

−1.00

−0.24

−2.3

−0.24

−0.79

−0.06

(a) Without air dam.

Fuselage Stations

19.7 18.0 16.3 15.0 13.5 12.0 10.3 8.6 7.4 6.4

−0.26

−0.11

−2.3

−1.00

−0.11

−0.42

−1.05

Air dam

(b) With air dam.

Figure 52. Computed C_P contours for F-16XL with and without air dams, $\alpha = 10°$, $M = 0.148$.
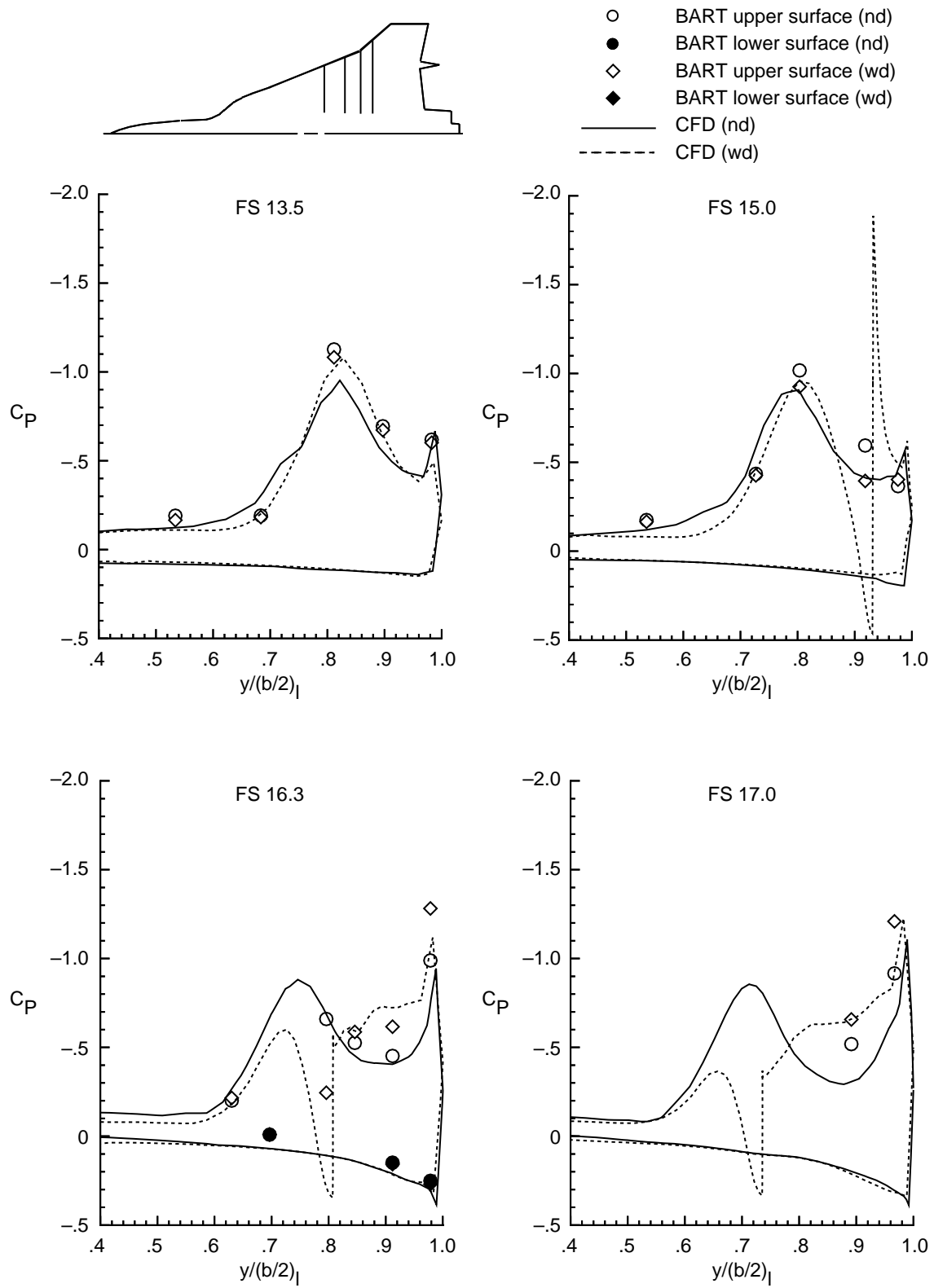
Figure 53. Spanwise distributions of experimental and computational C_P for F-16XL with and without air dams, $\alpha = 10°$, $M = 0.148$.
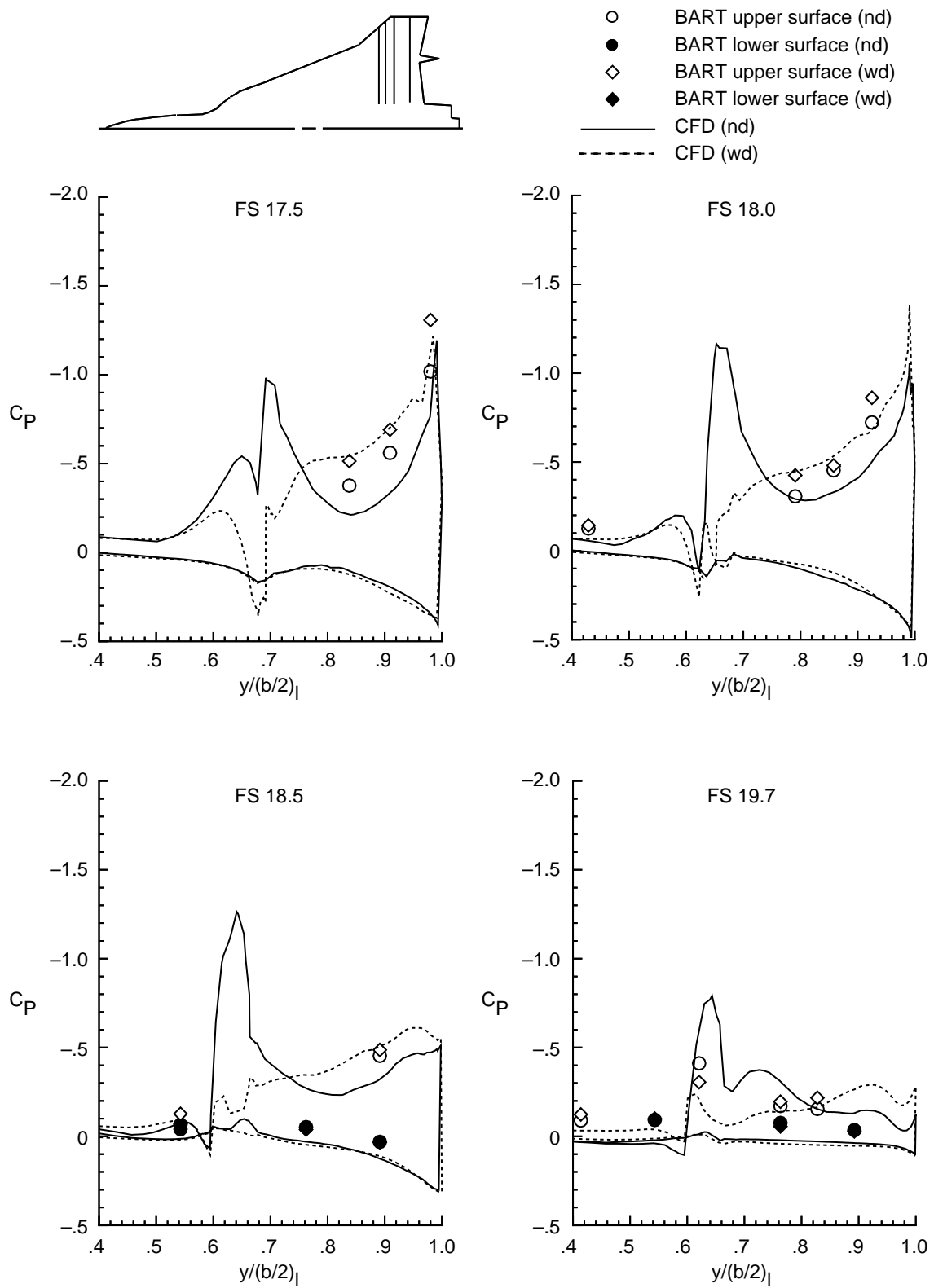
Figure 53. Concluded.

REPORT DOCUMENTATION PAGE

1. AGENCY USE ONLY *(Leave blank)*	2. REPORT DATE October 1996	3. REPORT TYPE AND DATES COVERED Technical Paper

4. TITLE AND SUBTITLE
Subsonic Analysis of 0.04-Scale F-16XL Models Using an Unstructured Euler Code

5. FUNDING NUMBERS
WU 537-03-22-02

6. AUTHOR(S)
Wendy B. Lessard

7. PERFORMING ORGANIZATION NAME(S) AND ADDRESS(ES)

NASA Langley Research Center
Hampton, VA 23681-0001

8. PERFORMING ORGANIZATION REPORT NUMBER
L-17498

9. SPONSORING/MONITORING AGENCY NAME(S) AND ADDRESS(ES)

National Aeronautics and Space Administration
Washington, DC 20546-0001

10. SPONSORING/MONITORING AGENCY REPORT NUMBER
NASA TP-3597

11. SUPPLEMENTARY NOTES

12a. DISTRIBUTION/AVAILABILITY STATEMENT

Unclassified–Unlimited
Subject Category 64
Availability: NASA CASI (301) 621-0390

12b. DISTRIBUTION CODE

13. ABSTRACT *(Maximum 200 words)*
The subsonic flow field about an F-16XL airplane model configuration was investigated with an inviscid unstructured grid technique. The computed surface pressures were compared to wind-tunnel test results at Mach 0.148 for a range of angles of attack from 0° to 20°. To evaluate the effect of grid dependency on the solution, a grid study was performed in which fine, medium, and coarse grid meshes were generated. The off-surface vortical flow field was locally adapted and showed improved correlation to the wind-tunnel data when compared to the nonadapted flow field. Computational results are also compared to experimental five-hole pressure probe data. A detailed analysis of the off-body computed pressure contours, velocity vectors, and particle traces are presented and discussed.

14. SUBJECT TERMS
Unstructured grids; Euler computations; Subsonic flow field

15. NUMBER OF PAGES
78

16. PRICE CODE
A05

17. SECURITY CLASSIFICATION OF REPORT Unclassified	18. SECURITY CLASSIFICATION OF THIS PAGE Unclassified	19. SECURITY CLASSIFICATION OF ABSTRACT Unclassified	20. LIMITATION OF ABSTRACT